博　士　論　文

Various production methods for improving mechanical properties of discontinuous recycled carbon fiber sheet reinforced thermoplastics

（不連続リサイクル炭素繊維シート強化熱可塑性樹脂の力学特性改善のための種々の製造法）

肖　冰

Abstract

With the booming development of artificial intelligence, electrification and sharing economy, except the concepts of lightweight, durability and design, repairable, recyclable and reusable material is expected widespread to adapt to modern society and sustainable development. In this research, with the aim of realizing the reuse of recycled carbon fiber (rCF) with its utmost potential and the possibility of providing new service to industry, several manufacturing and processing methods were developed for rCF reinforced thermoplastics (rCFRP) experimentally and analytically.

When relatively long rCF, for instance, around 50 mm in this study, can be obtained from recycling, exploiting its potential for high mechanical performance would be priority. Therefore, a special carding and stretching process was introduced to make carbon fiber card web reinforced thermoplastics (CWT) sheet with mixing rCF and matrix resin fibers. X-ray micro-computed tomography analysis was performed to evaluate the fiber alignment level. The influence of fiber alignment on the elastic property of CWT is illustrated analytically. The flexural strength of CWT could even reached 862 MPa which is even higher than continuous woven carbon fiber fabric reinforced thermosetting plastic.

The other scenario is that when the length of rCF tends to be short, for example, within 10 mm, usually they would be uniformly dispersed in the plane by nonwoven technology or papermaking technology introduced in this research where it mix short CF and matrix resin fibers to produce carbon fiber paper reinforced thermoplastic (CPT) sheet. But due to short fiber length and random fiber orientation, high mechanical property cannot be expected compared with CWT. Therefore, to solve its weaknesses and find its potential in industry are necessary. Among those weaknesses, one is brittleness which could inferior energy absorption ability and cause safety problems. Therefore, we used aramid fiber which has high ductile feature to hybridize with short rCF and made hybrid carbon fiber/ aramid fiber thermoplastics successfully. The energy absorption ability reached around 4 times higher than pure CPT. With optimal laminated structure, the toughness of hybrid was improved without sacrificing its stiffness. Another problem is the severe

deconsolidation phenomenon (spring-back) when CPT is subjected to post thermal processing, which may cause structure useless. Therefore, the idea of using CPT as core material in sandwich structure was proposed. The spring-back core sandwich with no obvious delamination and extremely high specific mechanical property was made successfully. The density of the sandwich could be even lower than that of water, which indicates the various possibilities of it in the near future.

Contents

Contents

List of Figures

List of Tables

List of Equations

List of Abbreviations

Abbreviations	Definition
CF	Carbon fiber
CFRP	Carbon fiber reinforced plastics
rCF	Recycled carbon fiber
rCFRP	Recycled carbon fiber reinforced plastics
CFRTS	Carbon fiber reinforced thermosetting plastics
CFRTP	Carbon fiber reinforced thermoplastics
CWT	Carbon fiber card web reinforced thermoplastics
FOD	Fiber orientation distribution
CPT	Carbon-fiber paper-based reinforced thermoplastics
AF	Aramid fiber
AP	Aramid-fiber paper
HAP	Handmade aramid-fiber paper
APT	Aramid-fiber paper-based reinforced thermoplastics
HAPT	Handmade aramid-fiber paper-based reinforced thermoplastics
LH	Interlaminated carbon fiber and aramid fiber hybrid reinforced thermoplastics
MH	Intermingled carbon fiber and aramid fiber hybrid reinforced thermoplastics
PP	Polypropylene
PA6	Polyamide-6
CTT	chopped carbon fiber tape reinforced thermoplastics
UD	Unidirectional
SB	Spring-back ratio

1. Introduction

1.1. Background

Carbon fibers (CF) were first introduced in the 1950s. Along with the development of aerospace science and technology, it was commercially utilized and the demand of it has increased since the 1960s with its light weight and excellent engineering properties as high modulus and high strength fiber material [1]. The capacity to produce the small-tow CF for most aerospace application is dominated mainly by Japan's and American companies as shown in Table 1-1 [2]. The global carbon fiber market from 2012 to 2017 and the forecast from 2018-2023 is shown in Figure 1-1, segmented by end use industry and precursor. It was predicted that the global market for carbon fibers is growing by 6% per year through 2023 [3].

Table 1-1 Summary of capacity and locations of the top six small-tow carbon fiber producers [2]

CF supplier	**Capacity 2012 vs 2020 (tonnes/yr)**	**Prepreg**	**Aerospace Customers /Programs ***	**Comments**
Toray	18,900 vs. 50,000	Tacoma, WA, United States Japan	Boeing 787 Airbus	60% aviation market share
Toho Tenax	15,100 vs. 18,900	Shizuoka, Japan	Bombardier C Series, A380	Thermoplastic focus Airbus contract
Mitsubishi Rayon	10,600 vs. 14,300	Irvine, CA, United States	A380	Largest acrylic fiber producer in Japan
Hexcel	7,250 vs. 10,000	United States; Europe: Tianjin, China	Airbus A350 A380	47% of 2007 sales driven by Boeing and Airbus

Cytec	2,400 vs. 6,000	Tempe, AZ, United States; Greenville, TX, United States	Bombardier F-35 COMAC C919	Boeing 787 uses infusion resins and surface treatments including prepregs by Cytec

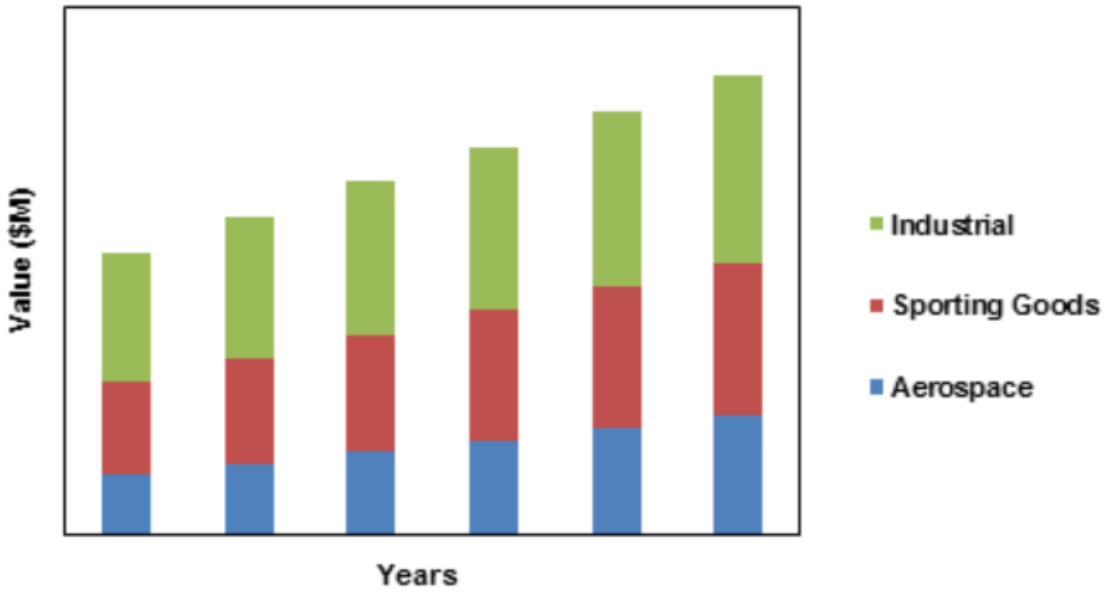

(a) Global carbon fiber market ($M) trends by end use industry from 2012 to 2017

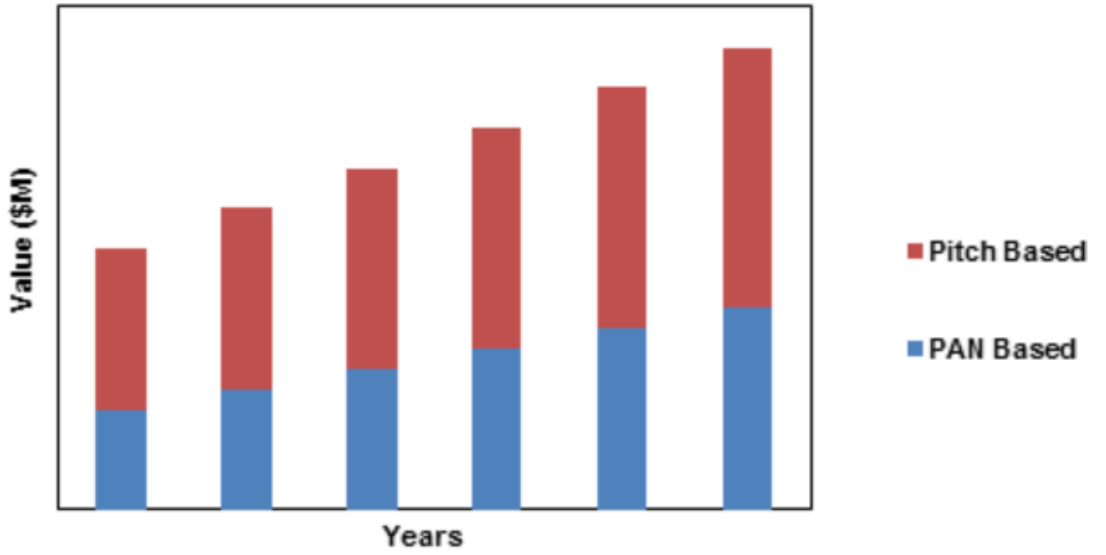

(b) Global carbon fiber market ($M) forecast by precursor from 2018 to 2023

Figure 1-1 Global carbon fiber market ($M) growth [3]

In most cases, CF cannot be directly used solely due to its weakness against compression, therefore it was combined with matrix and developed into carbon fiber reinforced plastic (CFRP). Several decades later, owing to its high mechanical performance and low weight, besides being used in aerospace and automotive industries, it has been applied in an array of other fields varying from wind turbines and satellites to drones and sports goods. The global demand volume of CFRP in 2017 is around 114k tons, which results in annual growth rate of around 12.8% from the year 2010. Apparently, a further positive development ranging from 10-13% is expected in the near future as seen in Figure 1-2 [4].

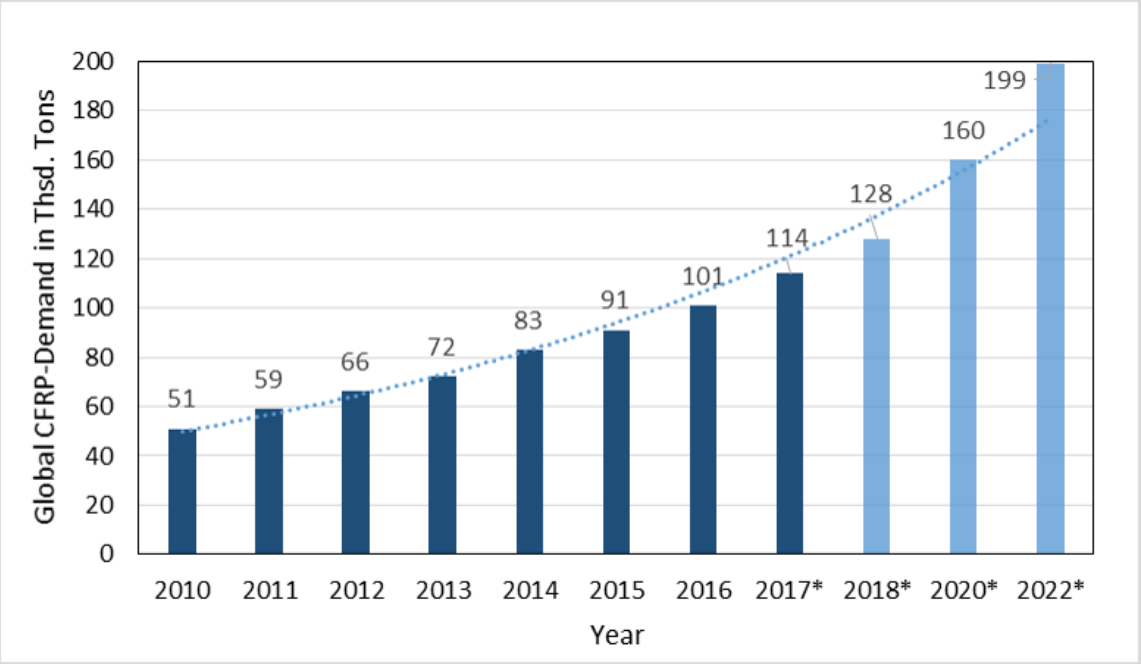

Figure 1-2 Development of the global CFRP-Demand in Thsd. Tons from 2010 until 2022 (*Estimation; 11/2018) [4]

1.2. Current status of carbon fiber recycling

1.2.1. CFRP wastes

Although it is not yet a mainstream material, there is already a large amount of CFRP products nearing the end of their life cycles. The wastage of CFRP correspondingly increases along with its demand, and up to 40% can be wasted during manufacturing and due to end-of-life [5]. For

example, 6000 to 8000 commercial aircraft are expected to reach their end-of-life by 2030 [6]. Figure 1-3 [7] demonstrates composite demand and waste which was determined by considering various estimates of lifespan as well as production ramp rates. The increasing CFRP wastes have place the burden of many manufactures, which means the end of life options should be considered before designing.

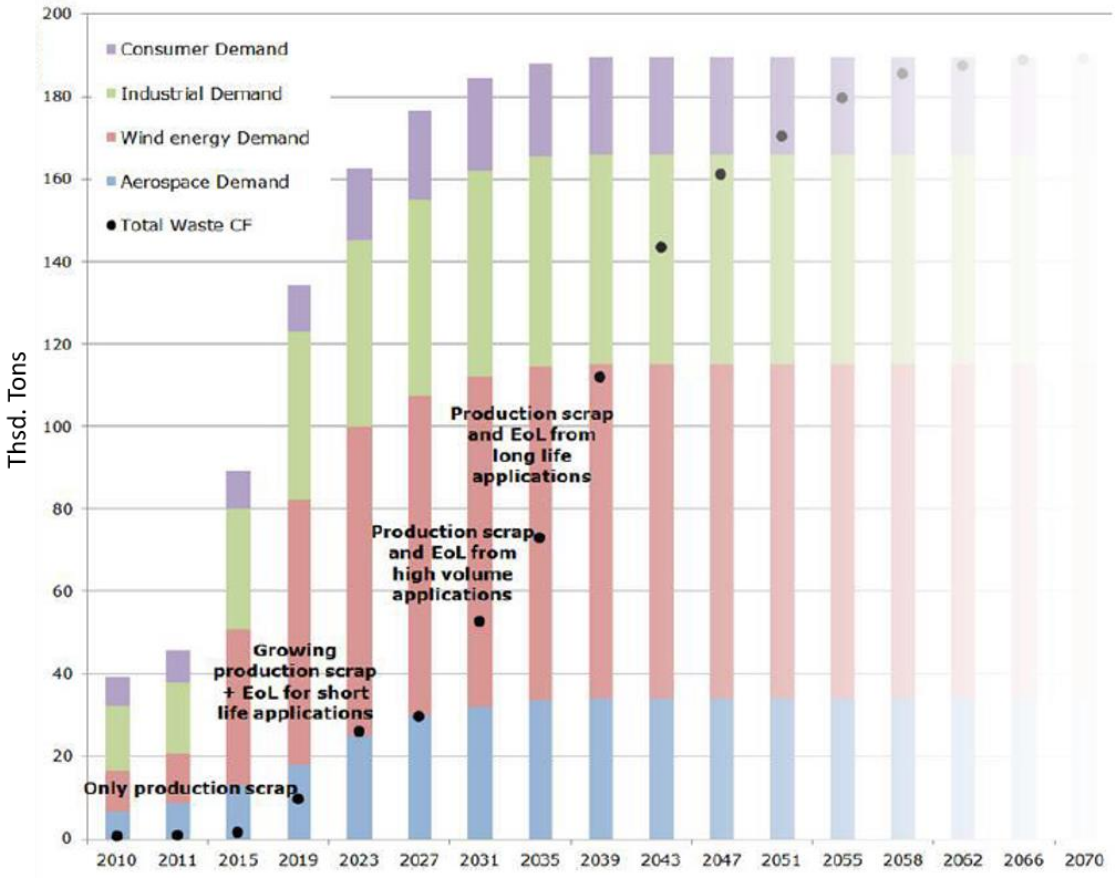

Figure 1-3 Graph of composite demand (bars), and waste (dots) in kilotonnes by year [7]

At the beginning, most CFRP waste was disposed of and sent to landfills, however it is considered an unsatisfactory solution due to the environment and legislation [8]. Recycling has been adopted as an effective way to deal with CFRP wastes because it is estimated that producing rCF requires just 1/10 of the energy needed for virgin CF; and a kilogram of rCF is valued at around US$15 while that of virgin CF is US$24-30. Airbus plans to recycle 95% of its CFRP wastes with 5% recycled back into the aerospace sector by 2020-2025; BMW have reused all CF wastes from production where 10% of the CF applied in BMW I series is rCF [9].

1.2.2. Recycling technologies

Currently, most CFRP waste consists of carbon fiber reinforced thermosetting plastics (CFRTS) either in plant or in market. Mechanical recycling and fiber reclamation are the two main classifications when it comes to fiber recycling [10, 11] where mechanical recycling involves shredding, crushing, milling etc. resulting in powdered and fibrous products while fiber reclamation is related to thermal decomposition or chemical process. Among them, fiber reclamation is favorable since it is able to recover individual fibers, and it has even been confirmed that currently available fiber reclamation technologies are able to maintain the mechanical properties of recycled carbon fiber (rCF) such as using supercritical n-propanol method as shown in Figure 1-4 [12]. Cai et al. [13] developed a superheated steam treatment (SHS), which is currently the most efficient way to recycle CFRP compared to other conventional thermal methods, and found a beneficial recycling condition. Figure 1-5 shows the fracture surfaces of virgin CF and rCF using SHS treatment.

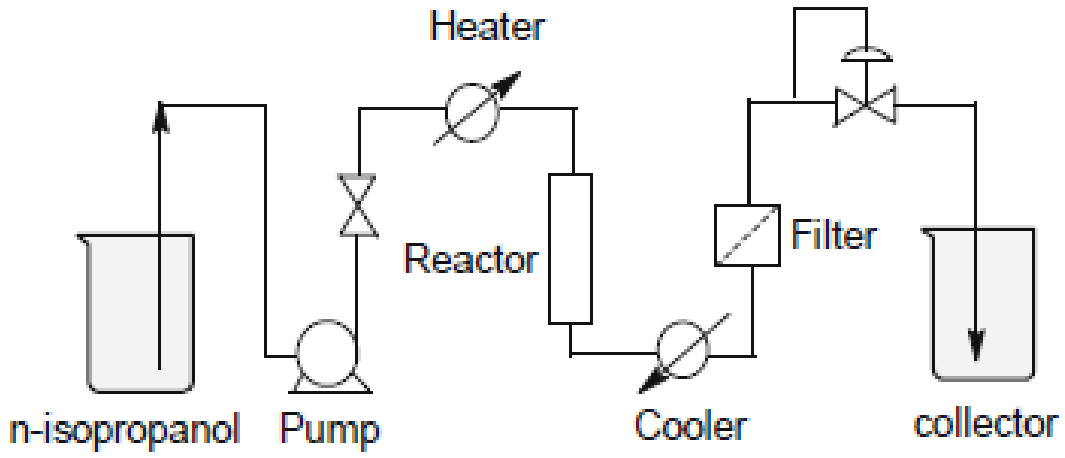

Figure 1-4 A schematic flow diagram for the recycling process [12]

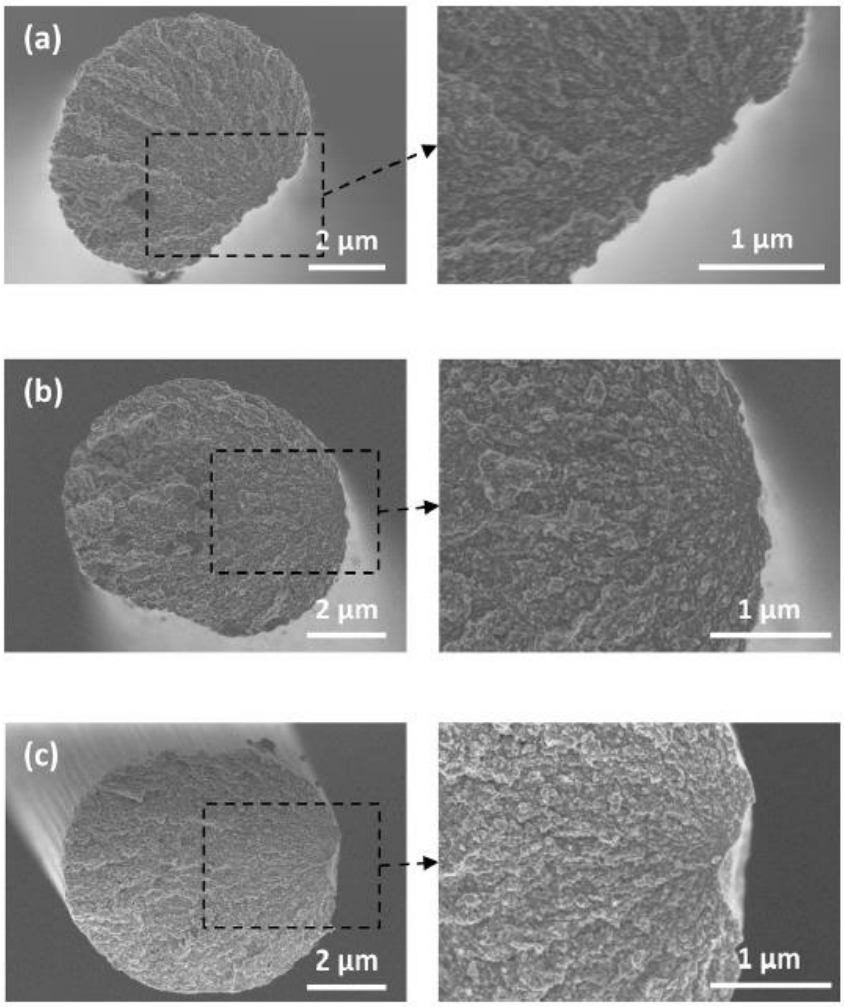

Figure 1-5 Fracture surfaces of carbon fibers: (a) virgin, (b) SHS 650℃, and (c) SHS 2-step

1.3. Re-Use of rCF

The technologies for CF recycling have been able to maintain its mechanical properties. However, it is not enough. The CFRP lifecycle loop is needed to be closed. That is, carbon fiber reclaimed from end-of-life sources should be repurposed for use in composites applications as Figure 1-6 [11].

Besides, it is still difficult to fully recover its original length and fiber alignment due to complex shapes or complicated fabrication status of the parts needed to be recycled. Therefore, it is

important to determine how to regenerate it for its original use. Therefore, the goal is to make full use of the rCF from fiber reclamation.

Figure 1-6 Close life-cycle for CFRP [11]

1.3.1. Matrix choosing for rCF reinforced plastic (rCFRP)

Considering choosing new matrix to remanufacture plastics, there are two typical types of rein matrix, thermoset and thermoplastic. The more conventional resin material used is thermosetting resin mentioned above. It has been reported that thermoset matrix systems take up around 70% proportion [4]. But thermoplastic has been attracted more and more attention and enjoying a period of growth, which is expected to continue not just because of its fast cycle times but also of its high formability [14, 15]. Besides, unlike thermoset which is not easily recycled, by using thermoplastic as a matrix, it can be recycled again in the future. Therefore, this study focuses on

investigating whether rCF with a thermoplastic matrix can be reused. The plastics made with CF and thermoplastic matrix are called carbon fiber reinforced thermoplastics (CFRTP).

1.3.2. Re-manufacturing of rCFRP

Re-manufacturing methods for rCFRP have been proposed based on two recycling technology families mentioned above (Figure 1-7). RCF is usually in the state of discontinuity and randomness, uniformity and satisfactory mechanical performance are difficult to be achieved in the rCFRP made by direct molding method. Therefore, before mixing with matrix, certain arrangement on fibers is necessary.

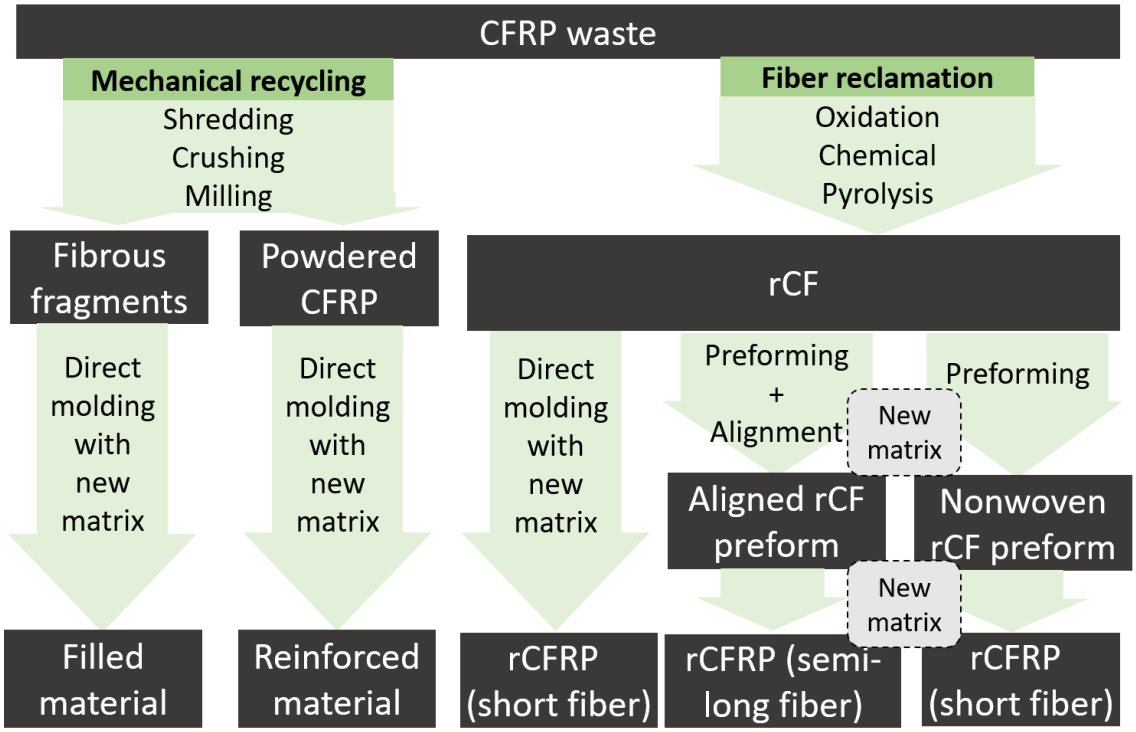

Figure 1-7 Main technologies for rCFRP

With the aim of realizing the reuse of recycled carbon fiber (rCF) with its utmost potential and the possibility of providing new service to industry, proper manufacturing and processing methods should be developed for rCFRP.

1.4. Problems and solutions

In most case, it is able to obtain semi-long rCF (50-200mm) from in-plant CFRP wastes while recycling that involves grinding would produce short rCF (<40mm) [16]. When semi-long rCF can be obtained from recycling, exploiting its potential for high mechanical performance would be priority, for which re-arranging fiber clusters and re-aligning fibers should be considered. The other scenario is that when the length of rCF is short, usually they would be uniformly dispersed in the plane by nonwoven technology or papermaking technology introduced in this research. But due to short fiber length and random fiber orientation, high mechanical property cannot be expected. Therefore, to solve its weaknesses and find its potential in industry are necessary.

1.4.1. Semi-long rCF

1.4.1.1. Fiber alignment

Fiber alignment is an important factor that affects both mechanical performance and molding condition of the composite [11]. Gillet et al. [16] investigated the influence of fiber alignment on the strength and modulus of composite material and found the significant effects that lead to fiber alignment. In general, highly aligned short fiber composites have a great potential to enter production within the automotive industry if it is possible to realize mass production targets without significant reduction of properties [17, 18]. In terms of fiber alignment technique, there has been some research on developing manufacturing methods. A centrifugal alignment rig was presented by Werken et al. [19] (Figure 1-8), and they revealed that the process could produce mats with roughly 70% of fiber alignment within ± 15°. Yu et al. [20] introduced a manufacturing method for aligned discontinuous fiber composites (HiPerDiF) (Figure 1-9), and specimens with 67% of their fibers aligned within the range of ±3° were successfully produced.

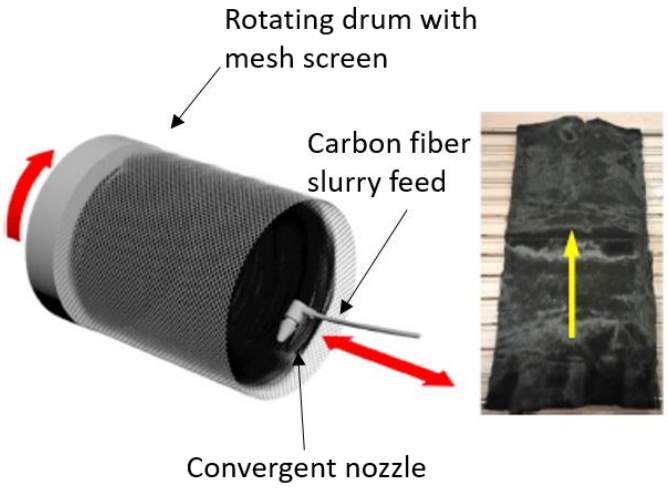

Figure 1-8 Centrifugal alignment rig and 60 × 120 mm fabricated aligned carbon fiber mat [19]

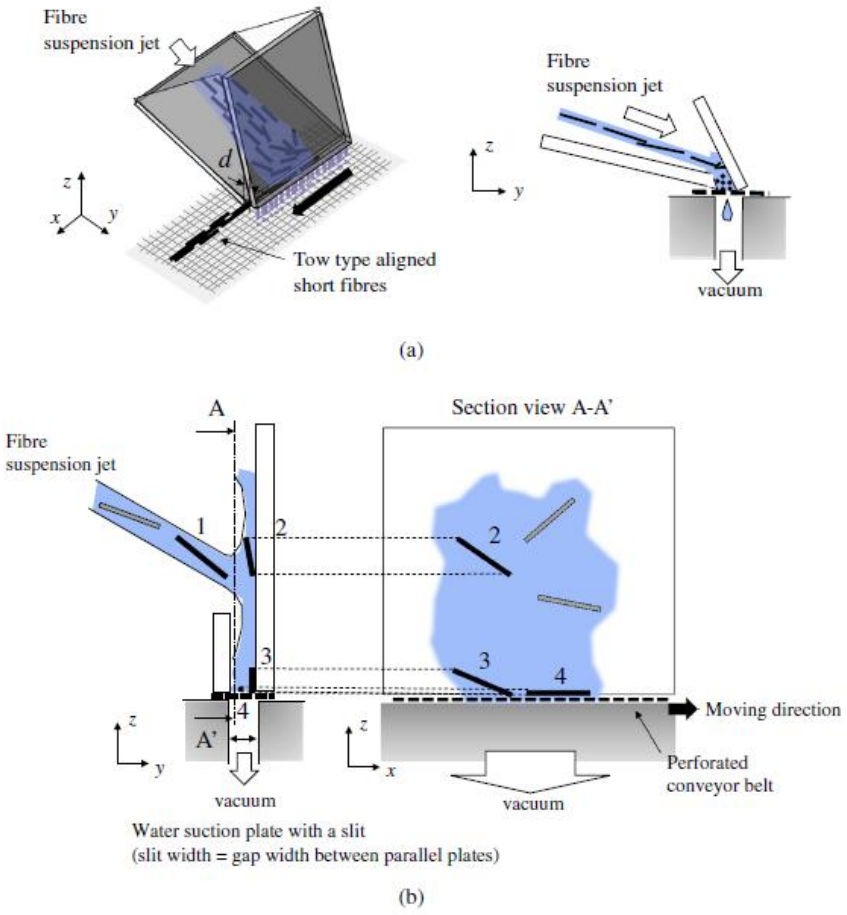

Figure 1-9 Schematic drawings of the new discontinuous fiber alignment method [20]

Dry aligning methods like carding and yarn spinning are more productive and effective for making aligned fiber composites. Hasan et al. [21] developed core–sheath hybrid yarn structures with 60-mm long staple CF and polyamide 6 (PA6) fibers by using a friction spinning machine. Unidirectional CFRPs with at least 86% of the strength and Young's modulus of a composite made heavy tow CF filaments could be achieved. Akonda et al. [22] used a carding and spinning process (Figure 1-10) to produce CF/polypropylene (PP) yarns with approximately 15-27.7% CF volume fraction (V_f). The average values obtained for tensile and flexural strength were 160 MPa and 154 MPa, respectively. Miyake and Imaeda [23] also used a special carding and spinning method (Figure 1-11) to make CF/PP yarns with approximately 13% V_f, and almost 70% of fibers were distributed within the range of ±14°.

Figure 1-10 Yarn winding arrangement [22]

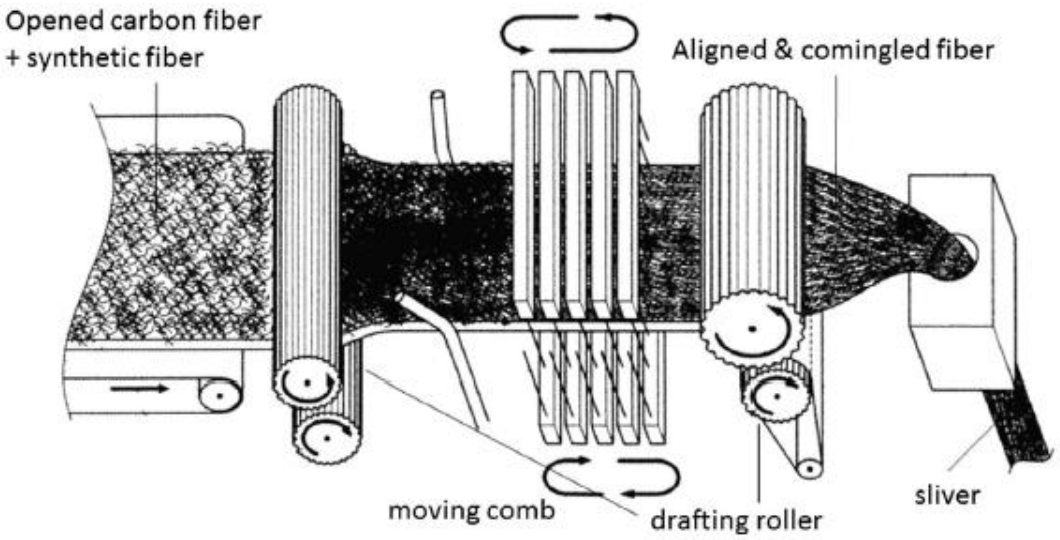

Figure 1-11 Schematic of the equipment use for making aligned silver [23]

Recent researches related to dry aligning methods for CF have mostly adopted concepts from the spinning of staple yarns, wherein blends of CF and resin staple fibers are produced using a carding process to obtain a continuous silver, which is subsequently drafted and then wrap spun into a yarn [22, 24-26]. However, silver and yarn manufacturing from CFs is still challenging due to their brittleness. Although the most recent research [21] reported tensile strengths of composites manufactured from CF/PA6 yarns reached 838 MPa, most other studies have achieved a maximum tensile strength of only 160 MPa for composites with hybrid yarn [22]. Besides, there is a possibility that the yarn axis deviates from the loading direction in wrap spinning processes [21]. These factors demonstrate that this process could offer better fiber alignment; however, it is restricted by its low productivity.

In order to improve the productivity of dry aligning and reduce the risk of CF breakage during elaborate processing steps, we aimed to improve the carding process. The carding provides the mixing and aligning of CF/resin fibers in plane to form flat sheet products that are directly able to be used for molding. Herein, blends of CF/polyamide (PA) fibers were aligned by a modified carding device; components including the rollers, cylinder, wire-clothing, etc., were all adjusted for a better quality of CF/PA6 blends. At high CF volume fractions, the stripping ability of the pins will decline due to fiber saturation. To further improve the fiber alignment level, a stretching

process was introduced to stretch the preform from carding process with the assistance of a shell-core synthetic PA fiber.

Analytical models for prediction of elastic properties in short fiber systems have been developed and validated by some researchers [27-29]. In this part, the elastic moduli of composites were analyzed using a simulated laminate model. Netting analysis was also applied since it is another approach to calculate ply stresses and is often used for helically wound reinforced pressure vessels and tubes [30-32]. Although netting analysis has been regarded as a limited case of the laminated structure, it is an excellent basis for quick estimation and an approximation of the response of a composite. And we used it to compare with classic laminate theory and evaluate the effect of fiber orientation.

1.4.2. Short rCF

1.4.2.1. Brittle fracture of short rCF reinforced thermoplastic

As is known to us from conventional materials like metal at certain condition, brittle fracture is the worse type of failure because it occurs suddenly without warning and the material exhibits no visible signs of damage [33]. Involving little or no plastic deformation at the crack tip, it can be identified by the smoothness of the failed surface where a strong indication of a brittle fracture can be identified by smooth fracture surface [33].

In microscale aspect, the propagation of a brittle crack require much less energy than a ductile crack, which means the stress applied to grow a crack is lower than that at which failure would normally be expected [34]. And such a fracture requires stress concentrations which are usually initiated by pre-existing microsacle defects, such as void, inclusion, discontinuity etc., or regions of high localized stress concentration, such as a crack tip, notch or drilled hole [33-36].

Brittle failure is commonly unwanted and should be avoided in engineering industries because the failure shows catastrophic in components or parts where they can split fast and shatter into pieces that are thrown at high velocities. The sudden release of pressure, fragments etc. is hazardous to equipment or personnel nearby, which would cause tragic outcomes and lead to both

personnel and economic losses [37]. Some typical tragedy cases in history were caused by brittle fractures [37-40].

In terms of CFRP, at primary stage, many attempts have been made to improve the toughness of epoxy matrix.

Using rubber-modified matrix can be regarded as one of the earliest established concepts [41-45]. Jang and Yang [46] reported the delamination toughness of CF/polybenzoxazine composites were improved by rubber modification and a better interfacial bonding could be found in in amine-terminated butadiene acrylonitrile rubber (ATBN) than in carboxyl-terminated butadiene acrylonitrile rubber (CTBN) as shown in Figure 1-12.

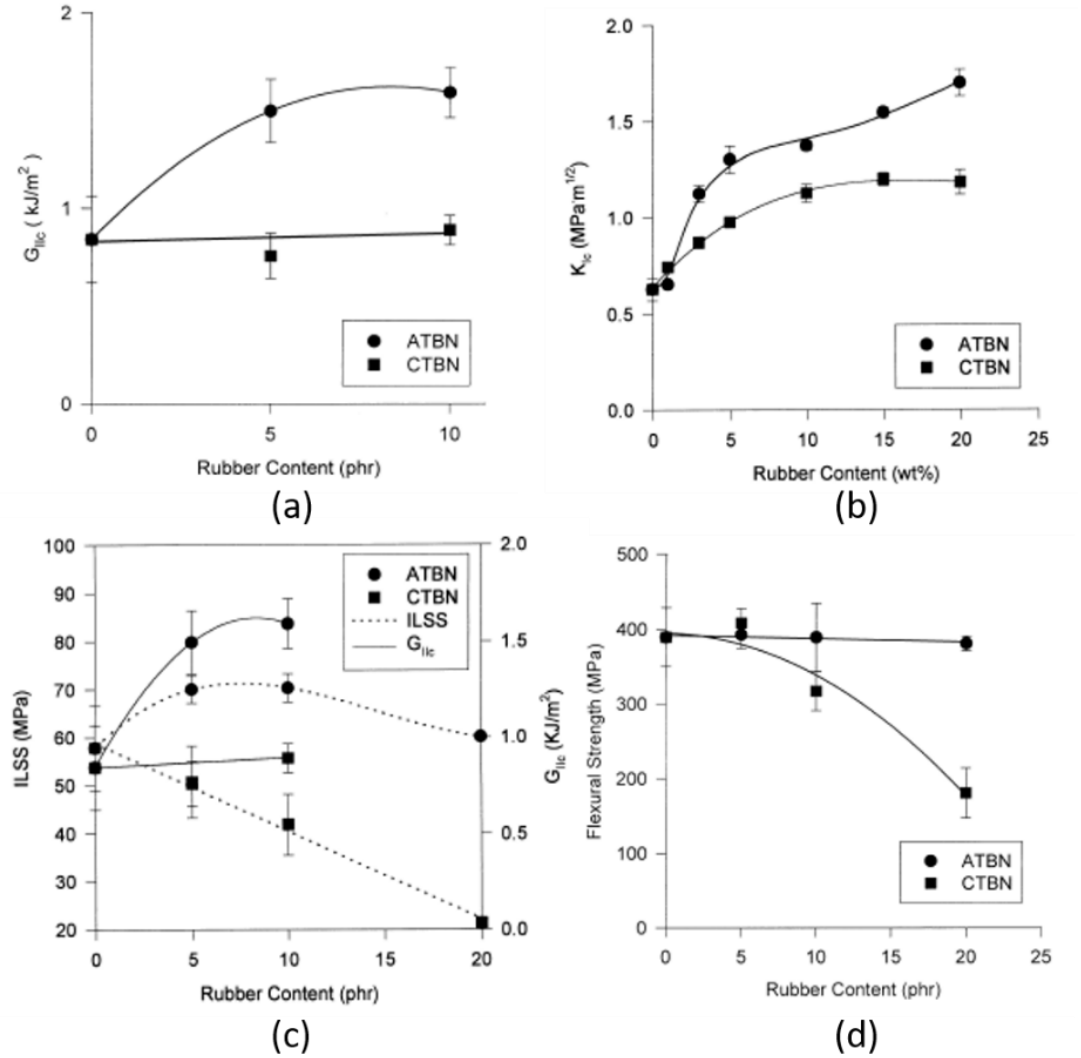

Figure 1-12 (a) G_{IIc} , (b) K_{Ic} , (c) ILSS, (d) Flexural strength of CF/polybenzoxazine composites as a function of rubber content [46]

Thermoplastics with relatively high glass transition temperature, T_g , have been used as replacement or toughening agent to improve toughness and have gained rapid acceptance since 1980s because of its relatively high mechanical property and stability [47]. Selezneva et al. [48] and Swolfs et al. [49] found utilizing polypropylene (SRPP) into carbon fiber-reinforced polypropylene (CFRPP) is possible to introduce ductility (Figure 1-13) and different damage mechanisms were investigated through carbon fiber volume fraction, the directionality of CFRPP and SRPP and layer thickness.

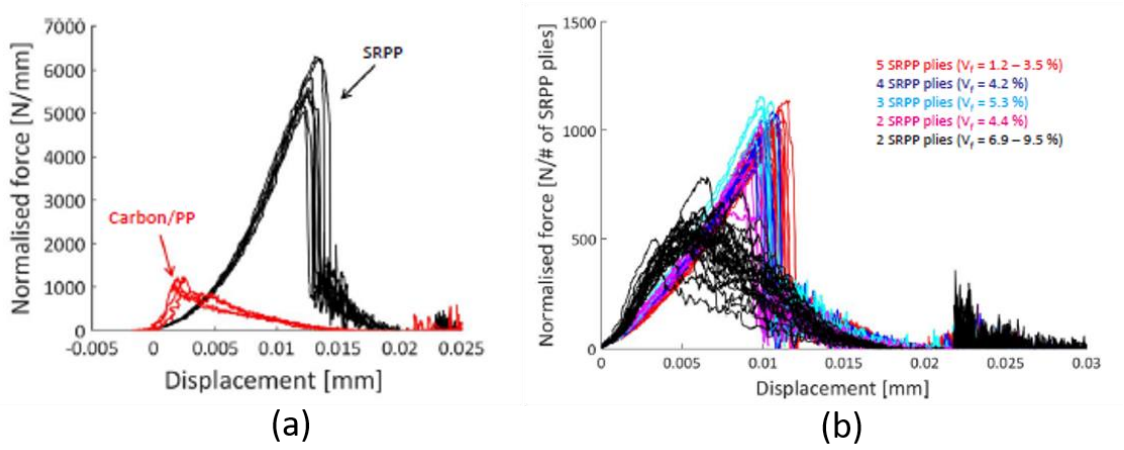

Figure 1-13 Impact force-displacement of (a) Carbon/PP vs. SRPP and (b) their hybrid [48]

Fiber coating is another method to improve the toughness of CFRP through modifying the interlaminar shear strength and the stress field, and reducing the stress gradient between fiber/matrix [50-55]. Liu et al. [55] used a sizing that consists of a thermoplastic polymer solution and a compatible amine monomer to coat CF. It was found that the re-size CF had better interfacial adhesion (Figure 1-14) and the fracture toughness of related CFRP was proved to be improved analytically.

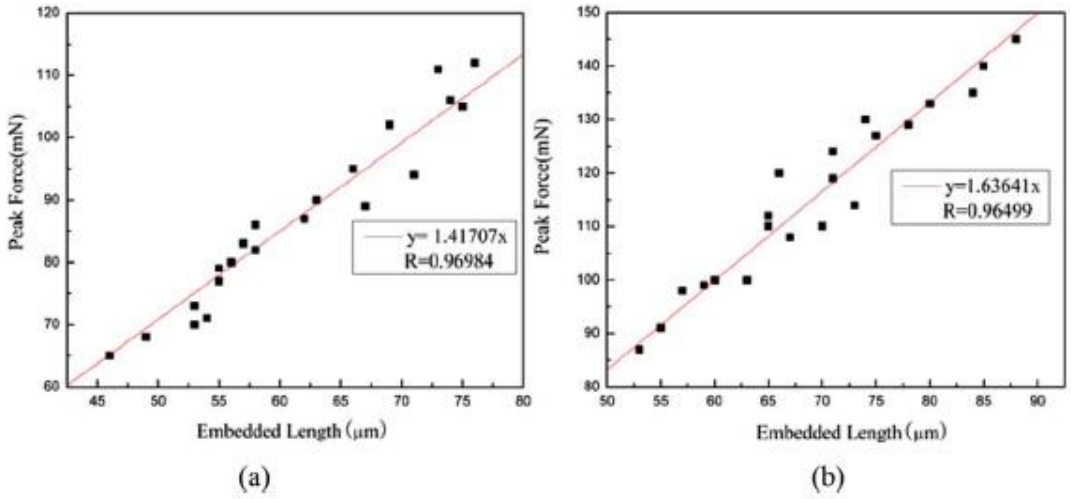

Figure 1-14 micro-bond test: (a) T700 and (b) re-size CF [55]

More recently, the use of nano rubber particles or other nanoscale fillers such as carbon nanotubes has gained much attention [56-62]. Yokozeki et al. [61] introduced several techniques to enhance the interlaminar fracture toughness of CFRP laminates using cup-stacked carbon nanotubes (CSCNTs) (Figure 1-15) which were proved contributive to improve fracture toughness of CFRP (up to 300%).

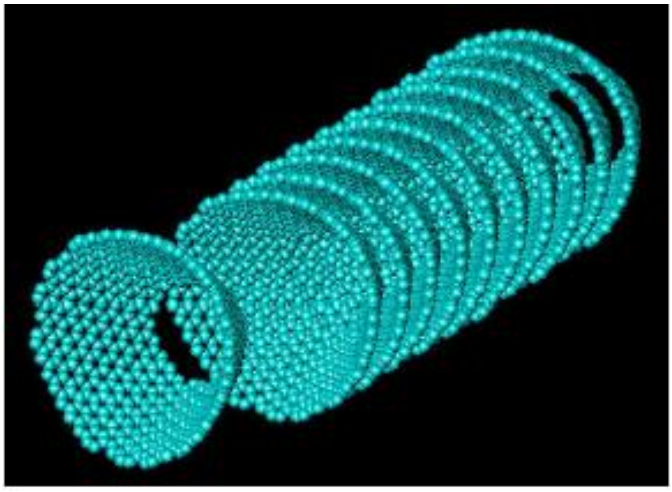

Figure 1-15 Cup-stacked carbon nanotube, CARBERE® [61]

Fiber hybridization is another promising and efficient approach. This method allows ductile fibers like glass fiber, aramid fiber etc. to incorporate with CF and improve fracture toughness of CFRP

in fiber component aspect. Most studies about hybridization have concentrated on the addition of glass or aramid fiber (GF or AF) to CFRP [47, 63-82]. Yu et al. [67] manufactured intermingled CF/glass fiber hybrid composite and they reported pseudo-ductility was achieved through fragmentation of the lower elongation constituent where there was a smooth transition between the elastic deformation and the damage evolution regions (Figure 1-16).

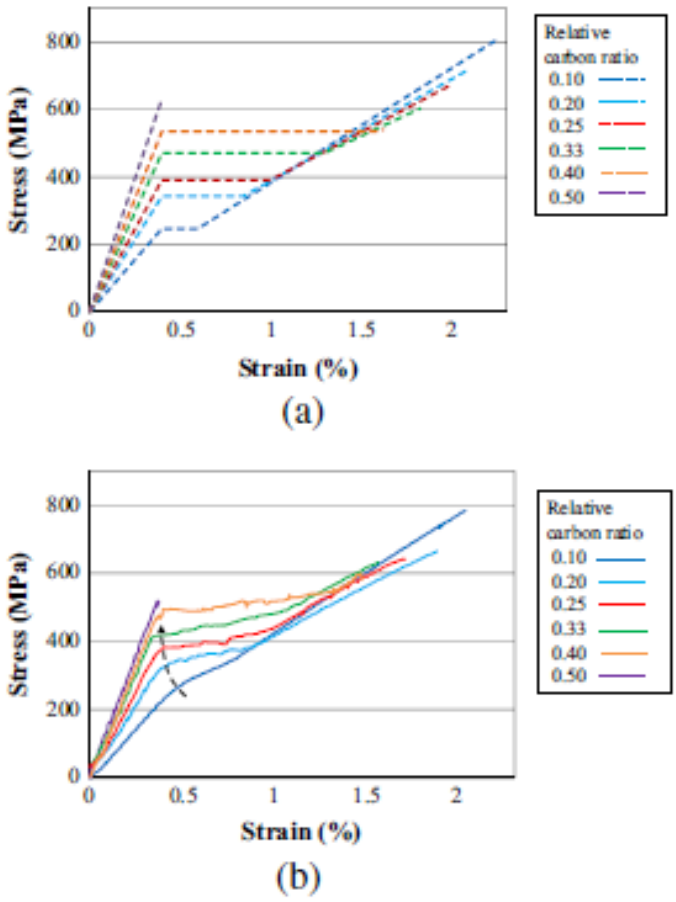

Figure 1-16 (a) Predicted stress-strain curves according to Jalalvand model and (b) representative stress-strain curves of high modulus carbon/E-glass composite samples with different relative carbon ratio [67]

However, rubber modification approach would sacrifice T_g and mechanical properties of the composites, which has limited its application. Thermoplastics have better mechanical property and stability, but even those robust and ductile thermoplastics such as Unplasticized Polyvinyl Chloride (UPVC) and polycarbonate (PC) are susceptible to brittle fracture in specific situations

[83]. Nanoparticle or nanofiller is a superior modifier to improve fracture toughness of CFRP, nevertheless, complex processing and high cost of nanomaterial restricted large-scale production [62].

Discontinuous fiber reinforced systems are usually in-plane orthotropic, and compared with continuous fiber reinforced systems, the fracture behavior is much closer to that of metallic materials. For spherical particle reinforcement, the elastic residual stress would be uniform while it would lead to local stress concentrations for those irregular shaped particles or short fibers which can affect the matrix microstructure, the properties and crack path [84]. Therefore, due to large number of fiber ends and misalignment, inner defects and voids would increase stress concentration and creates more available crack propagation paths, and discontinuous carbon fiber reinforced plastics tend to be more brittle.

In order to maintain some superior mechanical properties and manufacturing process of CFRP, the concept of localized toughening has been introduced and proved to be an alternative toughening method where ductile fiber interleaves or ductile, high performance polymer films were interlaminated into designated region of CFRP [85-90]. Wong et al. [47] combined two toughening systems, resin phase toughening and fiber phase toughening, into CFRP where phenoxy and aramid fiber interleaves were applied. A near 150% increment of interlaminer fracture toughness were found in the optimal interleaf composition. A comparison between fracture surfaces and different phenoxy concentrations is shown as Figure 1-17.

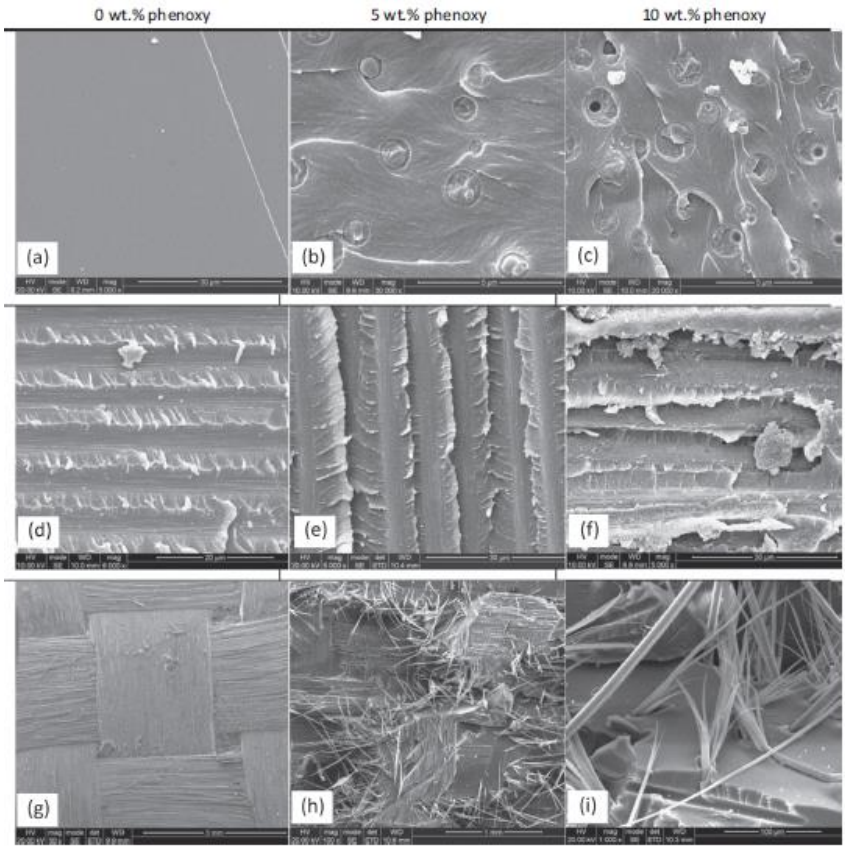

Figure 1-17 SEM image of Mode-I fracture surfaces of phenoxy/epoxy bends, phenoxy modified CFRP laminates an aramid veil interleaved CFRP laminates with fiber de-bonding at different phenoxy concentrations of: (a) neat epoxy resin; (b) 5wt% phenoxy and (c) 10 wt% phenoxy [47]

As fiber hybridization was used as a toughening approach for CFRP, to determine the toughening effect of hybrid, "synergistic strengthening" or "hybrid effect" is usually considered to be crucial. Although it is defined in different ways [70, 91-95], the most important observation is that the failure strain of the hybrid shows greater than that of pure low elongation fiber plastic.

It was reported that the degree of fiber dispersion plays a significant role in hybrid effect. Many researchers believe a finer fiber dispersion can slower development of internal damage and lead to better mechanical property and impact resistance [72, 96-104]. In the case of interlaminated hybrid, fiber positioning can also affect the impact resistance. Based on literature reviews, many reported that positioning the fibers with the high energy-absorption ability on the outside rather than on the inside allows the hybrid to absorb more energy [76, 105-108]. However, as there are

either conflicting results or insufficient data due to different materials and their interfaces, there is no clear conclusion or frame-work available to assess the deterministic material parameters [109].

In this study, fiber hybridization method was used to improve toughness of short randomly oriented carbon fiber paper-reinforced thermoplastic (CPT) where aramid fiber paper was applied as the toughening component. Effects of stacking sequence and aramid fiber length were investigated through various loadings and compared.

1.4.2.2. Deconsolidation of short rCF reinforced thermoplastic

CPT under post-thermoforming would produce deconsolidation, which demonstrates the so-called spring-back effect (Figure 1-18 and Figure 1-19) [110, 111]. During processing, stress can be introduced into the material via various mechanisms, which can result in a low quality part. In some case, release of the internal stresses during post-processing thermal treatments can result in an excessive void content, which can render the part useless. However, this production of voids in CPT can be used to produce a porous and lightweight core material to reduce the density of the composite and absorb impact energy, vibrations, compressive stress, and acoustical shock. Therefore, it was considered to be a suitable core in sandwich structure.

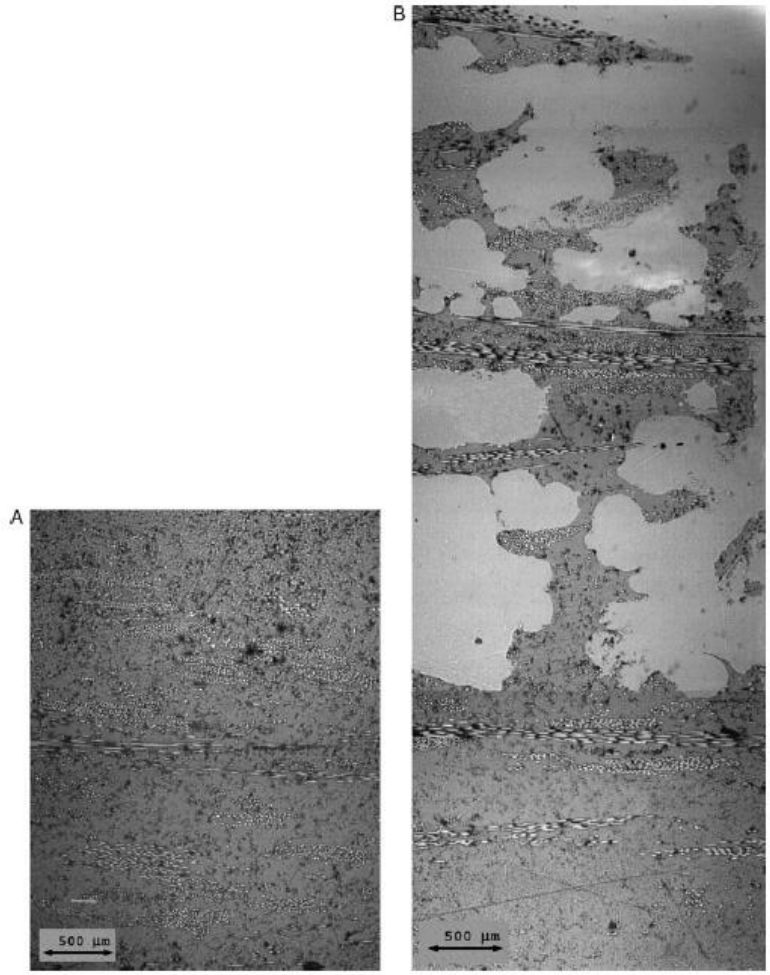

Figure 1-18 Microstructures of consolidated (A) deconsolidated (B) commingled systems; voids are seen in light grey [110]

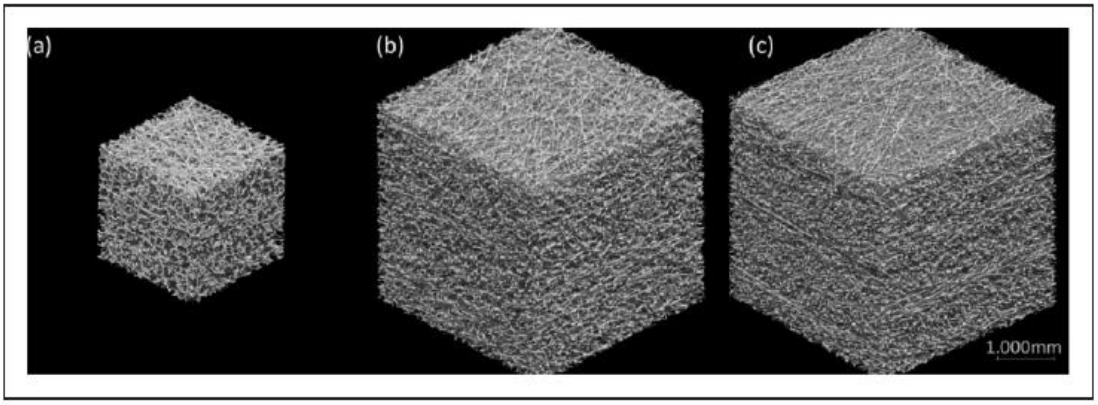

Figure 1-19 The 3D structural models of CMT 1 (a), CMT 2 (b), and CMT 3 (c) after the deconsolidation [111]

Sandwich structures commonly consist of two facing layers that bear axial and flexural loads and a light core to carry shear loads. The facing is usually made of a material with high stiffness and strength such as metals or fiber-reinforced polymers. Common core materials include foam, honeycomb or truss structures to minimize the weight of the composite [112]. Sandwich structures have found numerous applications in construction, automotive, and aeronautical applications due to their excellent mechanical properties and low weight. Allen provided a comprehensive introduction to sandwich structures and their theoretical analyses [113], which was updated by Zenkert [114].

Many researchers have studied the mechanical properties of sandwich structures under out-of-plane loading. Failure mode maps have been drawn from experimental data and predicted from simulations. For example, Triantafillou and Gibson [115] produced a failure mode map for a foam-core panel and developed equations quantifying the load at which failure occurs for each possible failure mode. Following their work, Petras and Sutcliffe [112] investigated on honeycomb sandwich structures wherein failure mode maps were derived with the core relative density and ratio of the facing thickness to span length as the axes. Vitale et al. [116] discussed and developed failure mode maps for natural and synthetic fiber-reinforced composite sandwich panels; they investigated the mechanical properties and manufacturing process, and predicted failure modes for flexural solicitations. Mostafa et al. [117] studied the flexural behavior of a polyurethane (PU) foam/glass-fiber-reinforced polymer sandwich via experimental, theoretical, and numerical comparisons. Good agreement was observed between the numerical and experimental data, while a deviation was observed in the theoretical predictions as the load increased up to the point of failure due to limitations of the calculations. An investigation of the failure behavior of sandwich beams made of unidirectional carbon/epoxy facings and PVC closed-cell foam core under three-point and four-point bending was undertaken by Gdoutos and Daniel [118]. Various failure modes including wrinkling, indentation failure, and core failure were studied and the experimental results were compared with theoretical predictions. Bau-Madsen et al. [119] conducted an experimental study of the geometrically nonlinear behavior of

a clamped sandwich structure containing aluminum facing sheets and a PVC foam core. The experiment results showed good agreement with results of a finite element analysis. Daniel and Abot [120] studied the flexural behavior of sandwich structures composed of unidirectional carbon/epoxy facings and aluminum honeycomb cores with an adhesive film. Their simplified analysis was based on a classical approach, where the nonlinear behavior of the facing material was considered and compared with experimental results.

To achieve structural integrity of the sandwich structure, the quality of adhesive bonding between the facing and core is of crucial importance. For example, honeycomb core structure provides only a small area of cell wall that can be bonded with the facing. Hence, it is necessary to improve the quality of the adhesive between the facing and core to obtain better load transfer. Joachim [121] demonstrated a peel-stopper method (Figure 1-20) for manufacturing sandwich panels that reduces the risk of catastrophic skin de-bonding, which functioned well under quasi-static conditions without sacrificing the strength of the sandwich. To examine the effect of the adhesive joint between the honeycomb core and facings on the load transfer and static response of sandwich panels, Burton and Noor [122] developed detailed finite element models using 3D solid elements to describe the total strain energy of each panel. Mostafa et al. [123, 124] demonstrated semi-circular shear keys inserted between glass-fiber-reinforced polymers sheets and two types of foam cores to increase skin-core de-bonding resistance and shear performance (Figure 1-21); the flexural stiffness and strength of the panel were significantly improved by the use of shear keys, which correlated well with analytical results. Åkermo and Åström [125] presented a numerical example to illustrate the predicted matrix flow from 12 glass fabric-reinforced polyamide facings to the expanded closed-cell polymethacrylimide foam core and compared the results with an experimental study. Rion et al. [126] used adhesive deposition method (Figure 1-22) and developed a model to predict the fillet size as a function of the properties of different sandwich structures, aiming to predict the debonding energy. The quantity of adhesive used for facing-core bonding could be tailored, where it was possible to study the size and shape of the meniscus over a wide range of adhesive quantities (8-80 g/m^2). Grove et al. [127] investigated the dependence of the quality of the facing-core bonding achieved using a range of different processing parameters on the peel strength of Nomex honeycomb core/CF-epoxy prepreg facing sandwich panels.

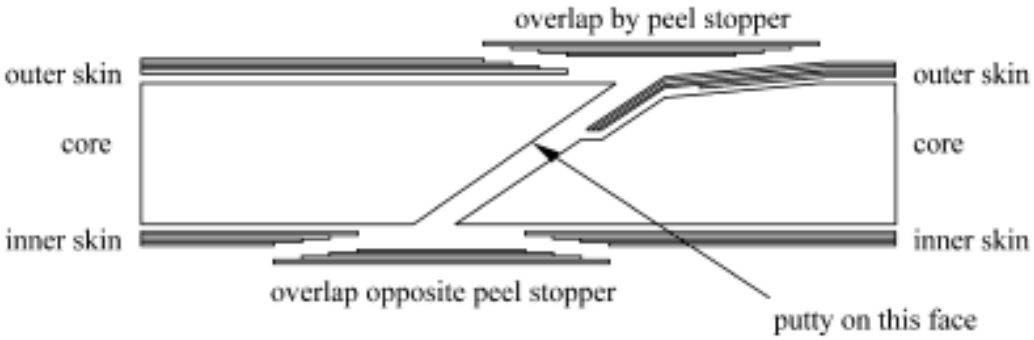

Figure 1-20 Schematic of the combined peel-stopper and joint [121]

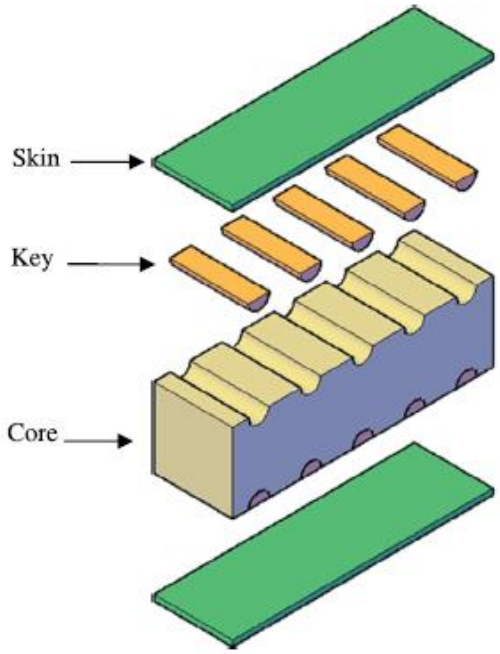

Figure 1-21 Sandwich panel with shear keys methodology [123]

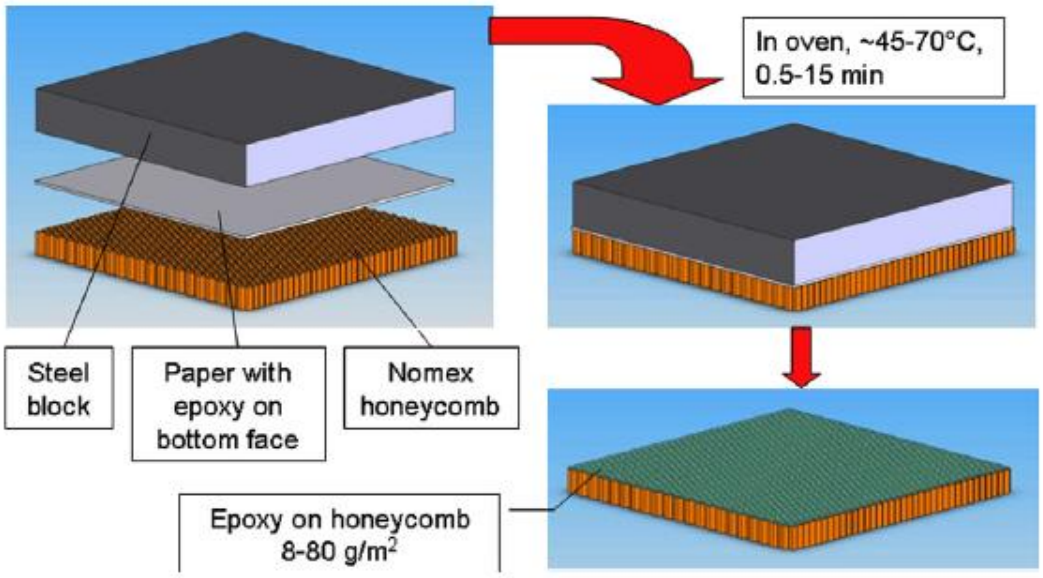

Figure 1-22 Adhesive deposition method [126]

Sandwich structures are recognized for being lightweight and for their good in-plane mechanical properties. However, in most cases, they do not perform well in their thickness direction as the core material is generally weak due to its high porosity, and de-bonding or delamination occurs due to poor facing-core adhesion and poor inter-laminar shear property. Many techniques have been developed for reinforcing laminate polymer composites in the out-of-plane direction to enhance the delamination resistance and improve the mechanical properties along the thickness [128]. Most common through-thickness reinforcement techniques involve the use of fabrics with long filaments or discontinuous unidirectional prepregs, including 3D weaving [129-131], stitching [132-134], z-pinning [128, 135-137], and tufting [138] methods. Grogan et al. [129] tested vehicle armor panels with 2D and 3D woven composite backings. After ballistic tests, the armor panels with 3D woven backing (Figure 1-23) showed higher ballistic efficiency than 2D baseline panels, with controlled delamination and fewer complete penetrations. Xia et al. [139] found that through-thickness-stitched foam sandwich composites (Figure 1-24) are capable of bearing a high impact load by absorbing more impact energy, while exhibiting lower impact damage, compared to equivalent unstitched samples. Using fibrous z-pins (unidirectional carbon filament rods), Nanayakkara et al. [136] determined the influence of the volume content, size, and end constraint of orthogonal z-pins on the compressive stiffness, strength, and strain energy absorption of sandwich composites (Figure 1-25). Henao et al. [138] conducted edgewise

compression and three-point bending tests on tufted and non-tufted sandwich panels (Figure 1-26) made of combinations of carbon/epoxy and E-glass/epoxy facings and PVC and polyurethane foam cores with different tufting densities. A significant increase in strength was observed when tufted reinforcement was applied. A developed finite element model agreed well with the experimental study.

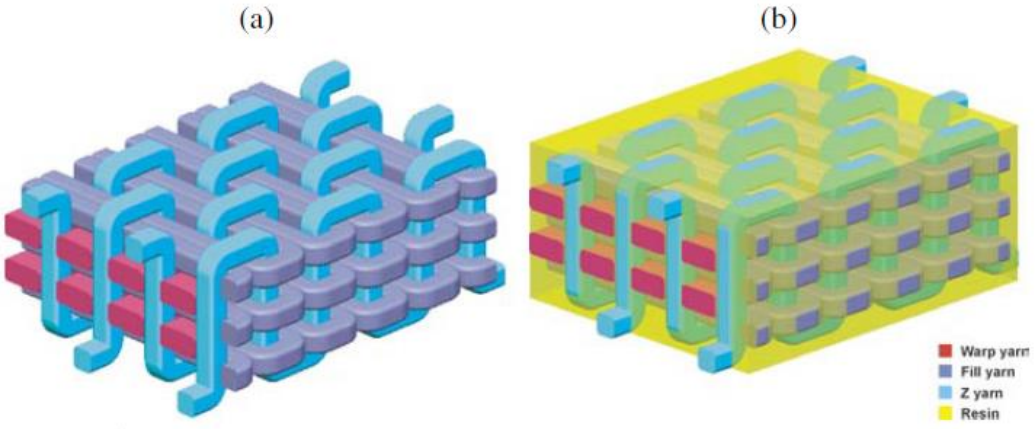

Figure 1-23 Geometric model of 3D orthogonal: (a) woven fabric and (b) composite matrix material is shown as transparent yellow [129]

Figure 1-24 Pictures of the front surface and cross-sectional view of through-thickness stitched sandwich [139]

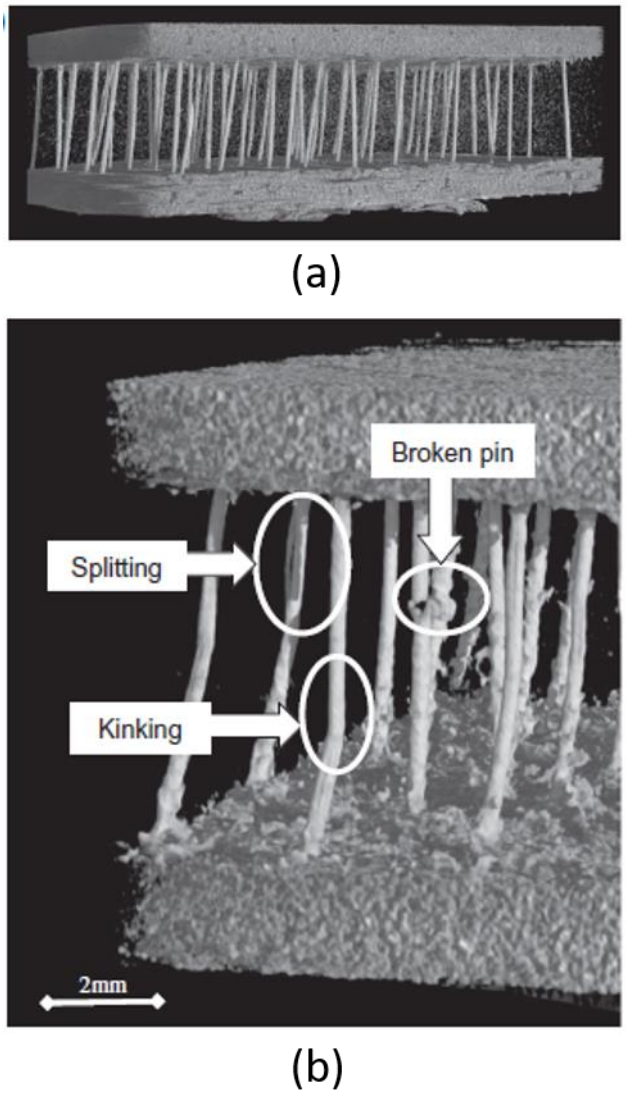

Figure 1-25 X-ray computed tomography image of an untested z-pinned sandwich composite specimen (a) and the one following elastic compression loading (b) [136]

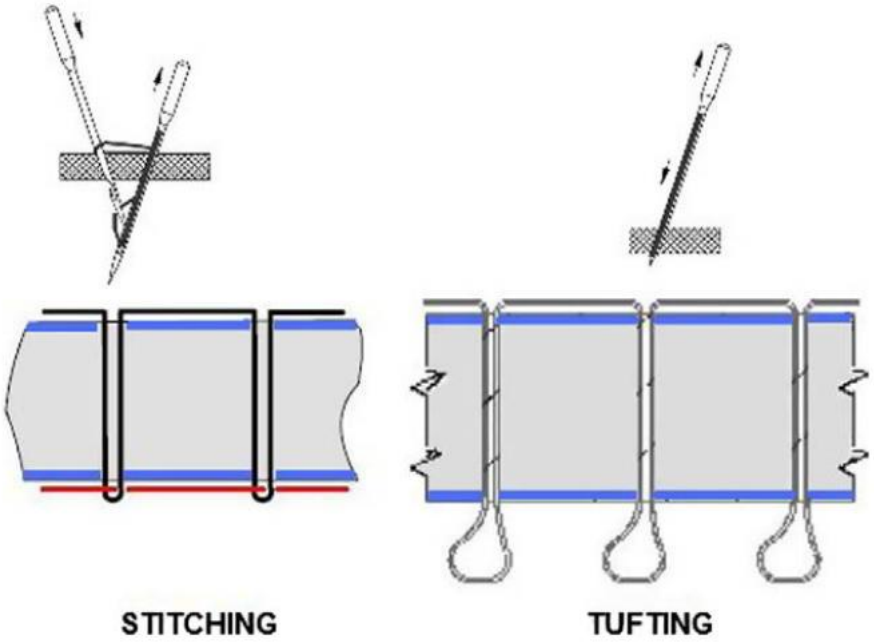

Figure 1-26 Schemes of stitching (Left) and tufting (left) applied to sandwich panels [138]

We performed preliminary experiments and observed that the spring-back effect of a CPT core could be used to produce a sandwich structure with low density. This satisfied our primary goal to achieve a high stiffness-to-weight ratio composite and inspired the detailed investigation of this material described here.

1.5. Research objective and outline

The structure of this thesis is shown in Figure 1-27.

In Chapter 1, firstly the general introduction of CF and CFRP were given. And then, the current status of carbon fiber recycling was presented. The problems and solutions were illustrated by literature reviews. The final part is the outline of the thesis.

In Chapter 2, a carding and stretching system was introduced to improve fiber alignment for rCF to make card web carbon fiber reinforced thermoplastics (CWTs). A series of mechanical tests was conducted on several types of CWT. In addition, X-ray micro-computed tomography

scanning analysis was applied to evaluate fiber orientation distribution. The effect of alignment on CWT was also investigated analytically.

In Chapter 3, CPT was hybridized with aramid fiber papers (AP) to improve toughness. In the first half of the chapter, the hybrid effect was investigated through stacking sequence where interlaminer number and carbon fiber layer on the outside or opposite positioning in interlaminated hybrid were tested and compared. In the last half of the chapter, using the optimal stacking sequence in the first half of study, interlaminated hybrids with handmade AP were produced and compared with intermingled hybrids with handmade carbon fiber/ aramid fiber (CF/AF) papers through various mechanical loadings and observation.

In Chapter 4, CPT with polypropylene (CPT-PP) or with polyaminde-6 (CPT-PA6) being subjected to different levels of thermal deconsolidation was applied as cores to be sandwiched with strong faces, chopped CF tape-reinforced thermoplastics (CTT) or unidirectional carbon fiber prepreg (UD). The sandwich was molded by various forming method which got rid of the process of the face and core molding separately and the adhesion. In the case of CPT-PP sandwich, to improve the properties of the structure along the thickness direction to prevent delamination, preformed sheets were subjected to needle punching. And the comparison was made through the different consolidation levels on the flexural behavior and the impact property of both CPT-PP and CPT-PA6 core sandwich beams.

In Chapter 5, a summary of the whole thesis was presented.

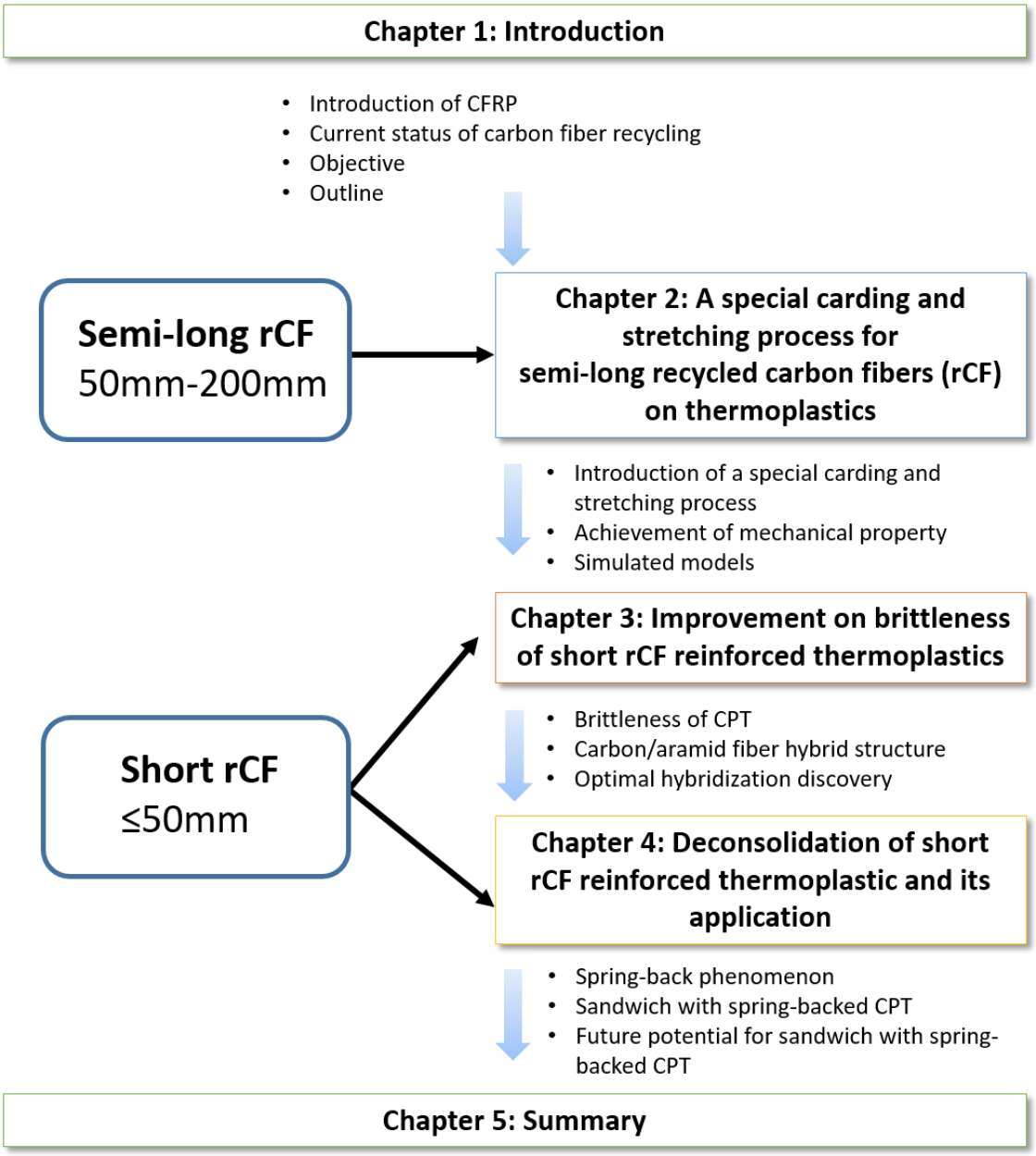

Figure 1-27 The main content of the doctoral dissertation

2. A carding and stretching process for semi-long rCF on thermoplastics

2.1. Introduction

In this chapter, a carding and stretching system was introduced to make CF card web sheet by blending 50-mm long CF and special synthetic polyamide fibers together. Sheets with several kinds of V_f and stretching levels were produced and molded into carbon fiber card web reinforced thermoplastic (CWT). In order to investigate its mechanical properties, tension, flexural, and izod impact loadings were conducted and compared for different types of CWT. In addition, X-ray micro-computed tomography analysis was performed to evaluate the fiber alignment level or fiber orientation distribution (FOD).

Analytical models for prediction of elastic properties in short fiber systems have been developed and validated by some researchers [27-29]. In this section, the elastic moduli of composites were analyzed using a simulated laminate model. Netting analysis was also applied since it is another approach to calculate ply stresses and is often used for helically wound reinforced pressure vessels and tubes [31, 140]. Although netting analysis has been regarded as a limited case of the laminated structure, it is an excellent basis for quick estimation and an approximation of the response of a composite. We used it to compare with classic laminate theory and evaluate the effect of fiber orientation.

2.2. Materials and methods

2.2.1. Materials

To ensure the validity and reliability of both the experimental and analytical results for the method used in this research, rCFs were replicated using vCFs (TORAYCA T700S). The vCFs were

uniformly cut into 53-mm long pieces, and then desized by fully soaking in acetone solvent for 24 h and washing thoroughly. The desized CFs were observed using scanning electronic microscopy (SEM, Keyence Corporation) as shown in Figure 2-1; the sizing was almost completely removed from the surface. The desized CFs were then mixed and opened randomly using an OP-300 opener from Takeuchi Works Co. Ltd (Figure 2-2). A type of synthetic PA fiber of fineness 1.7 dtex, length 51 mm from Unitika Ltd. was introduced as a matrix fiber; it has shell of polyamide 6 (PA6)–polyethylene (m.p. 136 ℃) copolymer and a core of polyamide 66 (PA66), as shown in Figure 2-3. A necessary amount of CF and resin fibers for 20, 30, and 40% CF volume fraction (Vf) were prepared.

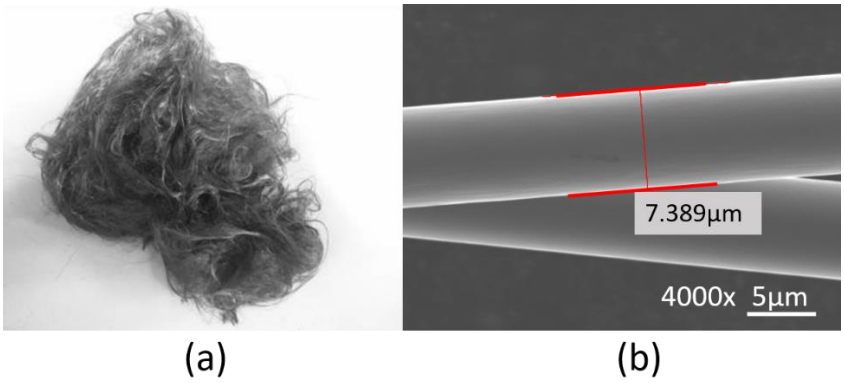

Figure 2-1 Scanning electron microscope observation of the fiber morphology of the CF after being de-sized

Figure 2-2 The opening and mixing of CF and PA fibers

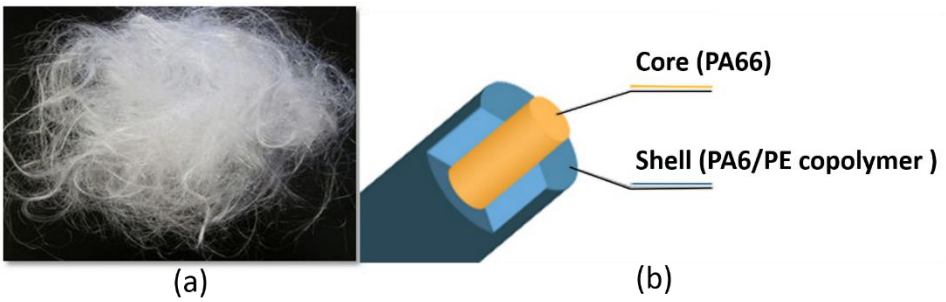

Figure 2-3 The appearance and structure of the synthetic PA fiber

2.2.2. Carding and stretching process

2.2.2.1. Carding process

A modified carding machine from Takeuchi Works Co. Ltd. was used to make CF card web preforms; it consists of several rollers with wire pins covering the surfaces. The rollers were positioned in pairs to produce different functions as pin direction and rotation speed vary in individual rollers. A schematic of the carding process is shown in Figure 2-4. The whole operation area was divided into several zones: take-in zone, carding zone, doffer transferring zone, and web formation zone. In the take-in zone, fibers were stripped from feed rollers and transferred to the carding zone where the main cylinder cooperates with several worker/stripper pairs to loosen up fiber aggregation and re-arrange fiber orientation through the path between pins along with the rotation direction of the main cylinder. In the doffer transferring zone, carded fibers were stripped from main cylinder and then raised from doffer and formed web on the web formation zone. Finally, the web was rolled onto a reel.

Before making the CWT preforms, the appropriate settings for good processing speed were found for all roller pairs and the conveyer belt in order to avoid unnecessary damage to the CFs. Subsequently, a suitable amount of cut CF and a calculated amount of resin fibers based on a determined volume fraction were fed and carded. The size of each carded web was 96 × 25 cm, and the basis weight of the CWT preforms was approximately 100 g/m^2.

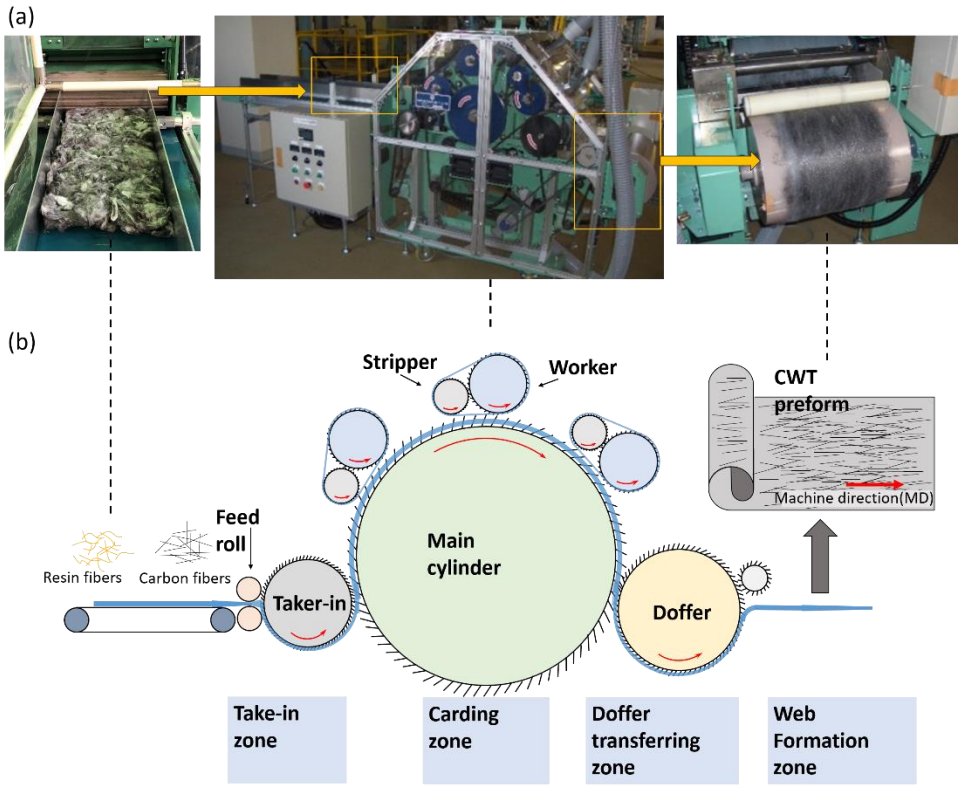

Figure 2-4 The carding process (top: actual setup; bottom: functional sketch)

2.2.2.2. CWT sheet preparation under stretching process

Post-thermal treatment is necessary because the CWT preform can easily lose its shape and break apart upon simple friction forces between the two types of fibers without adhesion. Therefore, after being carded, the CWT preform was thermally bonded by calendaring at a temperature of 110 ℃, and passing through a pair of rollers with a 0.10 – 0.15 mm gap. In this process, the shell part of the resin fiber would partially melt and bond around the fibers, while the other fibers would not be affected.

rCFs are usually in a state of disorder since they have been retrieved from broken parts. They may have suffered from matrix detaching by a series of physical, chemical, and thermal treatments, which can cause severe loss of mechanical performance upon reuse. In order to restore the mechanical properties as much as possible, one approach is to improve the degree of alignment. Although the carding process can significantly re-align fibers, it still has limitations. To achieve a higher fiber-alignment degree, a stretching process was applied to the CWT preforms. The CWT

preforms were fed into a stretching machine, where roller pairs were set under different rotation speeds to produce a tensile force on the CWT sheet. At the same time, the CWTs were heated to above 170 ℃, which is above the melting temperature of the shell and lower than that of core of the PA fiber. In this way, the core of the PA fiber would not melt or tear apart, so that the sheet structure can be maintained even at a high stretching level. Here, we define the term stretch ratio (S-ratio) to represent the stretching level of the thermally bonded and stretched CWT sheets; S-ratio = $(L' - L)/L \times 100\%$, where L is the length of original CWT sheet, and L' is the length of stretched CWT sheet, as shown in Figure 2-5.

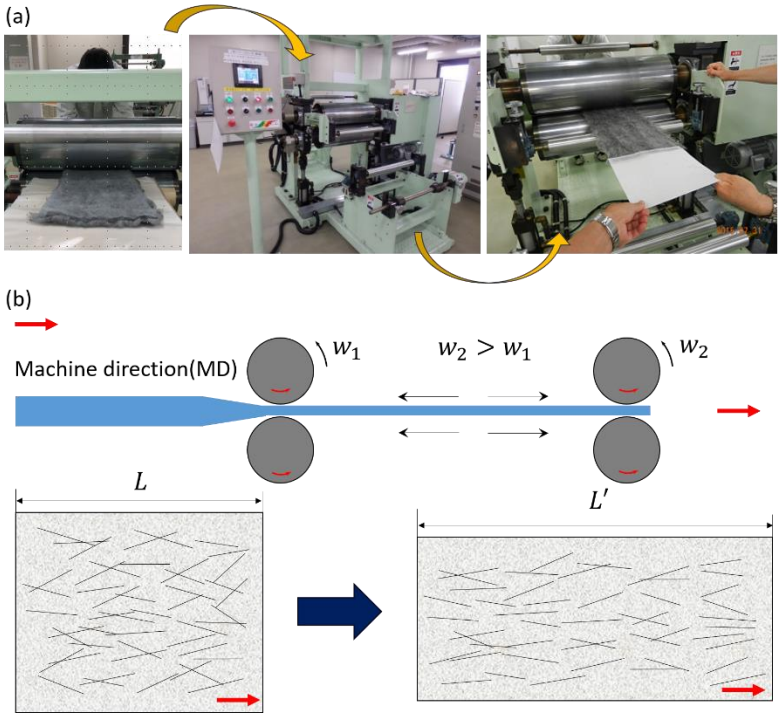

Figure 2-5 The stretching process (top: actual setup; bottom: functional sketch)

2.2.3. Molding

Before panel molding, CWT sheets were cut into pieces in the longitudinal direction (L) and transversal direction (T) to fit a molding die of 250 × 125 mm. Then, they were stacked unidirectionally and dried in an oven at 90 ℃ for 48 h. The CWTs with different CF fractions and S-ratios were denoted as "S*a*-CWT*b*-L/T", where *a* and *b* represent the S-ratio (%) and CF volume fraction (%), respectively. Panels were molded by compression molding using a hot compression machine. The molding temperature was set at 280 ℃, while the molding pressure

differed depending on the CF volume fraction to achieve good resin infiltration and less void content. For CWT20, CWT30, and CWT40, the molding pressures were 5, 7, and 9 MPa, respectively. The temperature and pressure profiles of the molding procedures are shown in Figure 2-6.

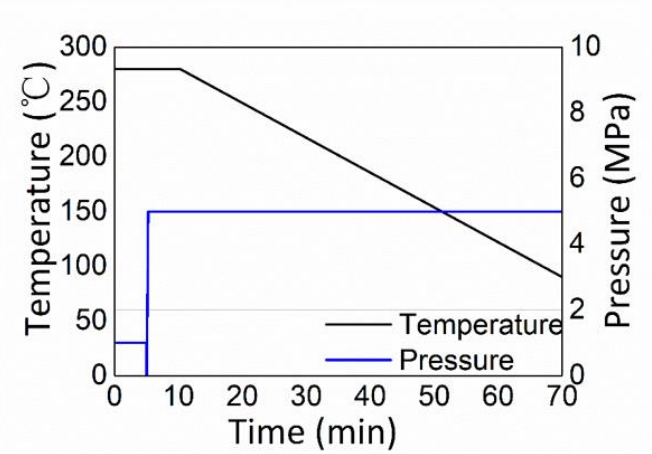

(a)

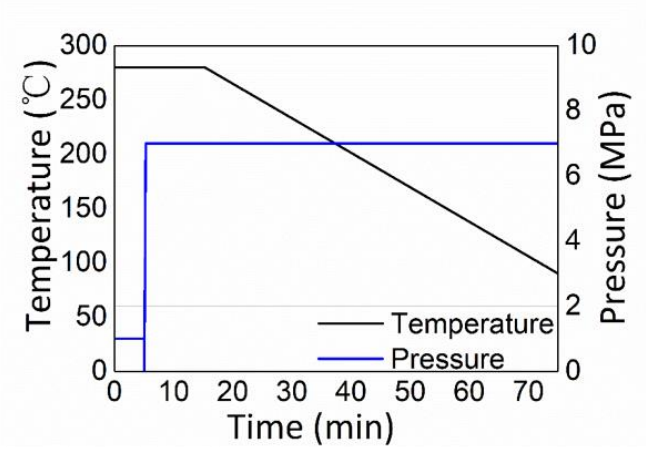

(b)

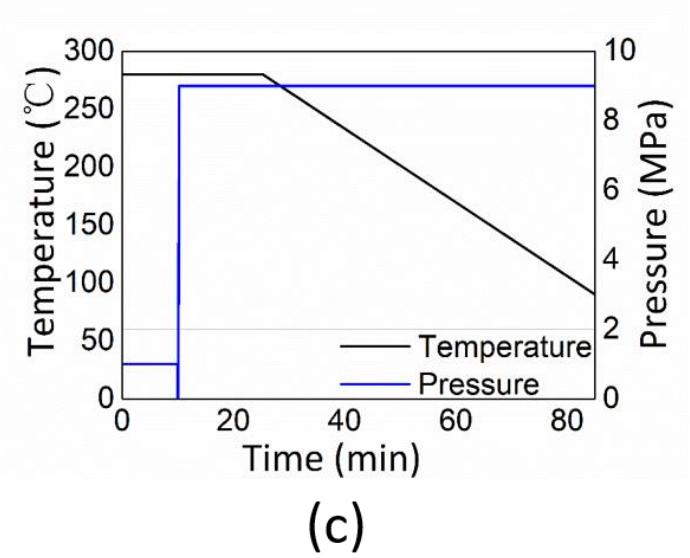

Figure 2-6 Molding programs: (a) CWT20 (b) CWT30 (c) CWT40

2.2.4. Experiment

2.2.4.1. Ash test

In order to qualitatively and quantitatively assess the correlation between V_f and mechanical properties, the actual V_f and void content ratio V_v of each CWT panel were obtained by measuring ignition loss of polymer matrix at inert gas atmosphere. Five coupons with dimensions of 15 × 15 mm were created according to the JIS K 7075 standard by electric densimeter (MDS-300, Alfa Mirage Co., Ltd.). V_f and V_r were easily obtained by measuring the weight of the specimen before and after ignition. In terms of V_v, it is obvious that $V_f + V_r + V_v = 1$ and $W_f + W_r = 1$; $\rho_c = \rho_f V_f + \rho_r V_r$, where V_r is volume fraction of resin, W_f and W_r are the weight fractions of CF and resin, respectively, and ρ_c, ρ_f, and ρ_r are the densities of composite, CF, and resin fiber, respectively. Because $W_f = \rho_f V_f/\rho_c$; $W_r = \rho_r V_r/\rho_c$, $V_v = 1 - \rho_c(W_f/\rho_f + (1 - W_f)/\rho_r)$.

Three kinds of ash test conditions were conducted as shown in Table 2-1. The validity of the test conditions were confirmed by SEM. The fiber morphology of CF under different test conditions are given in Figure 2-7. It can be seen that in condition 1, residual polymer is clearly evident on

the surface of the CFs; in condition 2, the polymer was fully removed but the fiber surface was oxidized and deteriorated, which could affect the results; in condition 3, most polymer was removed and the morphological integrity of CF was able to be maintained. Thus, the ash tests were operated under condition 3: 500 ℃ for 2 h. The fiber morphology after the ash tests is given in Figure 2-8 at lower magnification. Most polymer had been removed from the surface of CFs, which indicates the condition for ash test was reliable and the calculation of fiber volume fraction can be trusted.

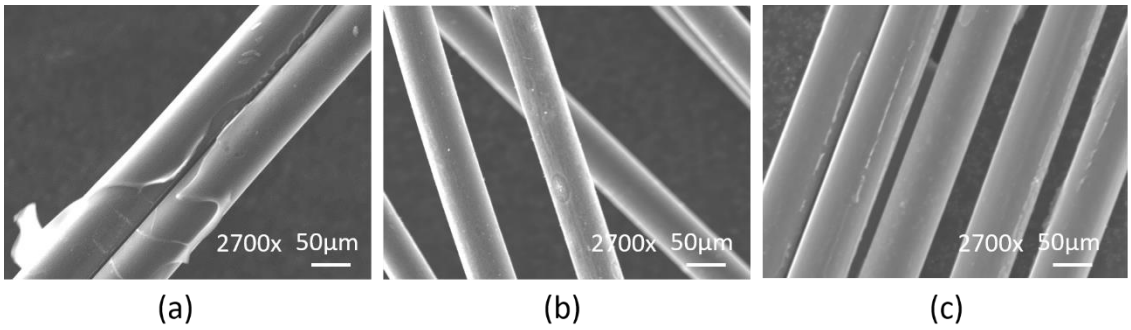

Figure 2-7 SEM images of the CF morphology after ash testing under: (a) condition 1, (b) condition 2, and (c) condition 3 (See **Error! Reference source not found.**)

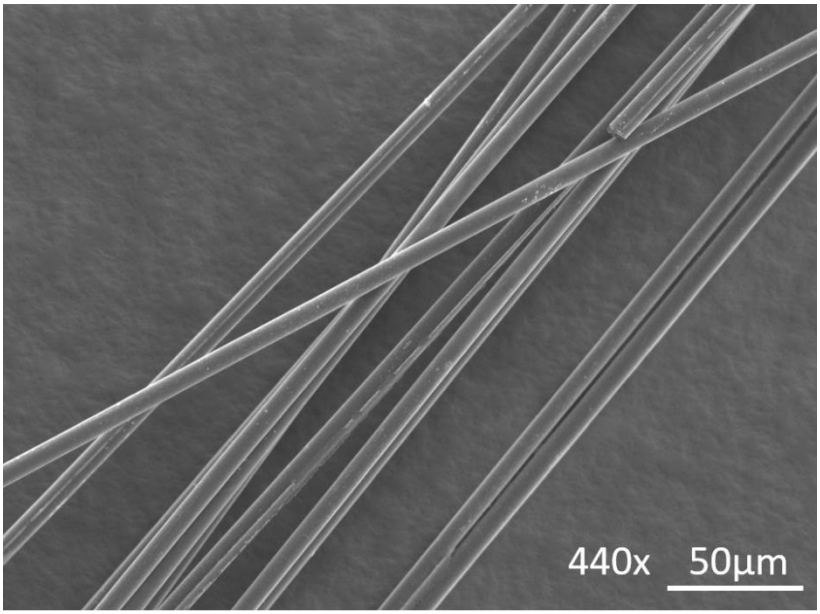

Figure 2-8 SEM image of the CF morphology after ash testing under condition 3 (See **Error! Reference source not found.**)

Table 2-1 Ash test conditions.

	Condition 1	**Condition 2**	**Condition 3**
Temperature [℃]	500	550	500
Time [h]	1.5	1.5	2.0

2.2.4.2. Tensile test

Tensile test was performed with 80-mm gauge length for measuring the strain in the load direction.

A schematic of the set-up for the tensile test is shown as Figure 2-9.

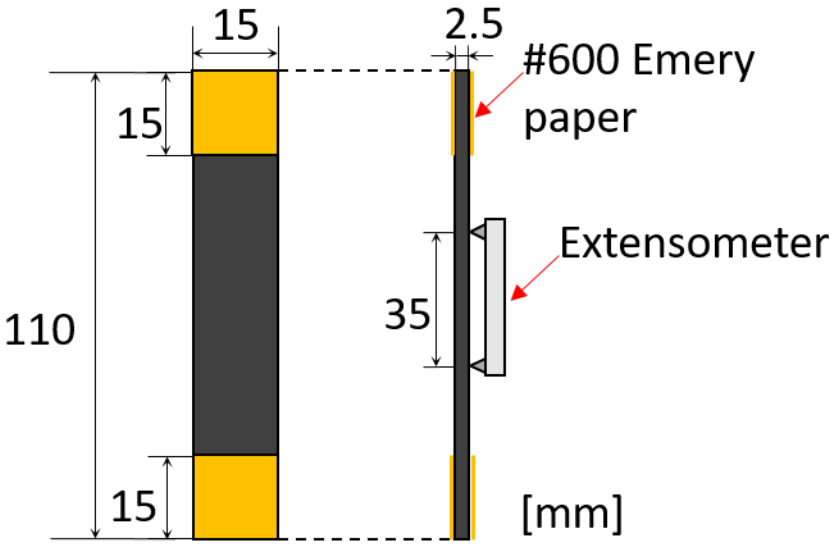

Figure 2-9 Schematic of the set-up for the tensile test

2.2.4.3. Three point bending test

Flexural property was measured in accordance with JIS K 7074 using a universal testing machine (AUTOGRAPH AGS-X 5KN, Shimadzu Co.). Five coupons were prepared for each type in the L-direction and T-direction, respectively. The dimensions of each specimen were 50 × 10 × 2 mm.

The span length was 32 mm and a span-to-depth ratio of 16:1 was applied. The crosshead speed was 1 mm/min.

A schematic of set-up for the tensile test is shown as Figure 2-10.

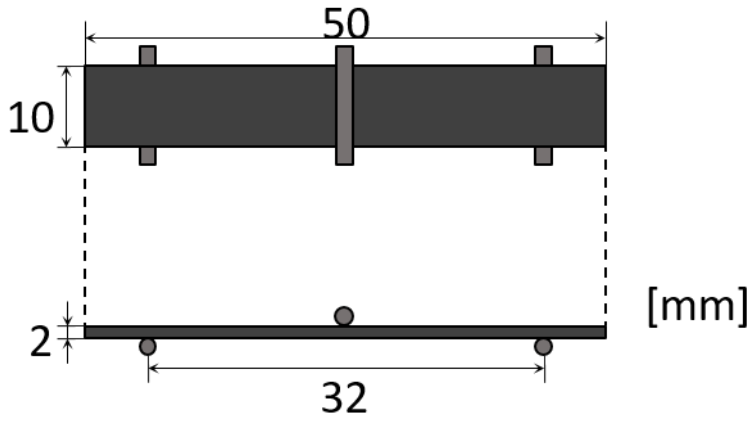

Figure 2-10 Schematic of the set-up for the three-point bending test

2.2.4.4. Izod impact test

Based on the JIS K 7110 standard, CWT specimens were also tested in Izod impact loading with a pendulum impact tester (Dynatup POE2000e, Instron Engineering Corporation) to understand their energy absorption capacities. The weight of hammer was 11.975 kg and the swing-up angle was 50°, so the impact speed was approximately 1.5 m/s. Five coupons were prepared and tested in the L-direction and T-direction, respectively. The dimensions of each specimen were 50 × 10 mm.

A schematic of the set-up for the Izod impact test is shown as Figure 2-11.

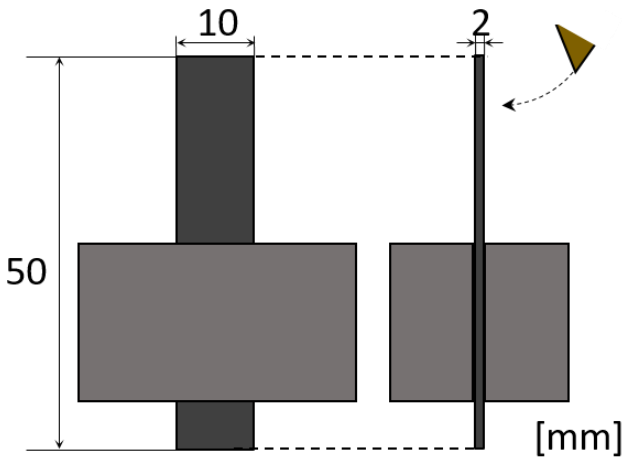

Figure 2-11 Schematic of the set-up for the Izod impact test

2.2.4.5. X-ray micro-CT scanning

The internal structures of the CWT panels for tensile test were scanned using a TDM1000-II 3D X-ray micro-CT scanning system (YAMATO Scientific Co., Ltd). Five coupons of 50-mm in length, 2-mm in width, and 2-mm in depth were chosen from different positions in each panel and cut. A scan voltage of 38 kV and scan current of 38 mA were used. A schematic of the scanning process is shown as Figure 2-12.

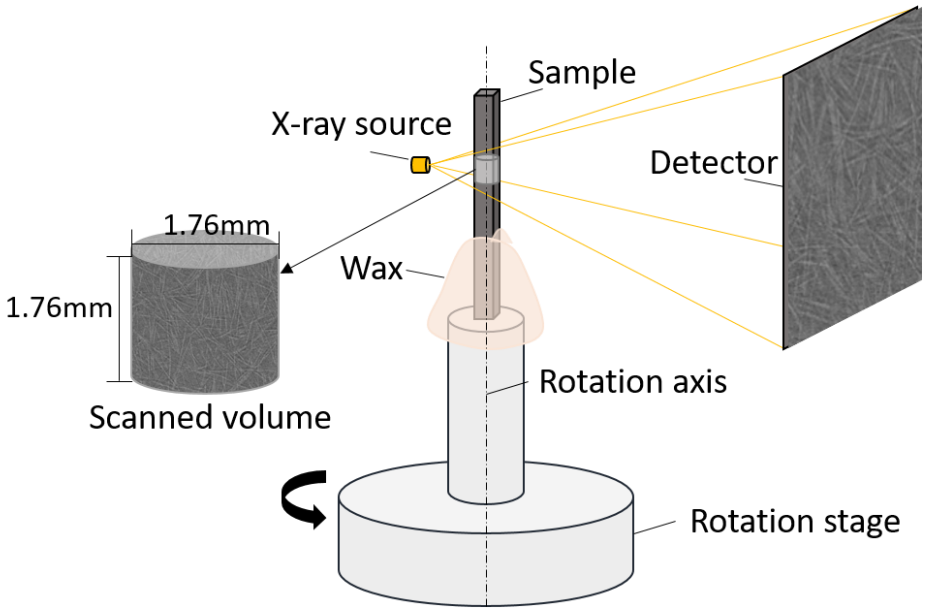

Figure 2-12 Schematic of X-ray scanning process and scanned volume

2.3. Results and discussion

2.3.1. Test results

2.3.1.1. Ash test

The actual values of V_f and V_v used in the evaluations were calculated by ash testing; the values are shown in Table 2-2. The results indicate that the void content increases as CF volume fraction increases. Although the CFs in the CWTs had been carded and the alignment degree of CFs had been improved, a certain amount of CFs still perturbed in various directions ranging from 0°-180° in the plane and even off the plane. When many CFs overlap and contact with each other, it is inevitable that many small spaces that are difficult for the resin to infiltrate. Considering the stretching ratio, in the case of CWT with 30% V_f, the stretched CWT showed lower void content compared to un-stretched. As mentioned above, this was because the created spaces in stretched CWT were less common than in non-stretched CWT. However, this tendency was not observed in the case of CWT with 40% V_f. In the carding machine, there is a limitation in the feeding amount of fibers, and 40% CF content caused fiber saturation on the wire pins, thereby resulting in unevenness in the carded CWT sheet. Hence, the results are irregular for CWT with 40% V_f.

In general, the actual V_f of all types of CWT is close to the expected value, and the actual V_v is within a tolerance, so the mechanical properties are comparable among all types of CWT.

Table 2-2 V_f and V_v of the specimens for mechanical tests

	Tensile test			**3-point bending test**			**Izod impact test**	
	V_f [%]	V_v [%]		V_f [%]	V_v [%]		V_f [%]	V_v [%]
CWT20	20.3	0.2	CWT21	21.4	0.9	CWT21	21.4	0.9
CWT30	30.3	1.0	CWT31	30.7	1.7	CWT31	30.7	1.7
S30-CWT32	32.0	0.6	S30-CWT29	29.3	1.3	S30-CWT31	31.3	1.7
S60-CWT35	34.7	0.6	S60-CWT34	33.6	0.8		-	-
	-	-	CWT37	37.3	3.5		-	-
	-	-	S48-CWT43	43.4	4.6		-	-
	-	-	S68-CWT39	38.6	5.7		-	-

2.3.1.2. Tensile property

The results of the tensile tests are shown in Figure 2-13. The tensile moduli of S30-CWT32 and S60-CWT35 are 44.4 GPa and 45.6 GPa, respectively, which are even higher than that of unidirectional tape reinforced thermoplastics; the tensile strength reached 476 MPa, which is close to that of unidirectional tape reinforced thermoplastics, as shown in the study of Wan at el. [14]. The results further demonstrate that the carding process helped realign fibers and let most fibers aligned in the longitudinal direction, which creates the massive gap between the longitudinal and transverse properties (see Section 3.5.). Comparing CWT20 with CWT30, with higher CF volume fraction, both tensile modulus and tensile strength were improved because there are more CFs contributing to sustaining the loading in CWT30. It can be seen that the tensile property of the stretched CWT was improved in the longitudinal direction compared with the control, while it deteriorated in the transverse direction when stretching ratio increased, which indicates that the stretching process did partly guide further off-axis fibers to change their direction. However, the modulus of the CWTs did not improve significantly upon increasing the stretching ratio, which results from excessive stretching that caused some fibers to withdraw. Figure 2-14 shows SEM images of the fracture surfaces of CWT30, S30-CWT32, and S60-CWT35 in the longitudinal direction after tensile testing. The stretched composites exhibited more dispersed CF clusters on the fracture surfaces, which demonstrates that stretching did improve the CF alignment. However, a large amount of fiber pull-out was observed for S60-CWT35, because the excessive stretching adversely affected the fiber alignment, creating an unbalanced fiber alignment distribution. It also explains the similar mechanical performance of S30-CWT32 and S60-CWT35. Figure 2-15 compares the fracture surfaces between samples in the L and T directions; there is almost no fiber in the axial direction contributing to tensile force, which accounts for the massive gap between the properties of L- and T-aligned fibers. This demonstrates the importance of the aligning effect by the carding and stretching process. Overall, S30-CWT32 and S60-CWT35 show relatively better tensile properties than the other CWTs.

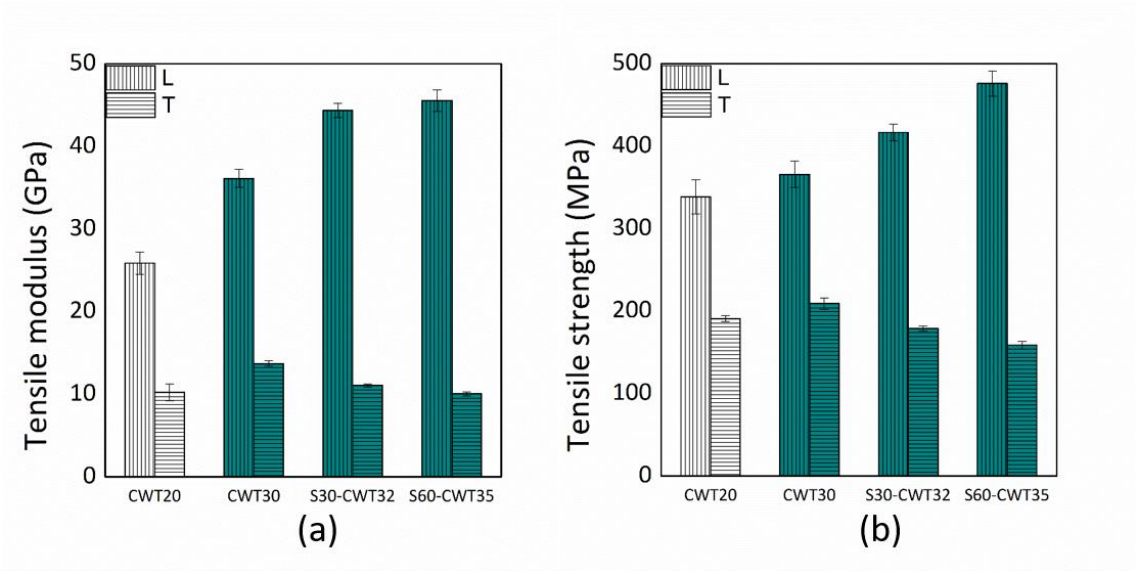

Figure 2-13 (a) Tensile moduli and (b) tensile strengths of CWT20, CWT30, S30-CWT32, and S60-CWT35

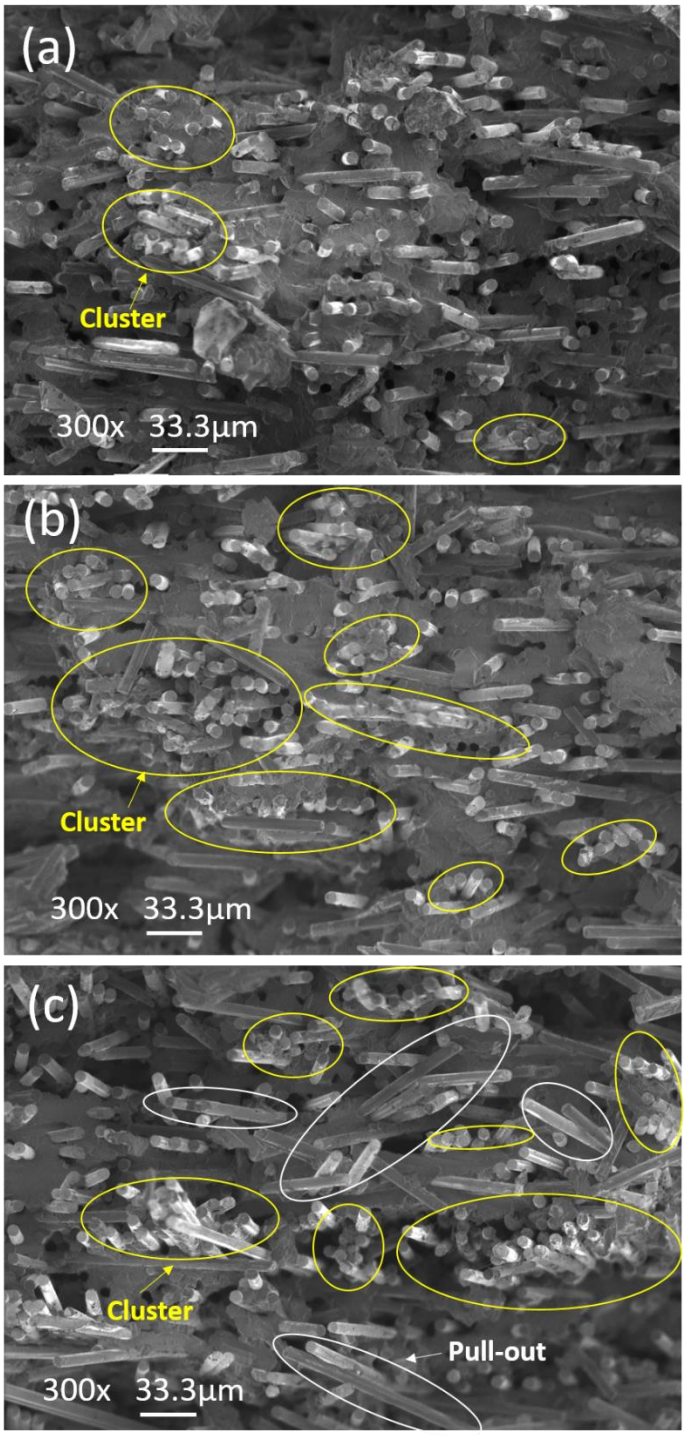

Figure 2-14 SEM images of fracture surfaces after tensile testing: (a) CWT 30-L, (b) S30-CWT32-L, and (c) S60-CWT35-L

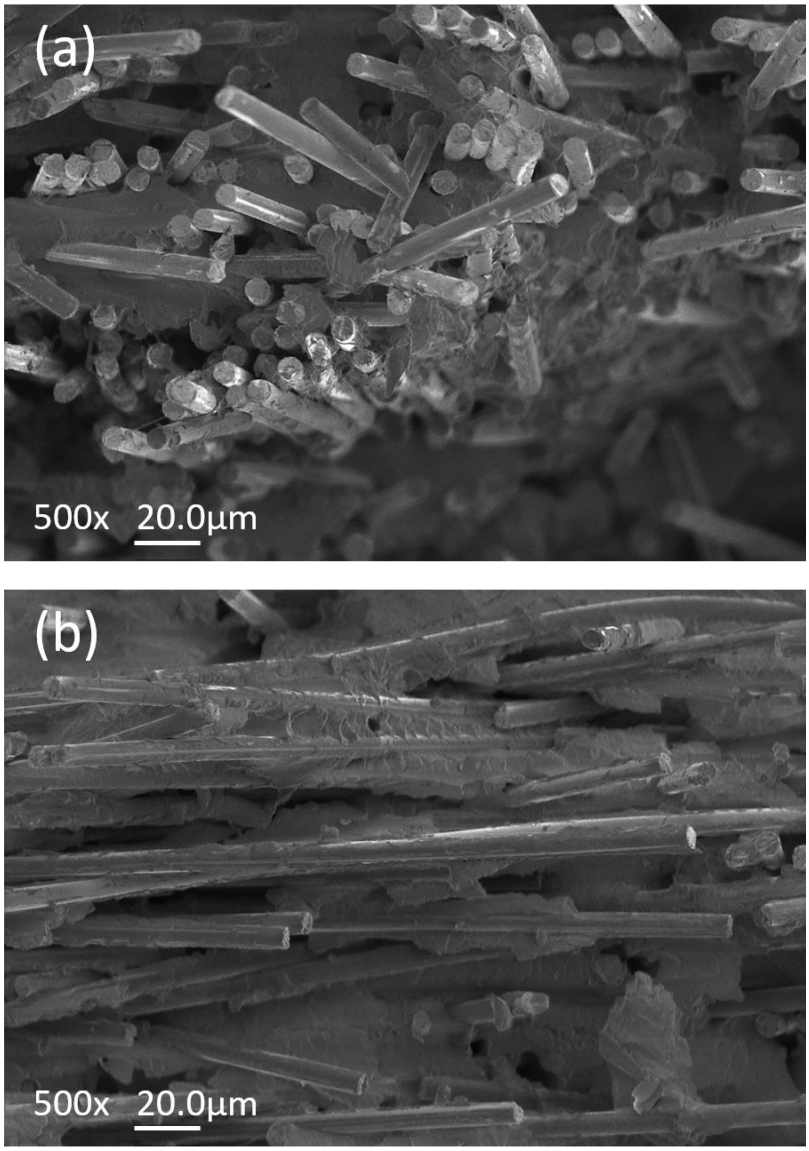

Figure 2-15 SEM images of the fracture surface of (a) S60-CWT-L and (b) S60-CWT-T after tensile testing

2.3.1.3. Flexural property

In a real situation, flexural failure is most often observed. With the aim of searching the upper limit of V_f and stretching ratio, the flexural properties of CWT21, CWT31, S30-CWT29, S60-CWT34, CWT37, S48-CWT43, and S68-CWT39 were measured by three-point bending test.

As shown in Figure 2-16, the flexural strength can reach 863 MPa, which is even higher than continuous woven CF fabric reinforced thermosetting plastic in Ma's study [141]. A similar tendency as in the tensile test result can be seen when V_f increases. However, in terms of stretching ratio, stretching ratio below 50% can be considered more favorable compared with higher stretching ratios as the flexural properties of S30-CWT29 and S48-CWT43 are dramatically higher than the control groups' and nearly close to that of high level stretched CWT, and in the case of V_f being approximately 40%, the flexural property of S68-CWT39 is even lower than that of S48-CWT43. This is due to the damage of web structure integration caused by excessive stretching, which means fiber aligning has reached its limit; some fibers withdrew and stopped moving forward when fibers lost connection with each other. This is clearly demonstrated in Figure 2-17, which shows images taken with an LED light panel below the sheets; fiber-rich and fiber-poor areas are clearly evident in S68-CWT39. In addition, residual stress was created inside the structure. It is apparent that S48-CWT43, which has both higher CF volume fraction and stretching ratio, was not able to overwhelm S30-CWT29, which was attributed to fiber saturation during carding process with high V_f. When the carding pins are overloaded, the fiber realignment degree tends to decrease.

In summary, S30-CWT29 had the optimal flexural properties among the various types of CWT.

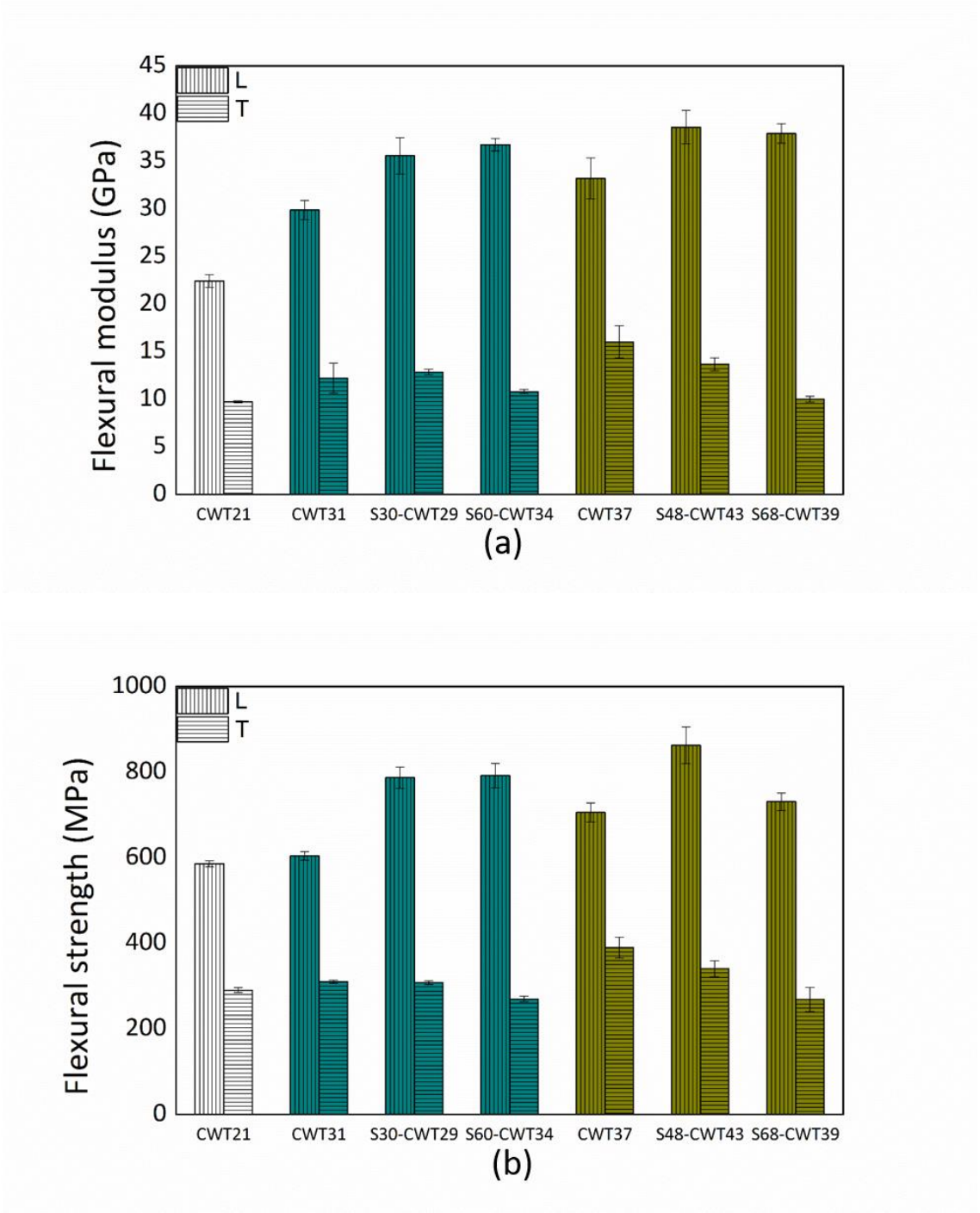

Figure 2-16 Results of three-point tests: (a) flexural modulus comparison and (b) flexural strength comparison among CWT with different CF volume fractions and stretching ratios

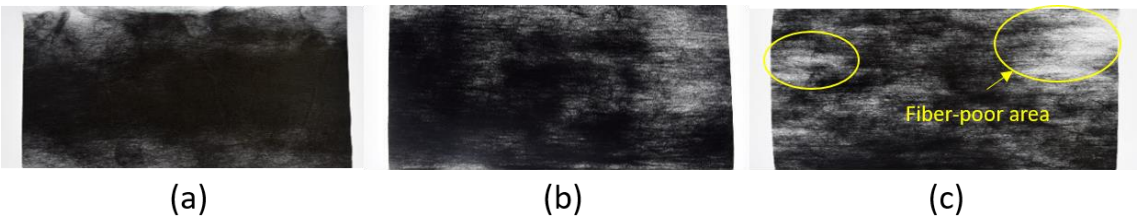

Figure 2-17 Sheet appearance of: (a) CWT37, (b) S48-CWT43, (c) S68-CWT39

2.3.1.4. Impact energy absorption

The static mechanical test results show that S30-CWT31 stands out from other types of CWT material. Therefore, Izod impact tests were also carried out to evaluate their dynamic property. The energy absorption was introduced as the evaluation index among CWT21, CWT31, and S30-CWT31, as shown in Figure 2-18. We supposed CWT21 might have better performance since high resin content would bring about more capacity for energy absorption, but they are almost equally matched in terms of energy absorption. Hence, it be can be concluded that fiber orientation may be a critical factor for both the static and dynamic properties of the CWTs.

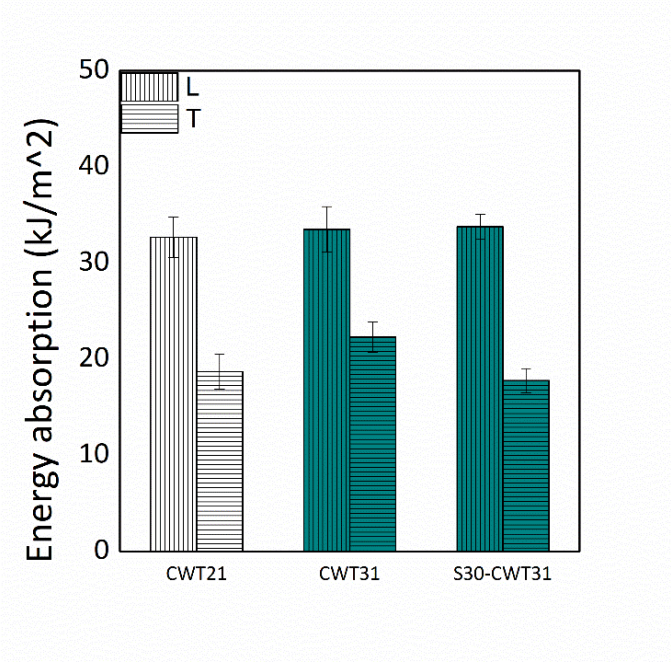

Figure 2-18 Energy absorption of CWT21, CWT31, and S30-CWT31 from Izod impact testing

2.3.1.5. Evaluation of fiber orientation distribution (FOD)

In order to obtain fiber orientation information, image binarization is an important step. The scanned images were transferred to TRI/3D-FBR-DT software (RATOC Corporation) to estimate microstructure orientation and anisotropy of the material based on the most widely used technique, the Mean Intercept Length (MIL) tensor [142]. Angles θ and φ represent in-plane and out-of-plane fiber orientation, as shown in Figure 2-19.

After image processing, the collected data of in-plane fiber orientation θ was analyzed by descriptive statistics into frequency counts ranging from -90° to 90° at 5° intervals, which is presented as a histogram in Figure 2-19. Note that 0° is also correlated to the axial direction in the tensile test and the machine direction in the carding process.

From the statistic results, it is apparent that the carding and stretching process did improve fiber alignment where most CFs were aligned within ± 15°. Furthermore, the fiber alignment degree of each material can be compared directly over the narrow scope of ±5°. The stretching ratio shows a nonlinear effect on the FOD, where it has around 25% improvement when stretching ratio is 30%, while there is just 11% improvement in the case of a stretching ratio of 60%. This can explain the decrease in mechanical properties when the stretching ratio is 60% and over.

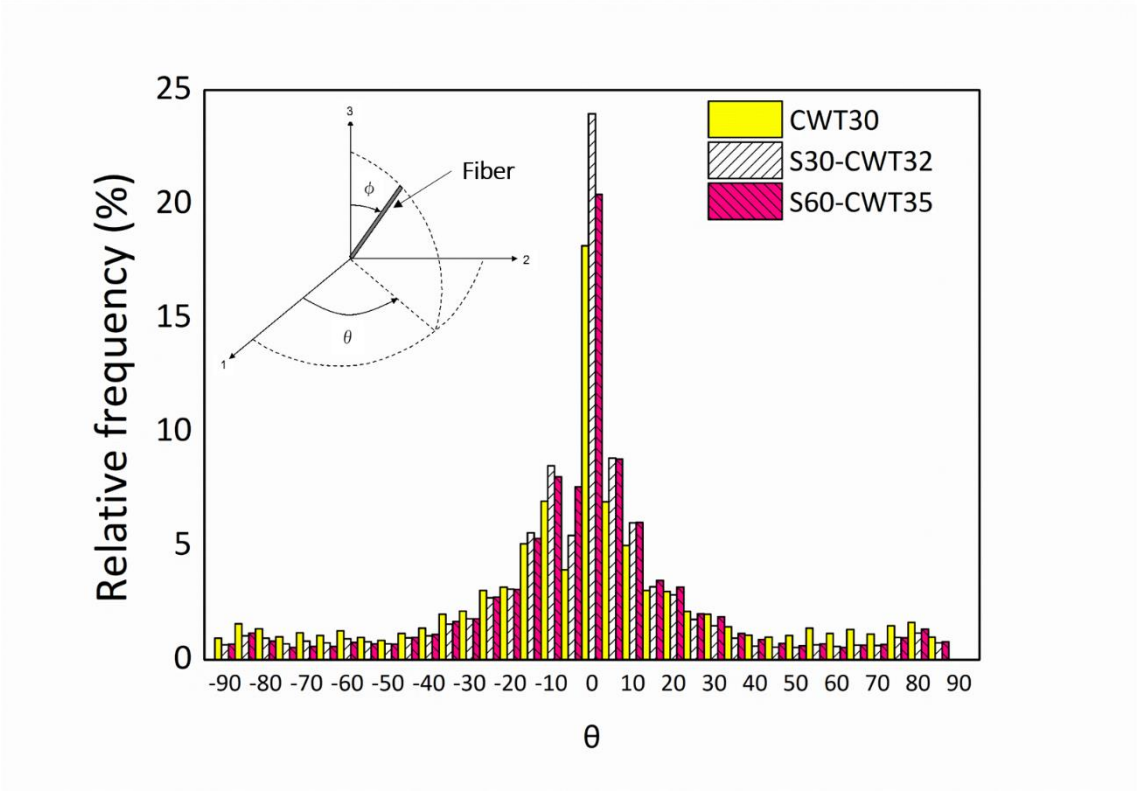

Figure 2-19 Fiber orientation distributions of CWT30, S30-CWT32, and S60-CWT35

2.3.2. Prediction of elastic moduli with FOD

2.3.2.1. Simulated laminate modeling

To model the laminate, the structure was treated as a set of unidirectional ply elements were are stacked according to the fiber orientation distribution as illustrated in Figure 2-20. Based on classic laminate theory [143], for the orthotropic lamina, the most general linear stress-strain relationship for three-dimensional state of stress will be reduced to a plane stress with five nonzero compliances in which only four are independent. The 123 coordinate axes are referred to as the principal material coordinates. The lamina stiffness matrix is denoted as

$$\mathbf{Q_{ij}} = \begin{bmatrix} Q_{11} & Q_{12} & 0 \\ Q_{12} & Q_{22} & 0 \\ 0 & 0 & Q_{66} \end{bmatrix} \qquad \text{Equation 2-1}$$

where

$$Q_{11}=\frac{E_1}{1-\nu_{12}\nu_{21}} \quad \text{Equation 2-2}$$

$$Q_{12}=\frac{\nu_{12}E_2}{1-\nu_{12}\nu_{21}}=Q_{21} \quad \text{Equation 2-3}$$

$$Q_{22}=\frac{E_2}{1-\nu_{12}\nu_{21}} \quad \text{Equation 2-4}$$

$$Q_{66}=G_{12} \quad \text{Equation 2-5}$$

The elastic moduli or engineering constants of unidirectional ply were calculated based on Hooke's law and the rule of mixture as

$$E_1 = E_f V_f + E_m(1 - V_f) \quad \text{Equation 2-6}$$

$$\frac{1}{E_2} = \frac{V_f}{E_f} + \frac{1 - V_f}{E_m} \quad \text{Equation 2-7}$$

$$\nu_{21} = \nu_f V_f + \nu_m(1 - V_f) \quad \text{Equation 2-8}$$

$$\nu_{12} = \frac{E_2}{E_1}\nu_{21} \quad \text{Equation 2-9}$$

$$G_{12} = \frac{G_m G_f}{G_m V_f + G_f(1 - V_f)} \quad \text{Equation 2-10}$$

where E_f and E_m are the longitudinal fiber modulus and matrix modulus, respectively; ν_f and ν_m are the Poisson's ratio of fiber and matrix, respectively; G_f and G_m are shear modulus of fiber and matrix, respectively; E_1 and E_2 are the longitudinal and transverse moduli of unidirectional lamina, respectively; ν_{21} and ν_{12} represent the secondary and principal Poisson's ratio of unidirectional laminate, respectively; and G_{12} is the major shear modulus of the unidirectional laminate.

However, the generally orthotropic lamina in off-axis coordinates is necessary to analyze laminates, and the relationships for transformation of stress components between coordinate axes can be obtained by the equations of static equilibrium. After carrying out the matrix

multiplications and converting back to engineering strains, the transformed stress-strain relationship is defined as

$$\{\boldsymbol{\sigma}\} = [\overline{\mathbf{Q}}]\{\boldsymbol{\varepsilon}\} \quad \text{Equation 2-11}$$

where $\{\boldsymbol{\sigma}\}$ is the stress, $\{\boldsymbol{\varepsilon}\}$ is the tensor strain, and $[\overline{\mathbf{Q}}]$ are the transformed lamina stiffness matrix, which describes the elastic behavior of in-plane loading.

$$\overline{\mathbf{Q}}_{\mathbf{ij}} = \begin{bmatrix} \overline{\mathrm{Q}}_{11} & \overline{\mathrm{Q}}_{12} & \overline{\mathrm{Q}}_{16} \\ \overline{\mathrm{Q}}_{12} & \overline{\mathrm{Q}}_{22} & \overline{\mathrm{Q}}_{26} \\ \overline{\mathrm{Q}}_{16} & \overline{\mathrm{Q}}_{26} & \overline{\mathrm{Q}}_{66} \end{bmatrix} \quad \text{Equation 2-12}$$

Where the $\overline{\mathrm{Q}}_{ij}$ are defined as follows:

$$\overline{\mathrm{Q}}_{11} = Q_{11}l^4 + Q_{22}m^4 + 2(Q_{12} + 2Q_{66})l^2m^2 \quad \text{Equation 2-13}$$

$$\overline{\mathrm{Q}}_{12} = (Q_{11} + Q_{22} - 4Q_{66})l^2m^2 + Q_{12}(l^4 + m^4) \quad \text{Equation 2-14}$$

$$\overline{\mathrm{Q}}_{22} = Q_{11}m^4 + Q_{22}l^4 + 2(Q_{12} + 2Q_{66})l^2m^2 \quad \text{Equation 2-15}$$

$$\overline{\mathrm{Q}}_{16} = (Q_{11} - Q_{12} - 2Q_{66})l^3m - (Q_{22} - Q_{12} - 2Q_{66})lm^3 \quad \text{Equation 2-16}$$

$$\overline{\mathrm{Q}}_{26} = (Q_{11} - Q_{12} - 2Q_{66})m^3l - (Q_{22} - Q_{12} - 2Q_{66})ml^3 \quad \text{Equation 2-17}$$

$$\overline{\mathrm{Q}}_{66} = (Q_{11} + Q_{22} - 2Q_{12} - 2Q_{66})l^2m^2 + Q_{66}(l^4 + m^4) \quad \text{Equation 2-18}$$

where the angle between the two axes is denoted by an angle θ ; $\mathrm{l} = \cos\theta$, $\mathrm{m} = \sin\theta$.

For a lamina that occupies the k^{th} position in the laminate with total n ply, Equation 2-11 can be written as

$$\{\boldsymbol{\sigma}\}^{\mathrm{k}} = [\overline{\mathbf{Q}}]^{\mathrm{k}}\{\boldsymbol{\varepsilon}\}^{\mathrm{k}} \quad \text{Equation 2-19}$$

Therefore, the laminate extensional stiffnesses are given by

$$A_{ij} = \sum_{k=1}^{n} \left(\overline{Q}_{ij}\right)^{k} t_k \qquad \text{Equation 2-20}$$

where t_k represents the thickness fraction of the k^{th} ply.

However, CWT material has a continuous fiber orientation distribution throughout the whole plate, so Equation 2-20 should be replaced with the corresponding integral:

$$A_{ij} = \frac{\int_{-\pi/2}^{\pi/2} \overline{Q}_{ij} f(\theta)\, d\theta}{\int_{-\pi/2}^{\pi/2} f(\theta)\, d\theta} \qquad \text{Equation 2-21}$$

where $f(\theta)$ is the density function, and θ is the angle of in-plane orientation. Here, the density function was replaced by actual measured FOD. Therefore,

$$\int_{-\pi/2}^{\pi/2} f(\theta)\, d\theta = 1 \qquad \text{Equation 2-22}$$

Alternatively, the loading can be expressed in terms of the strains as

$$\{\mathbf{N}\} = [\mathbf{a}]\{\boldsymbol{\varepsilon}\} \qquad \text{Equation 2-23}$$

where $\{\mathbf{N}\}$ represents the loading, and $[\mathbf{a}]$ is the matrix inverse $[\mathbf{A}]^{-1}$.

Therefore, the overall engineering moduli, E_{11} and E_{22}, along the 1-2 axes could be obtained from the following relations:

$$E_{11} = \frac{1}{a_{11}} \qquad \text{Equation 2-24}$$

$$E_{22} = \frac{1}{a_{22}} \qquad \text{Equation 2-25}$$

A flow chart of the simulated laminate modeling is shown in Figure 2-20.

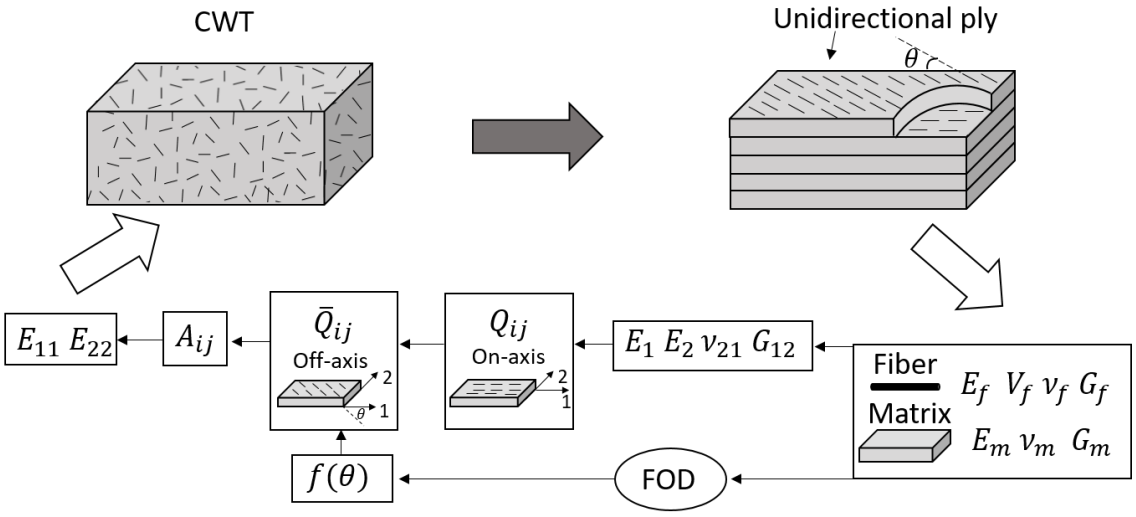

Figure 2-20 Simulated laminate plate model

2.3.2.2. Netting analysis

The procedure treats the laminate as a net and ignores the presence of the matrix and considers only the loading of the fiber ends. Meanwhile, the flexural stiffness of a single fiber is assumed to be negligible, so the fiber can only transfer tension loading. Since it is assumed that only fibers are loaded, according to Cox's model [32], if a planar mat of fibers is subjected to tensile strains e_1 and e_2 at two ends and to a shear strain ϕ, the strain of a fiber inclined at angle θ to the direction of e_1 is $e_1 \cos^2\theta + e_2 \sin^2\theta + \phi \cos\theta \sin\theta$; $f(\theta)$ is the distribution function which represent the number of fibers at angle θ and it was taken as $\int_{-\pi/2}^{\pi/2} f(\theta)\, d\theta = 1$; the loads P_1 in the direction of e_1 on the edge perpendicular to e_1, P_2 in the direction of e_2 on the edge perpendicular to e_2, Q in the direction of e_1 on the edge perpendicular to e_2 or vice versa will be defined as

$$P_1 = K \int_{-\pi/2}^{\pi/2} e_1 \cos^2\theta + e_2 \sin^2\theta + \phi \cos\theta \sin\theta) \cos^2\theta\, f(\theta) d\theta \qquad \text{Equation 2-26}$$

$$P_2 = K \int_{-\pi/2}^{\pi/2} e_1 \cos^2\theta + e_2 \sin^2\theta + \phi \cos\theta \sin\theta) \sin^2\theta\, f(\theta) d\theta \qquad \text{Equation 2-27}$$

$$Q = K \int_{-\pi/2}^{\pi/2} e_1 \cos^2\theta + e_2 \sin^2\theta + \phi \cos\theta \sin\theta) \cos\theta \sin\theta\, f(\theta) d\theta \qquad \text{Equation 2-28}$$

where K is the product of fiber modulus and fiber density. Then

$$P_1 = c_{11}e_1 + c_{12}e_2 + c_{16}\phi \quad \text{Equation 2-29}$$

$$P_2 = c_{12}e_1 + c_{22}e_2 + c_{26}\phi \quad \text{Equation 2-30}$$

$$Q = c_{16}e_1 + c_{26}e_2 + c_{66}\phi \quad \text{Equation 2-31}$$

Where

$$c_{11} = K\int_{-\pi/2}^{\pi/2} \cos^4\theta \ f(\theta)d\theta \quad \text{Equation 2-32}$$

$$c_{22} = K\int_{-\pi/2}^{\pi/2} \sin^4\theta \ f(\theta)d\theta \quad \text{Equation 2-33}$$

$$c_{16} = K\int_{-\pi/2}^{\pi/2} \cos^3\theta \ \sin\theta f(\theta)d\theta \quad \text{Equation 2-34}$$

$$c_{26} = K\int_{-\pi/2}^{\pi/2} \cos\theta \sin^3\theta \ f(\theta)d\theta \quad \text{Equation 2-35}$$

$$c_{12} = K\int_{-\pi/2}^{\pi/2} \cos^2\theta \sin^2\theta \ f(\theta)d\theta \quad \text{Equation 2-36}$$

Therefore, the lamina stiffness matrix of the transformed stress-strain relationship can be written as

$$\bar{Q}_{ij}{}' = \begin{bmatrix} l^4 & l^2m^2 & l^3m \\ l^2m^2 & m^4 & lm^3 \\ l^3m & lm^3 & l^2m^2 \end{bmatrix} \quad \text{Equation 2-37}$$

Therefore, the laminate extensional stiffnesses are given by

$$A_{ij}{}' = \frac{\int_{-\pi/2}^{\pi/2} \bar{Q}_{ij}{}' f(\theta)\, d\theta}{\int_{-\pi/2}^{\pi/2} f(\theta)\, d\theta} \quad \text{Equation 2-38}$$

And the overall engineering moduli $E_{11}{}'$ and $E_{22}{}'$ are obtained from the computed $A_{ij}{}'$ matrix as

$$E_{11}{}' = \frac{A_{11}{}'A_{22}{}' - A_{12}{}'^2}{A_{22}{}'} \quad \text{Equation 2-39}$$

$$E_{22}{}' = \frac{A_{11}{}'A_{22}{}' - A_{12}{}'^2}{A_{11}{}'} \qquad \text{Equation 2-40}$$

2.3.2.3. Comparison

Figure 2-21 shows a comparison between the experimental results and simulated modelling results. Although there is a gap between the prediction and the experiment, this is due to using unidirectional continuous fiber ply as components, and both laminate and netting theories show good correlation with experimental results. The result of short random-orientated carbon fiber paper reinforced thermoplastics with a V_f of 30% (CPT30) was used for comparison. In the case of CPT30 and S60-CWT35, there are relatively large deviations between prediction and the experiment. The former case is due to extremely short fiber length, for which the predicted unidirectional fiber ply is not suitable, while in the latter case, excessive stretching ratio caused integration out of balance and created residual stress inside the structure.

Although the moduli predicted using netting theory are smaller to those using laminate theory due to ignoring the contribution of the matrix, this has intuitive appeal and is acceptable within tolerance because it has a simple procedure and good agreement with experimental results. It can be used as a simple tool for approximating CWT material.

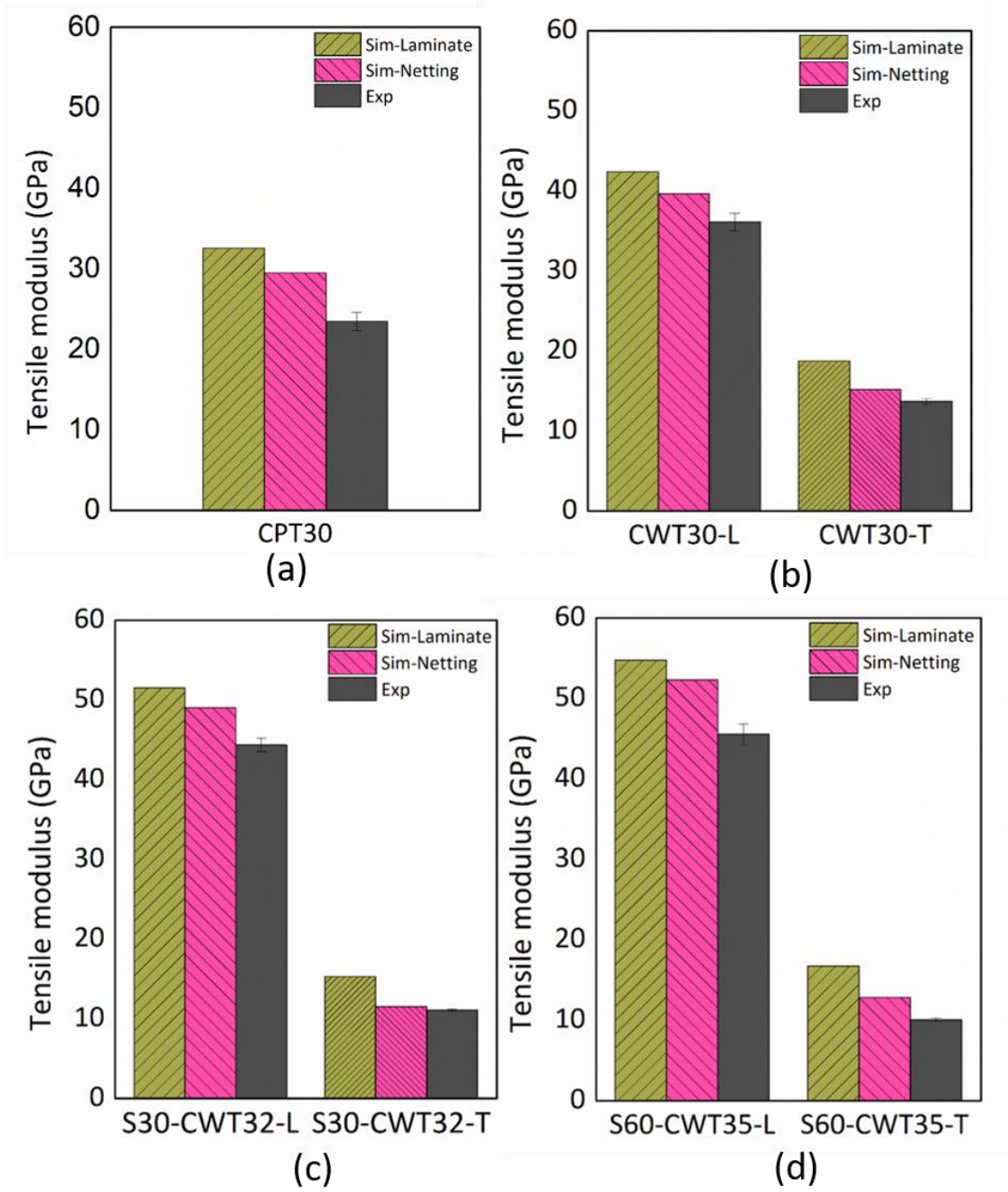

Figure 2-21 Simulated (Sim) and measured (Exp) tensile moduli: (a) CPT30, (b) CWT30, (c) S30-CWT32, and (d) S60-CWT35

2.4. Summary

In this chapter, through the development of a carding and stretching method to obtain a promising fiber alignment for rCF, the following conclusions can be drawn.

The carding process was used as the primary step to arrange thoroughly opened rCF and mix them with resin fibers uniformly. The stretching process was applied as a supplement to realign rCF. Using this method, CWT with a V_f of 43% without harmful void can be achieved. Satisfactory mechanical properties were obtained in some stretched types of CWT, and their tensile properties are close to those of unidirectional CF tape reinforced thermoplastics, and the flexural strength of some stretched CWT can be even higher than that of continuous woven CF fabric reinforced thermosetting plastic. An optimal CWT with a V_f of 30% and stretching ratio of 30% was proved. After X-ray micro-CT scanning, using an image processing and statistical analysis method, fiber alignment level was observed through FOD, and it was found that most rCF were aligned within ± 15°. At the end, two analytical models were applied to predict elastic moduli. Both laminate and netting theories show good correlation with experimental results, and netting theory was proven to be a simple tool for approximating CWT material.

3. Brittle fracture of short rCF reinforced thermoplastic and its improvement

3.1. Introduction

In this chapter, discontinuous AP was used as the toughening component to hybridize discontinuous CPT sheet. Effect of stacking sequence and aramid fiber length were investigated through various loadings and compared.

.

3.2. Effect of stacking sequence

In this section, aramid fiber paper was used to toughen CPT.

The stacking sequence has strong influence on mechanical performance of hybrid. To study the influence of stacking sequence, the volume fraction of the individual reinforcements were kept constant and only fiber packing of different fiber layers was changed from intimate to discrete state by varying stacking sequence.

Based on literature review, many researchers believed the impact resistance can be improved by placing low elongation fiber layers inside the hybrid and high elongation layers outside as shield. In order to verify whether our hybrids also conform the trend, carbon fiber layer on the outside or opposite positioning were also studied.

Different hybrids were investigated through flexural and energy absorption behavior.

3.2.1. Materials and methods

3.2.1.1. Materials

A kind of CPT (Awa Paper Co. Ltd.) sheet that composed of polyamide 6 (PA6) fibers and 6-mm-long carbon fibers (CPT-PA6 sheet) was used. It was prepared using a paper-making process where short resin fibers and carbon fibers were mixed thoroughly in water; then, the suspension was post-processed using hot compression into paper-like substrates. The carbon fiber volume fraction is 20%.

DuPont™ Nomex® paper Type 410 of aramid fiber paper was provided by DuPont Teijin Advanced Papers (Japan) Ltd. The paper was designed to be more porous and compatible to PA6 to achieve better resin impregnation and adhesion with dissimilar layer.

In order to achieve constant volume fraction of both two kinds of fiber components, the amount of individual reinforcement and PA6 films for resin supplement were calculated and prepared based on the classic rule of mixture.

3.2.1.2. Molding

Before molding, carbon papers and aramid papers were stacked by several sequences designed as Figure 3-1 shows. Generally there are two main classification. One is “Aramid outside” (A) where aramid papers were set close to surface of laminate while the other one is “Carbon outside” (C) where carbon papers were set close to surface of laminate. And the stacking sequence of the hybrid laminates were decided by changing the fiber packing from a segregated to an intimate arrangement.

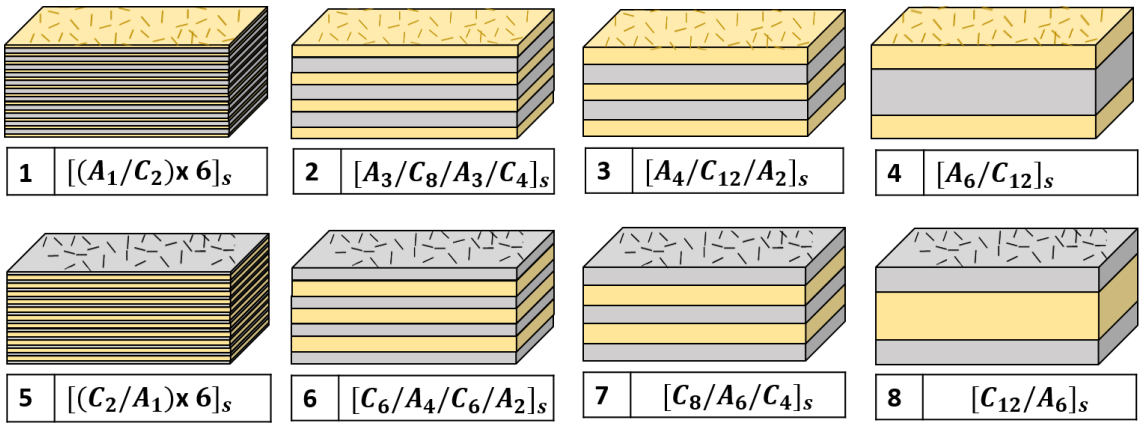

Figure 3-1 Stacking sequence

And the molding condition is shown as Figure 3-2.

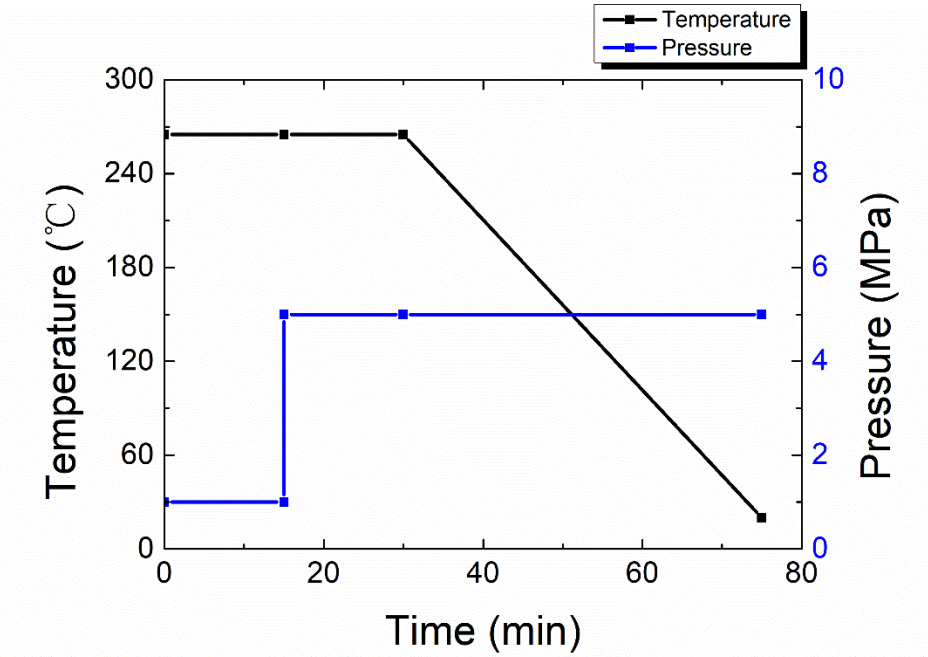

Figure 3-2 Molding condition of hybrid laminates

3.2.1.3. Experiment

3.2.1.3.1. Three-point bending test

Static three-point bending test of the hybrid beams were performed in accordance with the ASTM D 790-03 standard. The support span-to-depth ratio of 16:1 was chosen and the load was applied

at the middle of the span through a table-top precision universal tester from Shimadzu Corporation. The schematic of the set-up for the three-point test is shown as Figure 3-3.

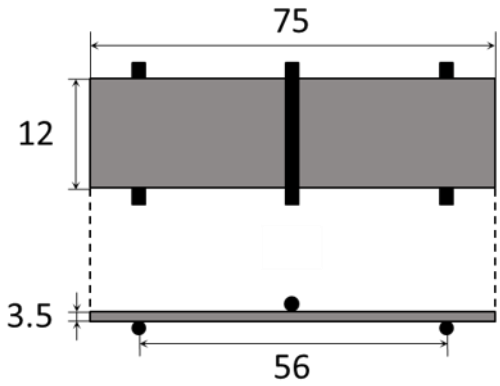

Figure 3-3 Schematic of the set-up for the three-point test

3.2.1.3.2. Izod impact test

Izod test was carried out by Instrumented pendulum impact tester (Instron USA, POE 2000e) following the testing standard of K7110 from JIS. The impact speed was approximately 1.5 m/s. The schematic of the set-up for the izod impact test is shown as Figure 3-4.

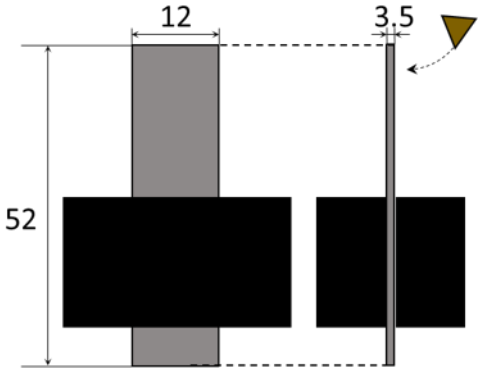

Figure 3-4 Schematic of the set-up for the izod impact

3.2.1.3.3. Three point impact test

Three-point impact test was conducted by HITS-P10 high-speed puncture impact tester from Shimazu Corporation. The test was carried out based on the standard JIS K7084. The impact speed was approximately 3.8 m/s. The schematic of the set-up for the three point impact test is shown as Figure 3-5.

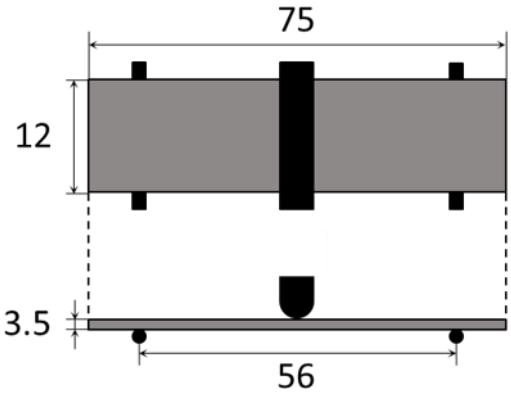

Figure 3-5 Schematic of the set-up for the three point impact test

3.2.2. Results and discussion

3.2.2.1. Molding quality

As we know that the coefficient of thermal expansion of aramid fiber is smaller than that of carbon fiber, which will result in residual tensile strains in the carbon fibers. Therefore, the molding quality or inner state of the hybrid panels were observed by optical microscope as shown in Figure 3-6, where it can be seen that the interface is adequate between two types of reinforcing fibers because there is no obvious defects or voids observed.

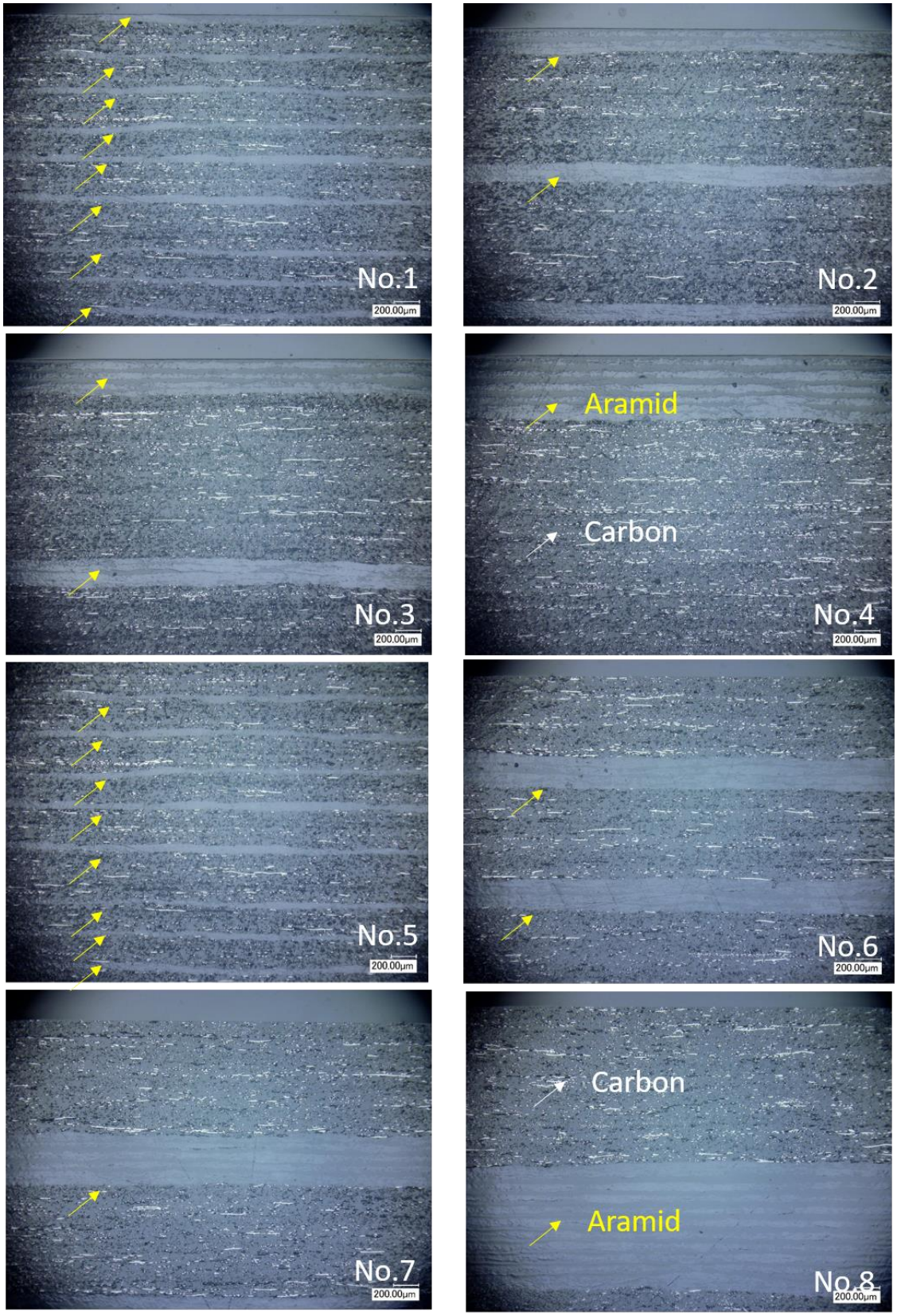
No.1
200.00μm
No.2
200.00μm
No.3
200.00μm
Aramid
Carbon
No.4
200.00μm
No.5
200.00μm
No.6
200.00μm
No.7
200.00μm
Carbon
Aramid
No.8
200.00μm

(a)

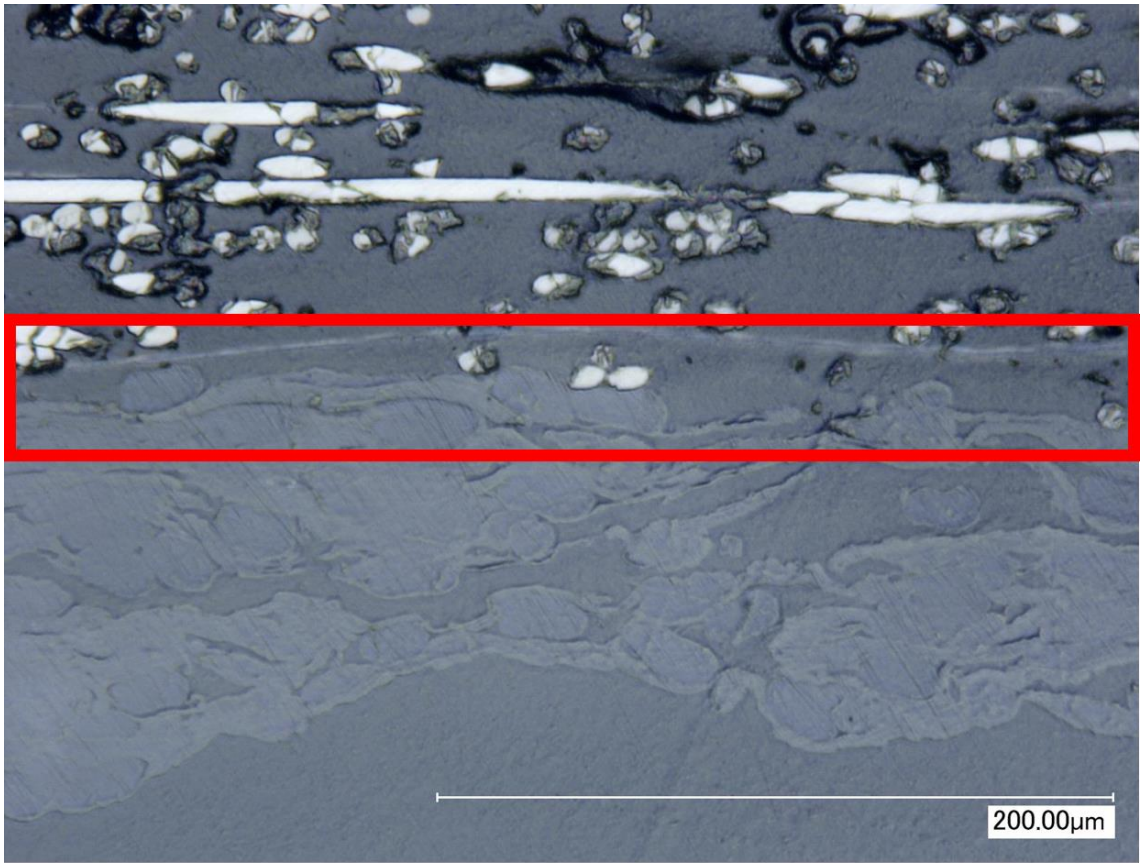

(b)

Figure 3-6 Optical observation for molding quality of the hybrids: (a) side-view of hybrids with different stacking sequence; (b) close-up of interface between carbon layer and aramid layer in hybrids

3.2.2.2. The result of three-point bending test

From stress-strain curves of three point bending test as shown in Figure 3-7, we can see that after hybridization, the flexural property tend to spread between pure CPT and pure APT. With more aramid papers placed outwardly, flexural property tend to decrease while the apparent failure strain extended. But it still shows the brittle feature in aramid outside case.

When it comes to carbon outside case, aramid layers take effect and can bear more stress when the aramid paper layer is thicker. For example, with thicker aramid layer in No.6 and No.7, it can

sustain more stress in later failure stage where No.7 shows three-step failure. But in the sandwich case of No.8 where the aramid layer is thickest, it still shows brittle. It is because all the carbon papers were on outside and sustain compression and tension, the core aramid papers concentrated on neutral plane and were not able to work resistance before the whole beam fails.

Therefore, No. 7 is an optimal stacking sequence if considering the final failure strain.

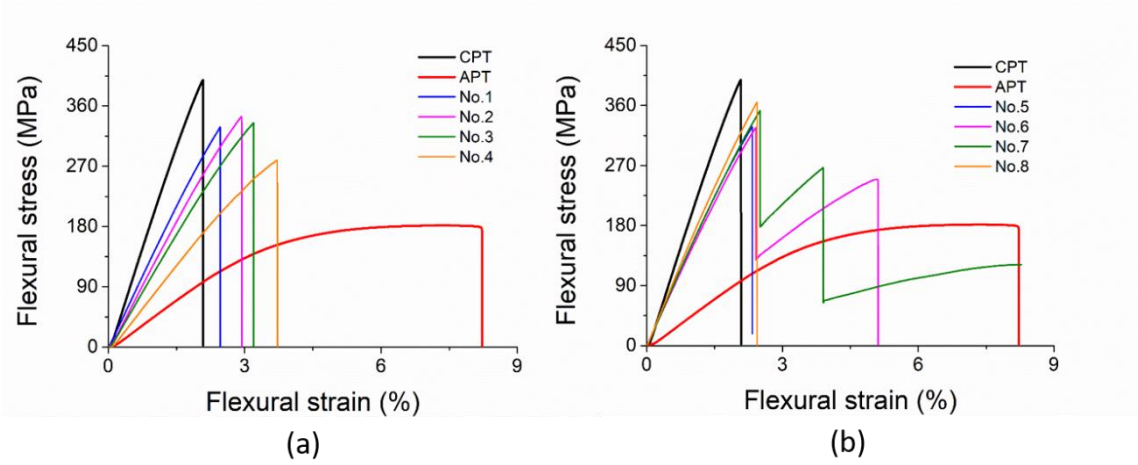

Figure 3-7 Flexural stress-strain curves of the hybrids: (a) No.1-No.4 (b) No.5-No.8

When comparing the flexural property as Figure 3-8 shows, with more aramid paper in outside, both flexural strength and flexural modulus decrease while it shows opposite in the case of carbon paper outside.

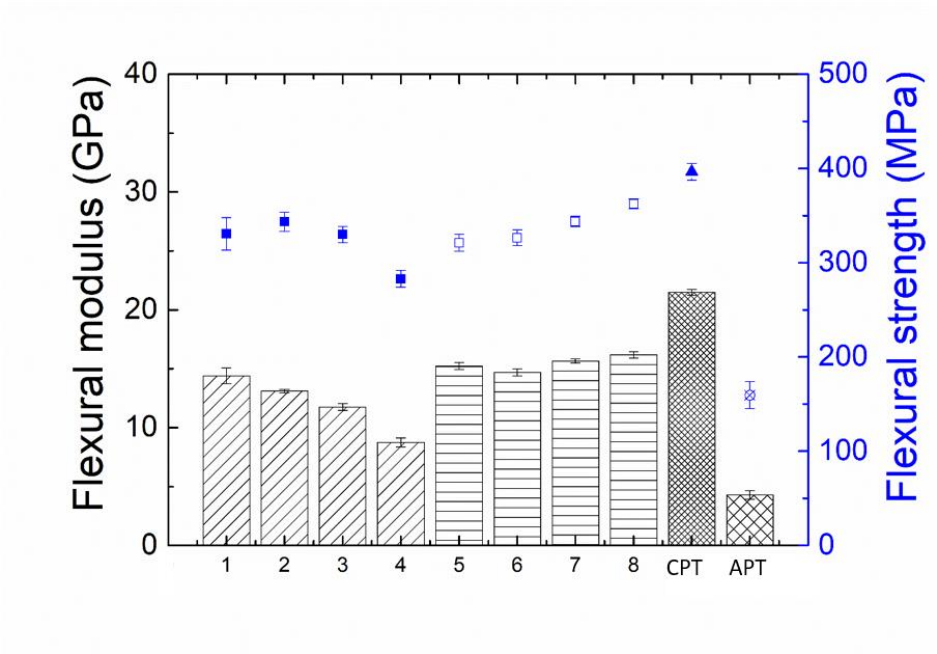

Figure 3-8 Flexural modulus and flexural strength of the hybrids

3.2.2.3. The result of izod impact test

Figure 3-9 shows the izod energy absorption results of the hybrid laminates. It was assumed that the aramid paper placed in outside layers panel is capable of absorbing more energy since carbon fibers are brittle and aramid fiber can sustain longer strain. But the result indicates it just depends on the number of segments which were separated by stacking sequence. For example, in No,4 and No.8, they are both sandwich structure, they both have 3 segments, but outside layer setting didn't influence energy absorption.

In addition, the positive hybrid effect can be observed during experiment in hybrids which didn't have catastrophic failure thanks to aramid fiber layer, which plays as a role of crack arrester and slow the development of the crack. CPT was too brittle that the sample separates apart in a short time, which actually shows risk to use this kind of material because it may cause secondary damage to neighbor.

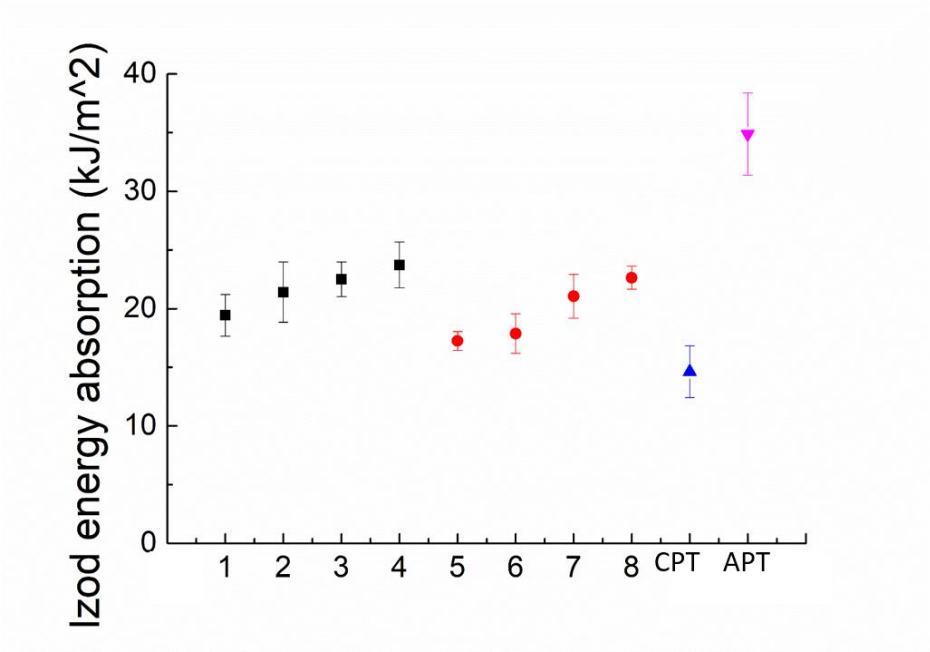

Figure 3-9 Izod impact energy absorption of the hybrids

3.2.2.4. The result of three-point impact test

Figure 3-10 shows the three-point impact energy absorption results of the hybrid laminates. It shows the same tendency as izod impact test, the more carbon paper placed outside, the higher energy absorption capacity can be obtained, which can also be seem from the displacement-load curves (Figure 3-11), that carbon paper contributed to the elastic impact region while the aramid fiber portion determined the curve extension and meanwhile.

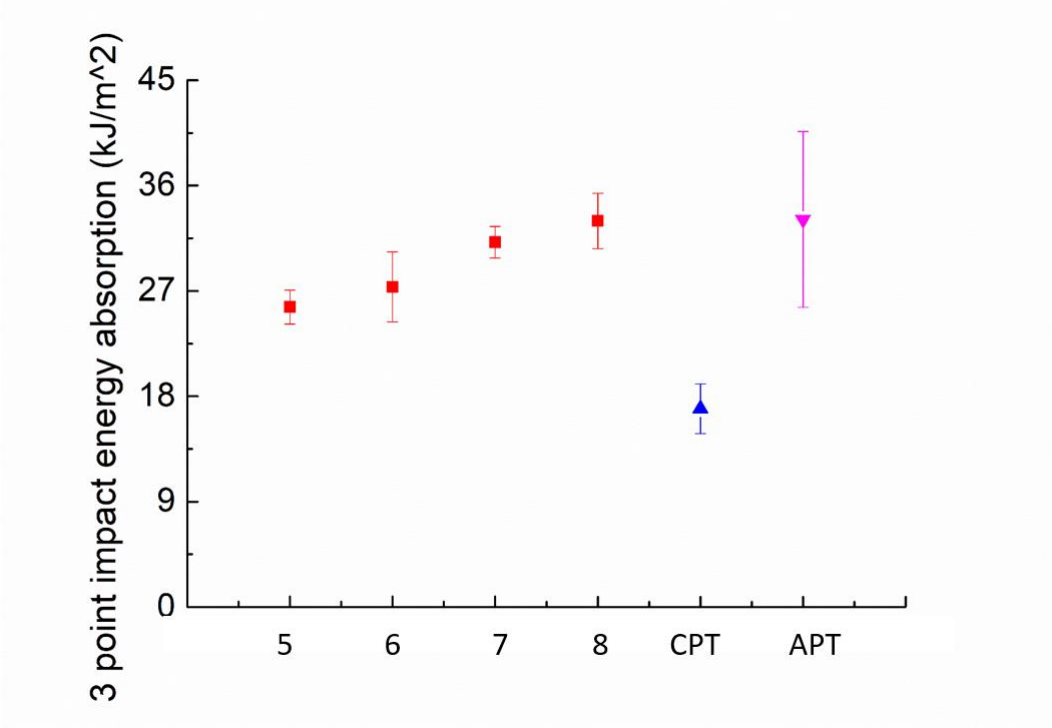

Figure 3-10 Three-point impact energy absorption of the hybrids

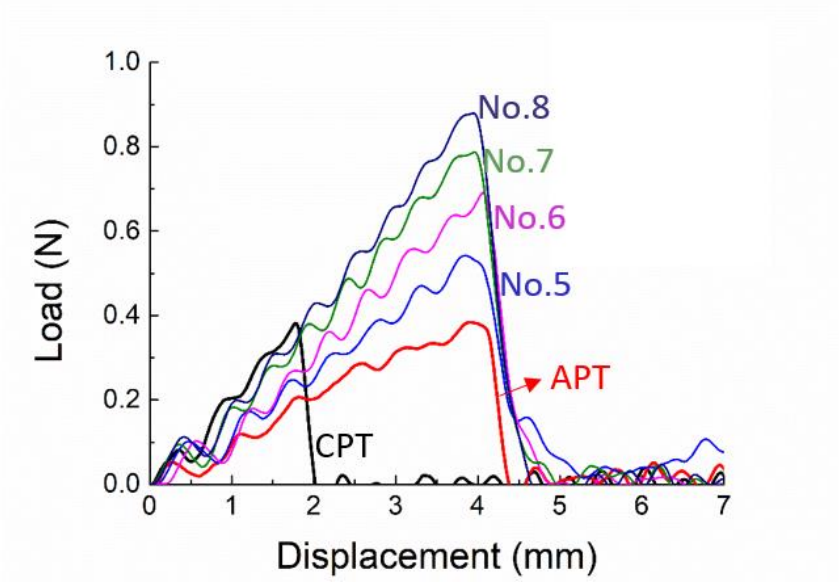

Figure 3-11 Load-displacement curves of the C type hybrids

3.2.3. Conclusion

In this study, discontinuous aramid fiber papers were applied to hybridize with discontinuous carbon fiber papers and reinforce with thermoplastic. Flexural and energy absorption behavior were investigated among the hybrid panels with various interlayer stacking sequence.

To sum up, hybridized carbon fiber/aramid fiber reinforced thermoplastics have positive hybrid effect where the toughness was improved. And No. 7 stacking sequence in type “carbon outside” is considered to be an optimal structure among all of the hybridization in this study.

3.3. Effect of aramid fiber length

In this section, the handmade aramid fiber paper with different fiber lengths were manufactured by paper-making process. And it was applied to interlaminated hybrid with the optimal stacking sequence from the last section. Intermingled CF/AF paper sheet was also produced to make intermingled hybrid to compare with interlaminated hybrid. And mechanical performance was studied among the hybrid panels with flexure and impact loadings.

3.3.1. Materials and methods

3.3.1.1. Materials

Technora® chopped aramid fibers with three different fiber length, 3 mm, 6 mm and 12 mm, were used. 6-mm long PA6 fibers were mixed with AF or CF using paper-making technique to produce both aramid paper (AP) and CF/AF paper as shown in Figure 3-12. The detail is addressed in the following part.

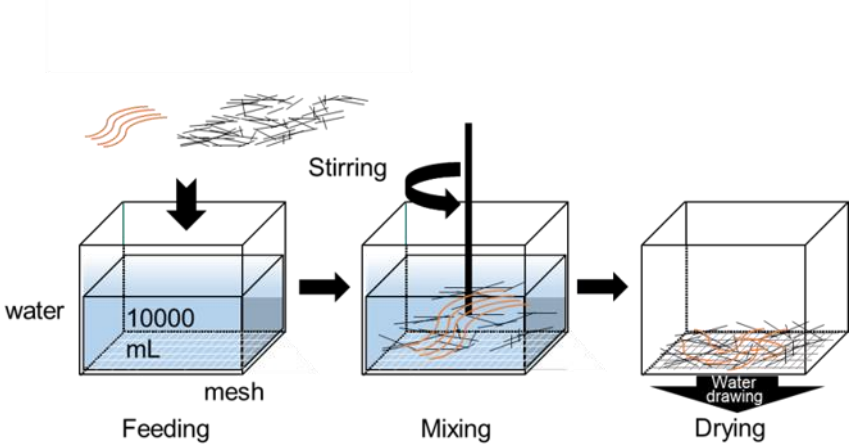

Figure 3-12 Schematic of AP and CF/AF paper preparation: a prototype of the papermaking process [144]

CPT-PA6 sheet described in the last section was used in making interlaminated hybrids.

In order to achieve constant volume fraction of both two kinds of fiber components, the amount of individual reinforcement and PA6 resin supplement were calculated and prepared based on the classic rule of mixture.

3.3.1.2. Manufacturing process of AP and CF/AF paper

The process is shown as following:

Weigh the desired amount of aramid fiber and small amount of PA6 fiber, whose function is to unite aramid fibers together after hot press, so as to make it easy to store the intermediate aramid sheet.

(1) Put two kinds of fibers into mixer with appropriate amount of dispersion agent and switch the mixer on for a few seconds.

(2) Pour the mixture into a big bucket with stirring machine on for around 30 seconds until the mixture is uniformly dispersed.

(3) Pour the mixture into a square shaped container named “Jabu Jabu-kun” with dense net at the bottom of it. Stir the mixture several times and drain the water, hopefully the uniformly dispersed aramid sheet could be obtained.

(4) Dry the sheet with Heating and cooling hand press (YSR-10H/C, SINTO Metal Industries Corporation) with 110 ℃ to evaporate the water.
(5) Melt the resin in the sheet so as to fix fibers together as a sheet after cooling down by using heating and cooling hand press machine with 240 ℃, which is higher than the melting point of polyamide-6, for 1 minute with pressure.
(6) Finally, trim the sheet into the desired size.

The processing of the AP and CF/AF paper is shown as Figure 3-13.

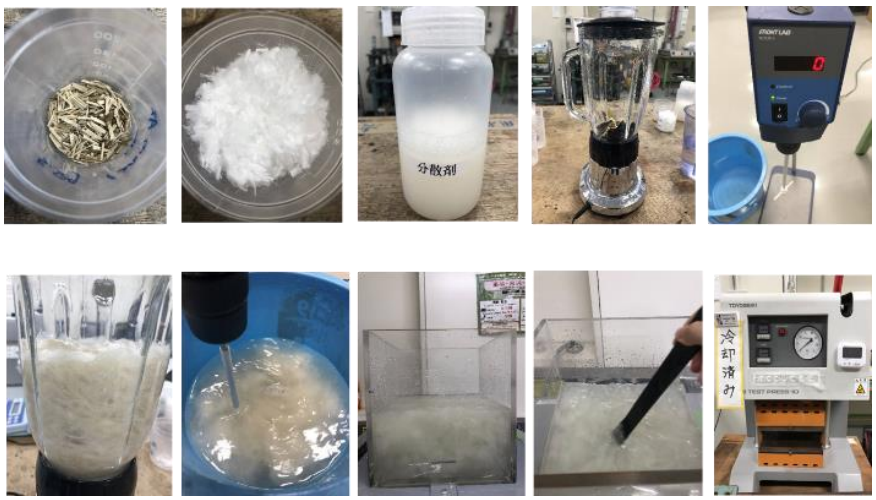

Figure 3-13 Manufacturing process of the AP and CF/AF paper

3.3.1.3. Molding

Before molding, carbon papers and aramid papers were stacked by carbon /aramid/ carbon/ aramid/ carbon sequence, which is chosen based on previous study.
When all papers were stacked with the sequence, they are placed onto the mold to manufacture hybrid panels by the molding condition shown in Figure 3-14.

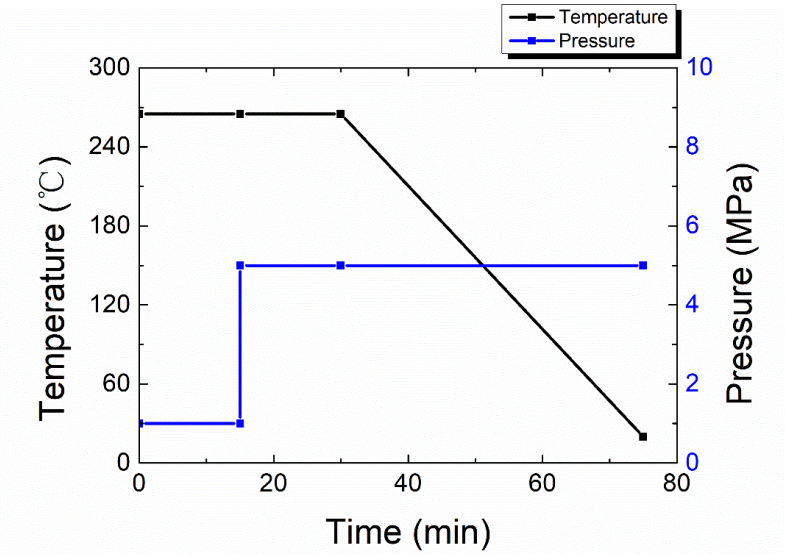

Figure 3-14 Molding condition of hybrids

The pure CPT and pure aramid fiber paper reinforce thermoplastics (APT) were also made and tested as control. The detail information of both interlaminated and intermingled hybrids is shown in Table 3-1.

Table 3-1 Detail information of the hybrids

Name	Material	Hybrid method	Length of aramid fiber[mm]	Length of carbon fiber[mm]
LH3	CPT/APT sheet	Interlaminated	3	6
LH6			6	
LH12			12	
MH6	CF/AF sheet	Intermingled	6	

3.3.1.4. Experiment

3.3.1.4.1. Three-point bending test

Static three-point bending test of the hybrid beams were performed in accordance with the ASTM D 790-03 standard. The support span-to-depth ratio of 16:1 was chosen and the load was applied

at the middle of the span through a table-top precision universal tester from Shimadzu Corporation. The schematic of the set-up for the three-point test is shown as Figure 3-15.

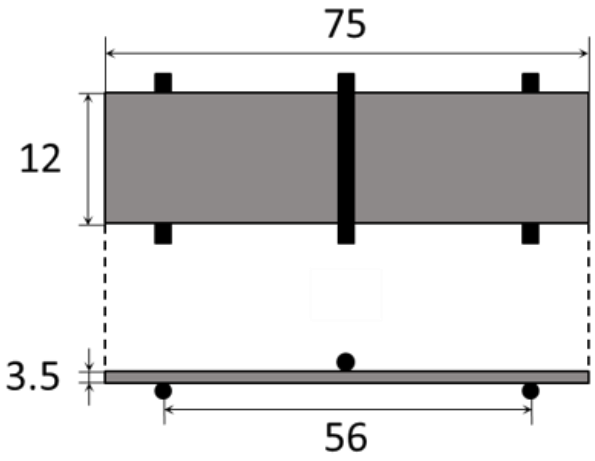

Figure 3-15 Schematic of the set-up for the three-point test

3.3.1.4.2. Izod impact test

Izod test was carried out by Instrumented pendulum impact tester (Instron USA, POE 2000e) following the testing standard of K7110 from JIS. The dimension is 52 mm in length and 12 mm in width. The impact speed was approximately 1.5 m/s. The schematic of the set-up for the izod impact test is shown as Figure 3-16.

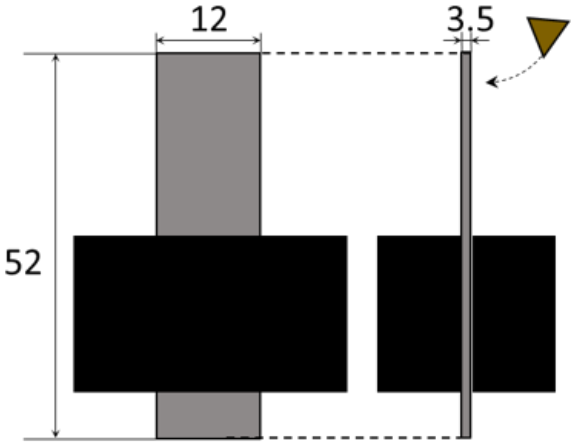

Figure 3-16 Schematic of the set-up for the izod impact

3.3.1.4.3. Three point impact test

Three-point impact test was conducted by HITS-P10 high-speed puncture impact tester from Shimazu Corporation. The test was carried out based on the standard JIS K7084. The impact speed was approximately 3.8 m/s. The schematic of the set-up for the three point impact test is shown as Figure 3-17.

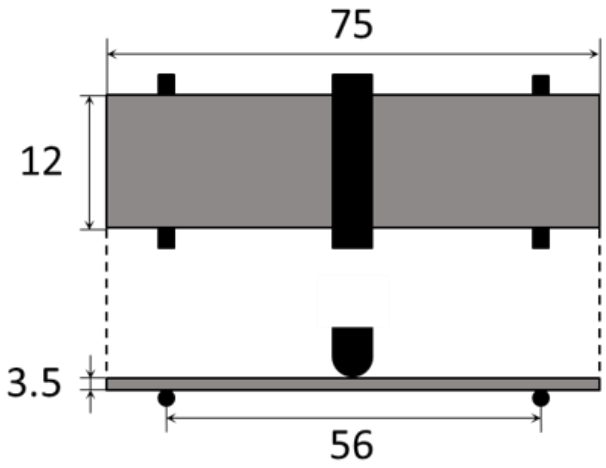

Figure 3-17 Schematic of the set-up for the three point impact test

3.3.2. Results and discussion

3.3.2.1. Molding quality

It can be seen that the interface is adequate between two types of reinforcing fibers since there is no obvious defects or voids observed as shown in Figure 3-18.

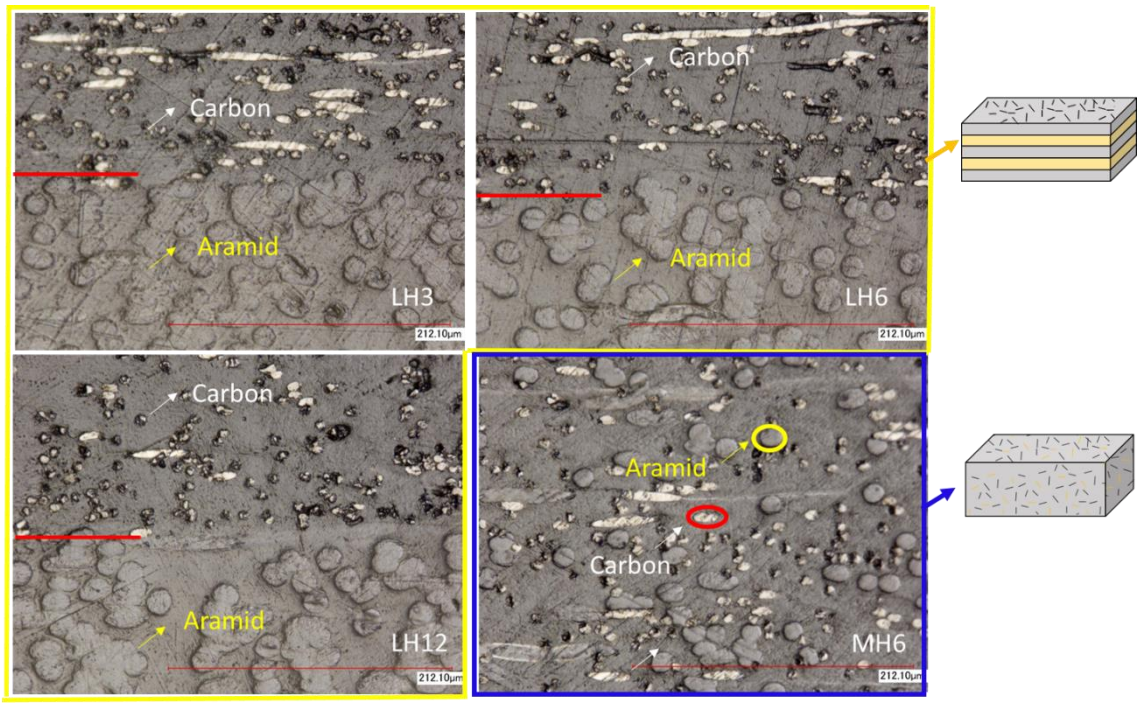

Figure 3-18 Molding quality of two types of hybrids

3.3.2.2. The result of three-point bending test

Figure 3-19 shows the flexural property of all types of beams under three point loading. In general, the flexural properties of both kinds of hybrids represent in-between two pure composites, which obeys the rule of mixture. In interlaminated hybrid, hybrid with 3mm and 6mm hybrid show similar flexural property while the one with 12mm aramid fiber has slight improvement, but just around 5%, in flexural property compared with the other two types. Therefore, it is considered that the fiber length did not contribute to flexural loading.

In the case of intermingled hybrid, the flexural strength is at the same level to interlaminated hybrid while the flexural modus shows lower value, which is because in interlaminated hybrid, carbon layer were put outside, thus it will be more stiff than intermingled hybrid

And from the flexural stress-strain curves in Figure 3-20, the general failure strain of intermingled hybrid did increase but it still show brittle characteristic, which is unwanted. And the general failure strain of interlaminated hybrid shows almost double since the interlaminated hybrid displays stage-like failure mode as shown in Figure 3-21. The first stress drop occurred

with the bottom carbon layer failure. After that aramid layer took effect and stopped crack propagation, which was then followed by the second stress drop where the first aramid layer and the second carbon layer failed spontaneously. Final failure occurred in the rest part. It can be concluded that with this kind of layer distribution, aramid fiber can act as a role of crack arrester. The general failure strain would be extremely extended and the whole material will not be brittle, which can be proved from fracture observation as shown in Figure 3-22, in the case of interlaminated hybrid, the upper carbon fiber layer even shows wrinkle shape which is not brittle fracture.

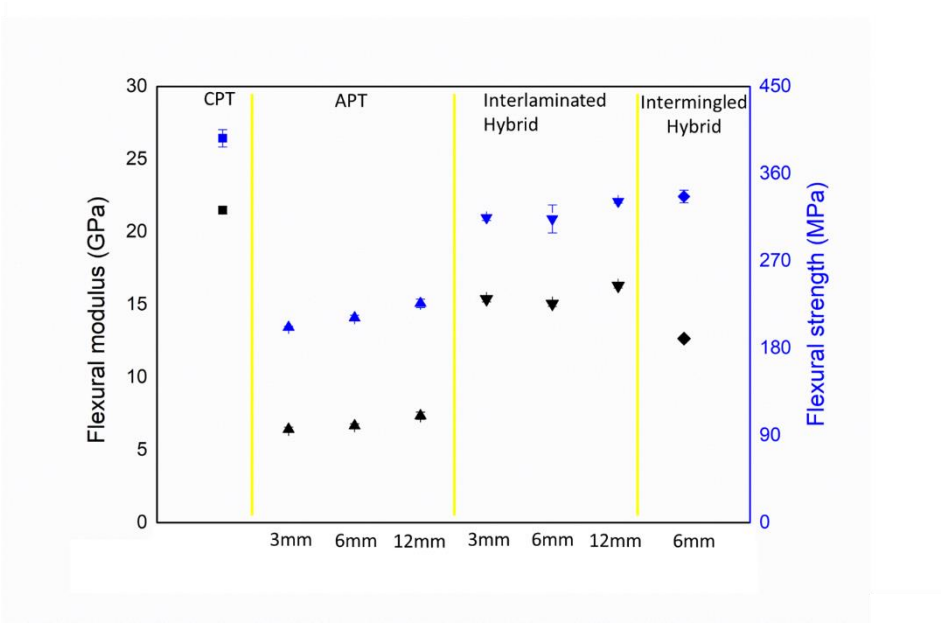

Figure 3-19 Flexural modulus and flexural strength of the hybrids and the controls

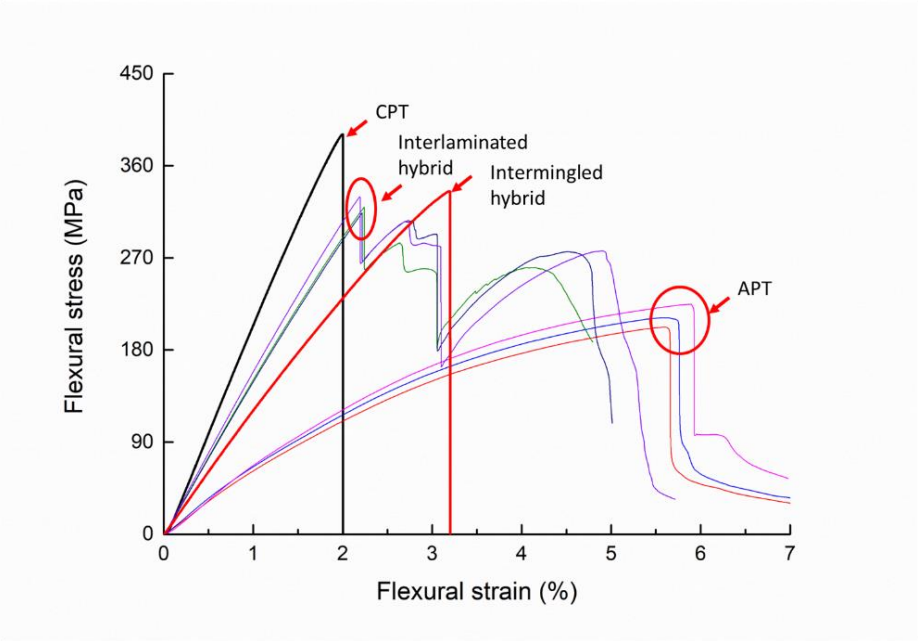

Figure 3-20 Flexural stress-strain curves of the hybrids and the controls

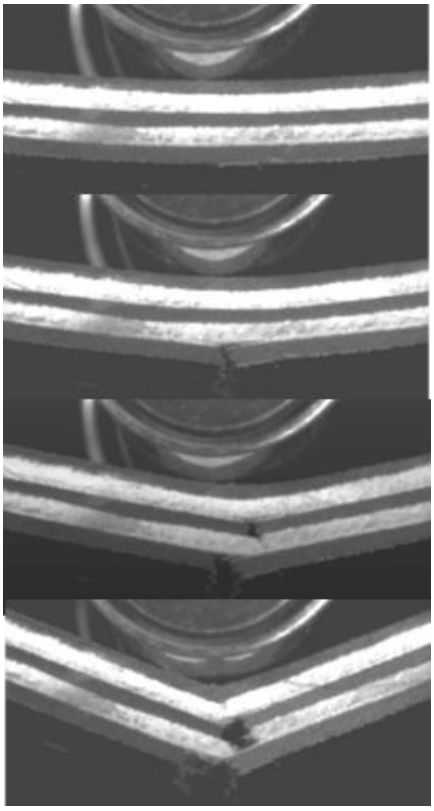

Figure 3-21 The failure mode of interlaminated hybrids in three-point bending test

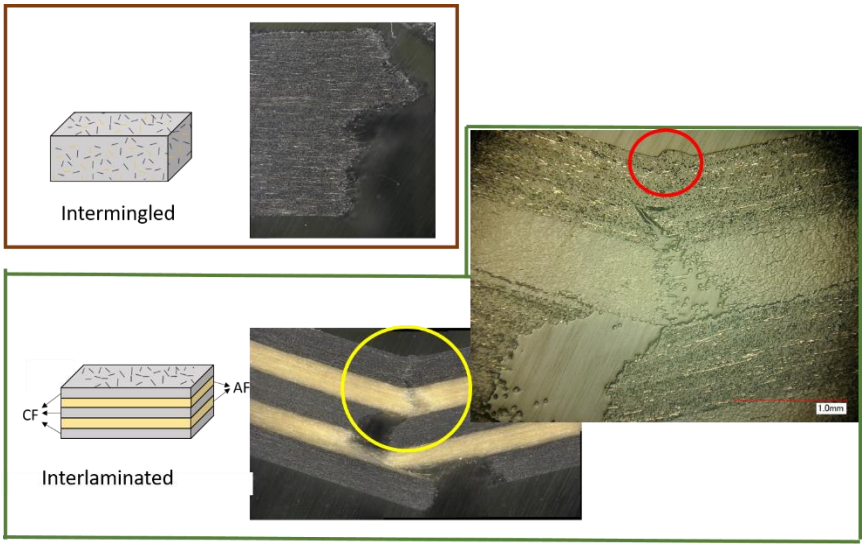

Figure 3-22 Fracture observation of two types of hybrids

3.3.2.3. The result of izod impact test

As Figure 3-23 shows, in the case of interlaminated hybrid, with aramid fiber length increase, the energy absorption capacity increased, which is attributed to the higher effect of fiber contact length in hybrid with longer aramid fiber where it requires more energy to detach and fail. When comparing two kinds of hybrid structure, it shows interlaminated hybrid can absorb more energy because of the stage-like failure and also the delamination. Those are main contribution to energy storage. Meanwhile, the aramid layer also displayed failure stopper role as the specimen failure step by step shown in Figure 3-24.

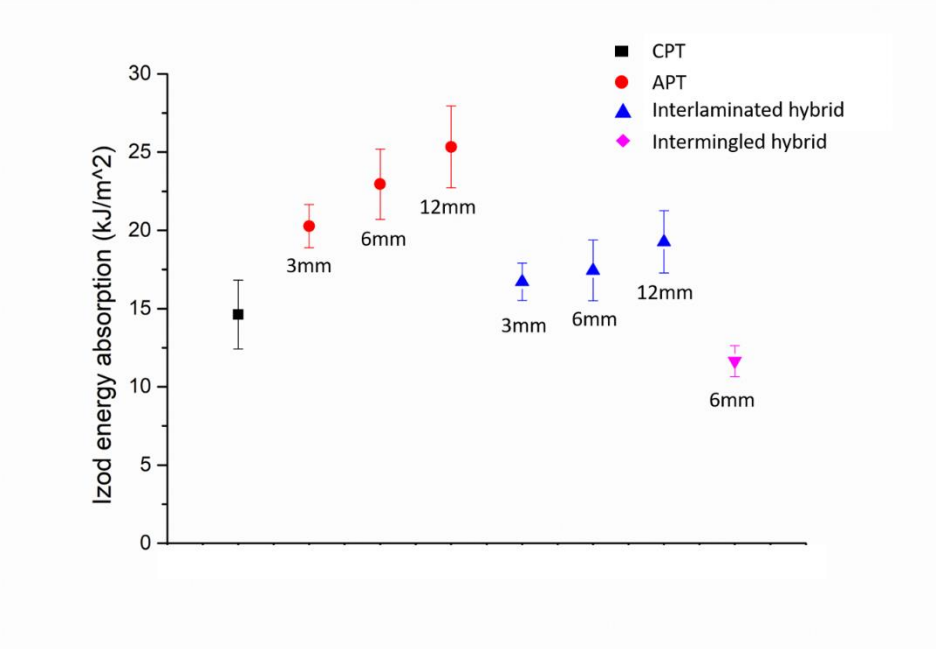

Figure 3-23 Izod impact energy absorption of the hybrids and the controls

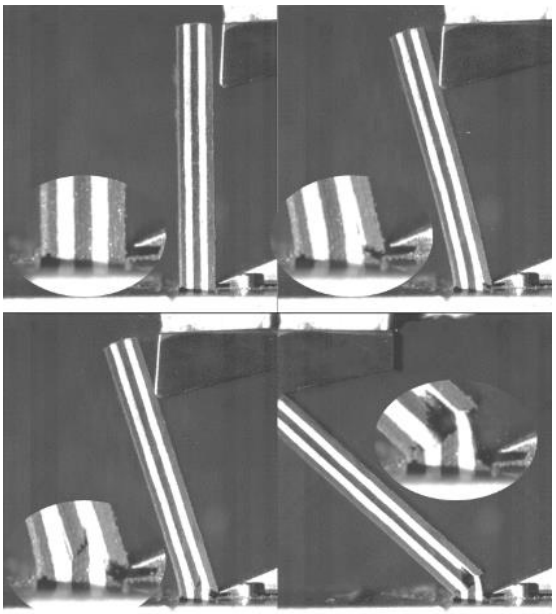

Figure 3-24 The failure mode of hybrids in izod impact test

3.3.2.4. The result of three-point impact test

In three point impact test, the impact loading was applied to freely supported beam. And the impact speed is double that of izod impact test as shown in Figure 3-25. With increase in aramid

fiber length, energy absorption ability increases. And the interlaminated hybrid has better energy absorption capacity than intermingled hybrid. Meanwhile, the energy absorption of hybrid with 12 mm long aramid fiber is even around 4 times higher than that of pure CPT, which can also be seen from the displacement-load curves (Figure 3-26), that carbon paper contributed to the elastic impact region while the aramid fiber portion determined the curve extension. Meanwhile, from the record of high speed camera records, hybrid beams failed step by step as Figure 3-27 shows.

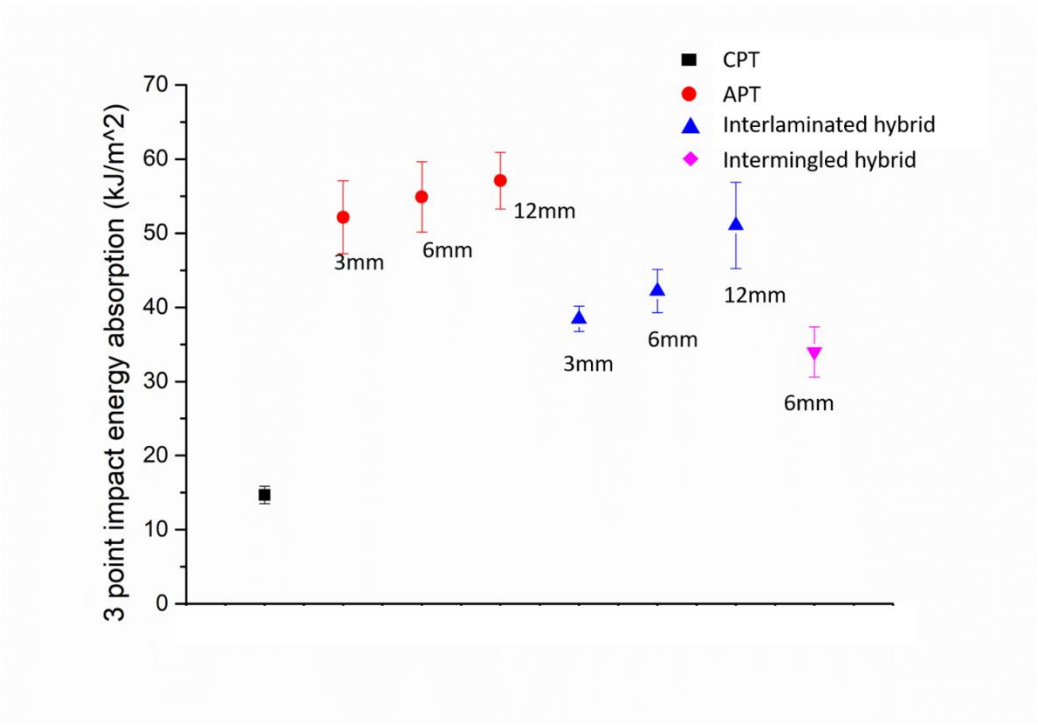

Figure 3-25 Three-point impact energy absorption of the hybrids and the controls

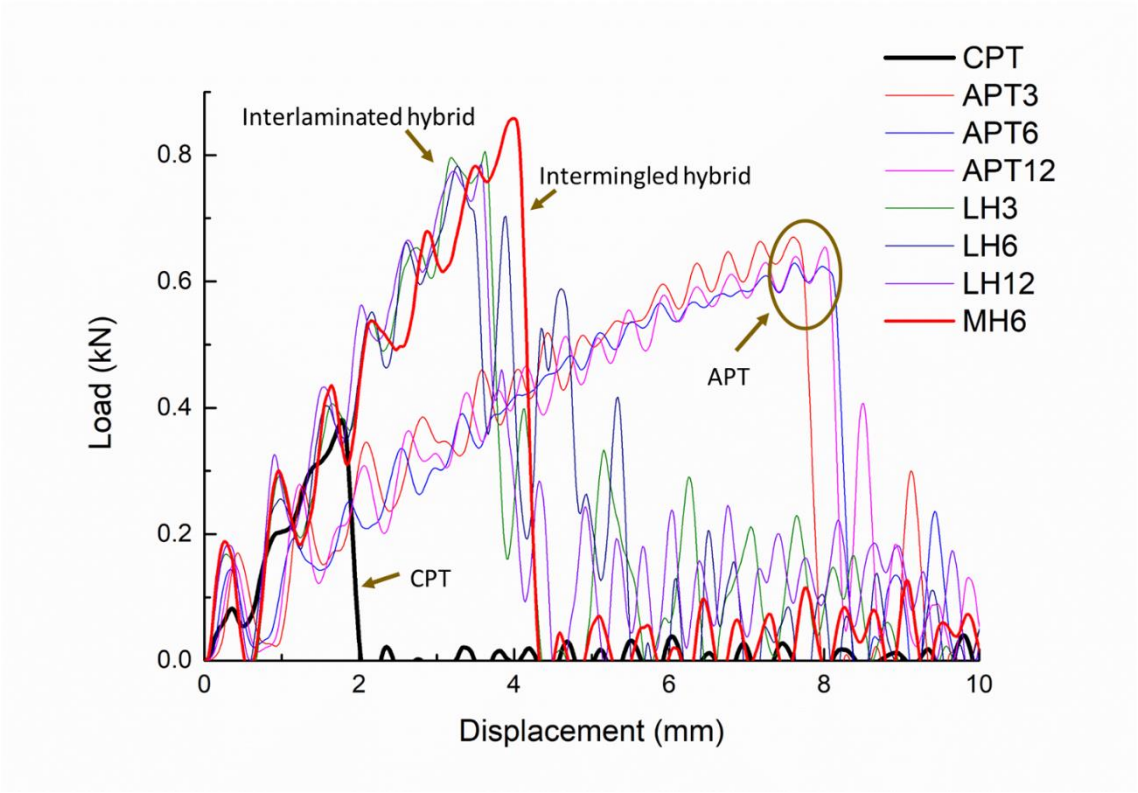

Figure 3-26 The load-displacement curves of the three-point impact test

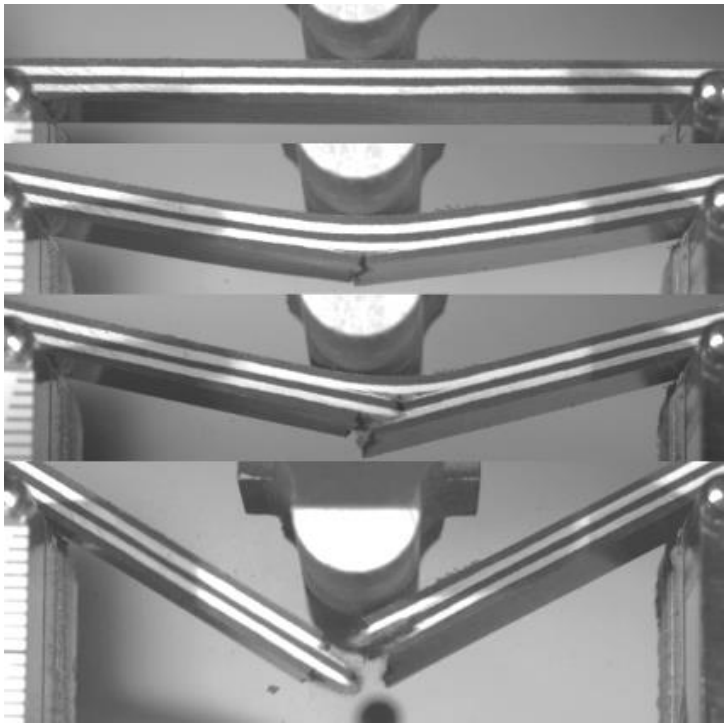

Figure 3-27 The failure mode of the hybrids in three-point impact test

With different fiber lengths in interlaminated hybrids, although all of them show stage-like failure process, failure details are different among them as shown in Figure 3-28. In the case of LH3, time span between first drop and second drop is quit short that the bottom four layers were failed almost at the same time due to dynamic condition where the effective fiber length decrease compared with static testing condition. In the case of LH6, the time span between first drop and second drop extended a bit but still less than that in the case of LH12 which can sustain further and produce longer delamination length to absorb more energy during failure.

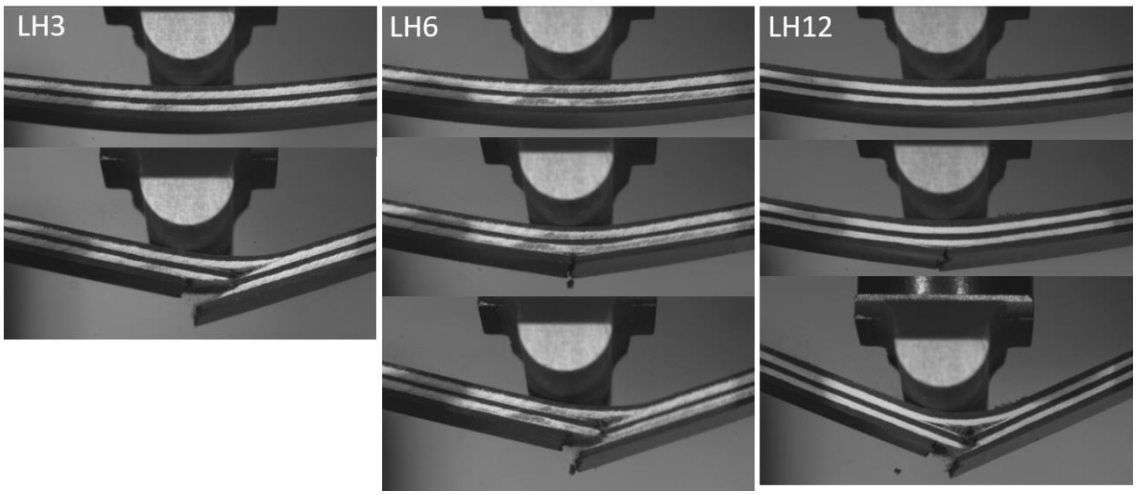

Figure 3-28 The failure mode comparison of the hybrids with different fiber lengths

3.3.3. Conclusion

In this study, discontinuous aramid fiber papers were applied to hybridize with discontinuous carbon fiber papers and reinforce with thermoplastic. Flexure and energy absorption behavior were investigated among the hybrid panels with different aramid fiber length.

To sum up, In general, hybridized Carbon fiber/aramid fiber paper reinforced thermoplastics have positive hybrid effect. Fiber length effect is not apparently in static loading, but hybrid with longer aramid fiber obtain larger energy absorption capacity in dynamic loading. Last but not least, interlaminate structure of hybrid overwhelmed intermingled hybrid because it has a comprehensive better performance.

3.4. Summary

In this chapter, discontinuous aramid fiber papers were applied to hybridize with discontinuous carbon fiber papers and reinforce with thermoplastic. Flexural and energy absorption behavior were investigated among the hybrid panels with various interlayer stacking sequence and different aramid fiber length. The following shows the conclusions:

- In general, hybridized carbon fiber/aramid fiber paper reinforced thermoplastics have positive hybrid effect.
- "Carbon outside" hybrids not only shows higher flexural property but also displays stage-like fracture. The effect of "fracture stopper" performed by aramid paper layers are more apparent in "carbon outside" hybrids.
- Hybrid reinforcement takes better effect when the segments setting numbers are lesser.
- Fiber length effect is not apparently in static loading, but hybrid with longer aramid fiber obtain larger energy absorption capacity in dynamic loading.
- Interlaminate structure of hybrid overwhelmed intermingled hybrid because it has a comprehensive better performance in terms of energy absorption capacity thanks to its stage-like failure process.
- For developing this kind of hybrids, it is necessary to optimize the structure more precisely. Further analytical and numerical discussion is required in future work.

4. Deconsolidation of short rCF reinforced thermoplastic and its application

4.1. Introduction

In this chapter, discontinuous carbon fiber-reinforced thermoplastics were used as both the facing and core materials with the aim of achieving high-speed molding, complex-shaped parts, and better closed-loop recyclability.

4.2. Sandwich with spring-backed CPT-PP core

In this section, the facing material was made of ultra-thin chopped CF tape-reinforced thermoplastics (UT-CTT), while the CPT was used as the core material. To improve the mechanical properties along the thickness direction and minimize delamination, needle punching was used to join stacks of CPT sheets. This avoided the use of other techniques like conventional 3D weaving and stitching which can introduce over-constraint problems related to closed loops and knots produced by the complex procedure, which may significantly deteriorate the quality of the structure, restrict the spring-back process, and is crucial for producing cores with different deconsolidation levels and out-of-plane thicknesses. Two needle-punching densities were compared in this study. In addition, we discussed the effects of using a CPA-PA6 sheet as the adhesive layer and different spring back ratios. Furthermore, the flexural rigidity of the sandwich panels was calculated based on beam theory and compared with experimental results. X-ray micro-computed tomography (CT) analysis was also conducted to investigate the fiber orientation of the cores in order to further verify the influence of needle punching on the sandwich panels.

4.2.1. Materials and methods

4.2.1.1. Materials

Two kinds of CPT (Awa Paper Co. Ltd.) sheets were used: one composed of modified polypropylene (PP) fibers and short CF 6 mm in length (CPT-PP sheet); and the other consisting of polyamide 6 (PA6) fibers and 6-mm-long carbon fibers (CPT-PA6 sheet). Both CPT sheets were prepared using a paper-making process where short resin fibers and carbon fibers were mixed thoroughly in water; then, the suspension was post-processed using hot compression into paper-like substrates. Both types of CPT were used as core materials in the sandwich panels for needle-punching.

The sandwich facings were intermediate UT-CTT sheets made of unidirectional CF-PA6 prepreg tapes which were cut from the prepreg provided by the Industrial Technology Center of Fukui Prefecture, Japan. The tapes contained TR50S CF (Mitsubishi Rayon Co., Ltd.) and PA6 fibers (Mitsubishi Plastics Co., Ltd.) and were 18 mm long, 5 mm wide, and 44 μm thick. To make intermediate UT-CTT sheet, the tapes were randomly oriented by water dispersion and compression molding methods. The CF volume fraction and density values for the materials used here are given in Table 4-1.

Table 4-1 Carbon fiber volume fraction and density of the materials used in this study

	CPT-PP	**CPT-PA6**	**UT sheet**
CF V_f [%]	19.4	23.1	54.0
Density [g/cm^3]	1.09	1.30	1.51

4.2.1.2. Needle punching process

The conventional needle punching method is usually applied to un-bonded, loose fibers as opposed to directly to the carbon fiber paper stacks. To diminish the risk that may cause large-scale needle-breaks or machine breakdowns, we used the manual punching method to punch the stacks following the sequence of punching and pulling out by the needle with barbs. The

preliminary experimental needle-punching device was fabricated from a dense 1.4 mm × 1.4 mm mesh welded at the edge to an iron frame that had the same size as the cut CPT samples. A railing-like metal stage was also used as a support for the mesh to allow the needle barbs to punch through every sheet. The grid frame was placed on top of a pile of CPT sheets, which were stacked in the desired sequence with all edges well aligned. The frame prevented interlayer slippage during needle punching and also determined the punching depth; the needle was inserted until a reference mark reached the plane of the frame. In order to minimize errors during processing, we ensured that the CPT sheet stacks were punched with the needle perpendicular to the centers of the holes in the mesh. The needle point followed a serpentine pattern along the rows of the grid. In addition, after punching, the backside of each preform was carefully checked and only good quality preforms were selected. Schematics of the preliminary experimental devices and their operation are shown in Figure 4-1.

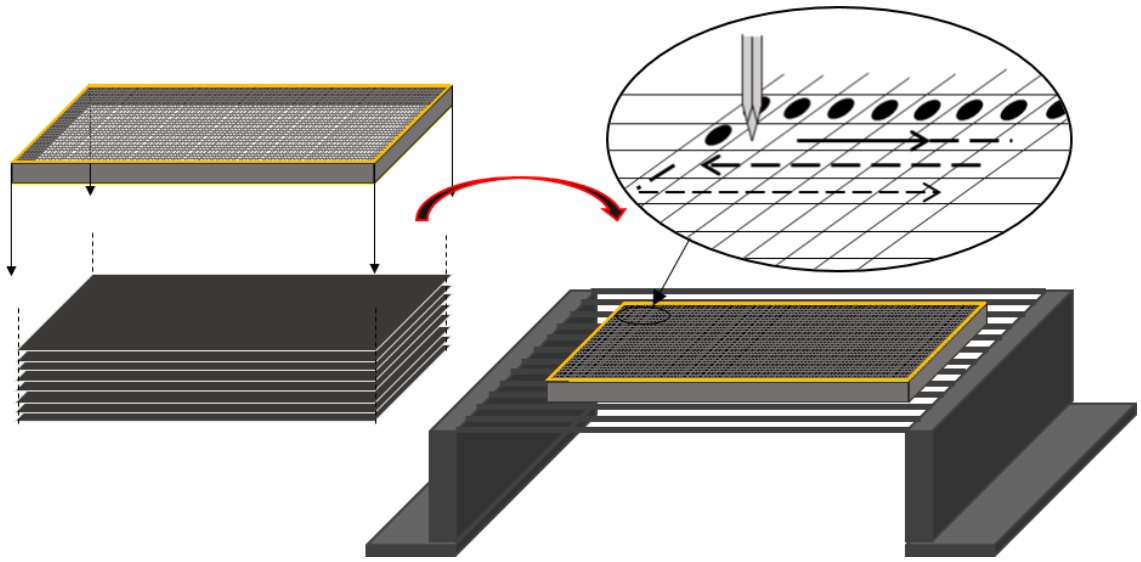

Figure 4-1 Schematic of the preliminary experimental devices and their operation

A triangular needle (FTD-132D 40SM) with a diameter of 0.5 mm and 6 barbs (Organ Needle Co., Ltd.) was used in the needle punching of the CPT sheets. In order to compare the effect of the needle punching density on the sandwich properties, we used punching densities of 12.7 punches/cm² and 51 punches/cm², as shown in Figure 4-2.

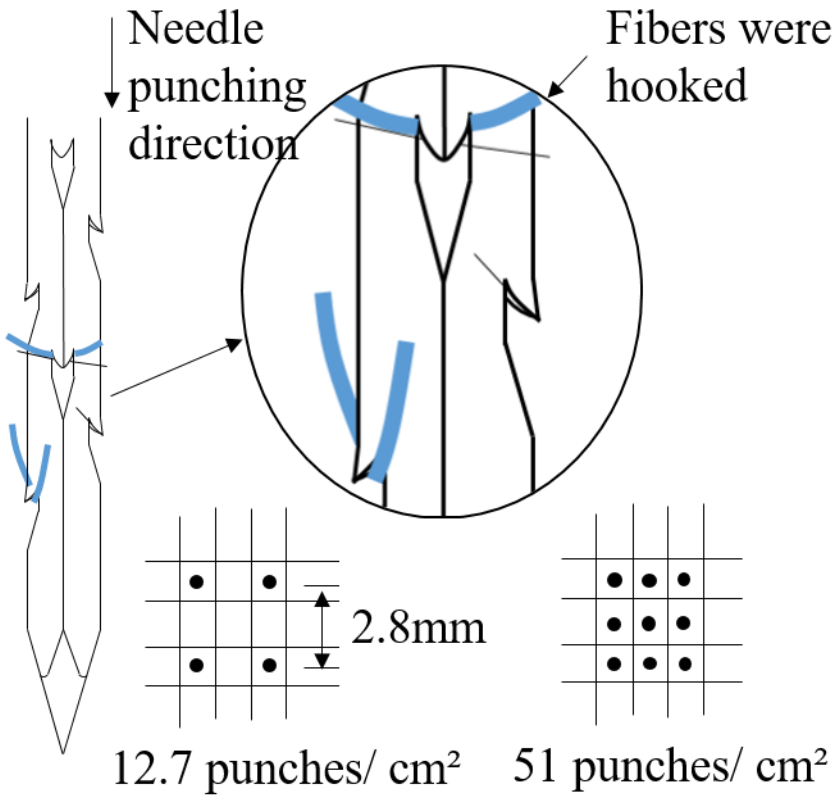

Figure 4-2 Schematic defining the needle punching density

4.2.1.3. Preparation of sandwich panels

The core of the composites was prepared by cutting samples from a CPT sheet roll and then stacking them (ensuring the same volume of CPT-PP sheets for each panel). Additional CPT-PA6 sheets were added to the upper and lower surfaces of the CPT-PP stacks as adhesive layers. Then, the needle-punching process described above was conducted to prepare each core preform. The facings of the sandwich panels comprised randomly oriented chopped CF tapes. First, 18-mm-long, 5-mm-wide tapes were cut from 44-μm-thick unidirectional CF/PA6 prepreg sheets. A known mass of tapes was then dispersed in water in a filtration vessel with a flat-steel filter. After the tapes were randomly dispersed, the water was removed and the tapes were deposited into a sheet on the filter. Then, the sheet was peeled from the filter and hot pressed at 110 ℃ for 3 min to evaporate the water. The dried sheet was then hot pressed at 265 ℃ under 5 MPa pressure for 1.5 min to form a preform sheet which will be used for stacking and molding. We call it

intermediate UT-CTT sheet and its thickness is around 0.16 mm. Both upper and lower facings of the sandwich panels were formed by compressing three intermediate UT-CTT sheets together.

A schematic diagram describing these intermediate sheets is shown in Figure 4-3.

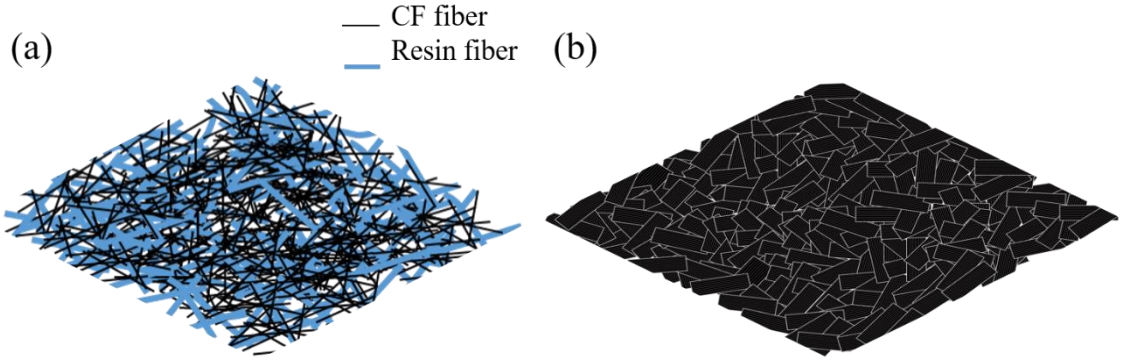

Figure 4-3 Schematic of (a) CPT and (b) UT-CTT intermediate sheets

After the core stacks and intermediate UT-CTT sheets were prepared, they were stacked and placed in a compression molding machine to pre-mold sandwich panels under 5 MPa pressure at 270 ℃ for 10 min, then cooled at a cooling rate of 5℃/min.

A spring-back process was conducted by reheating the pre-molded sandwich panel fabricated in the previous step with thickness-controlling spacers to produce different core thicknesses. The sandwich panel was placed onto a molding die again and the spring-back process was carried out under 5 MPa of pressure at 195 ℃, which is below the melting temperature of PA6 and above that of PP; hence, this heating process is expected to affect only the CPT-PP layer without changing the geometry or conditions of the facing or adhesive layers. The spring-back ratio is the ratio of the thicknesses of the CPT-PP layer before and after the spring-back process. Sandwich panels without needle punching were also prepared as a reference. Schematic diagrams summarizing the process of manufacturing the composite samples is shown in Figure 4-4.

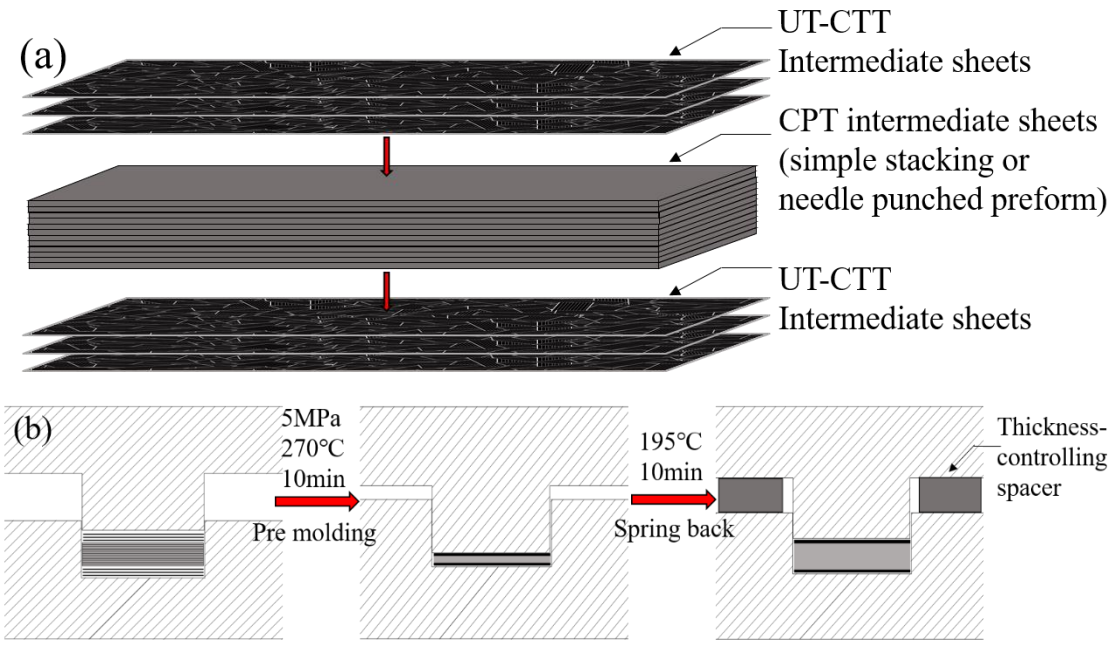

Figure 4-4 Schematic of the manufacturing process of the sandwich panels: (a) stacking sequence and (b) molding details

A summary of the different samples prepared in this study is shown in Table 4-2, where: C refers to sandwiches not subjected to needle punching; NC indicates needle-punched sandwiches with a needle-punching density of 12.7 punches/cm²; and HNC refers to needle-punched sandwiches with a needle-punching density of 51 punches/cm². In addition, SB3, SB2, SB1, and SB0 represent spring-back ratios of 2.9, 2.1, 1.6, and 1, respectively. The sample names of the sandwiches with adhesive layers are followed by -A. The "-" symbol represents adhesive layer or needle punching was not applied in the sandwich and the "*" symbol represents adhesive layer or needle punching was applied.

Table 4-2 Summary of the sample types with different facings/cores and the applied needle-punching density

	Spring-back ratio (SB)	**Core thickness [mm]**	**Facing thickness [mm]**	**CPT-PA6 adhesive**	**Needle punching density [punches/cm²]**
C3	2.9 (SB3)	2.6	0.5	-	-
C3-A	2.9 (SB3)	2.6	0.5	*	-
C2-A	2.1 (SB2)	1.9	0.5	*	-
C1-A	1.6 (SB1)	1.4	0.5	*	-
C0-A	1.0 (SB0)	0.9	0.5	*	-
NC3	2.9 (SB3)	2.6	0.5	-	12.7
NC3-A	2.9 (SB3)	2.6	0.5	*	12.7
NC2-A	2.1 (SB2)	1.9	0.5	*	12.7
NC0-A	1.0 (SB0)	0.9	0.5	*	12.7
HNC2-A	2.1 (SB2)	1.9	0.5	*	51
HNC1-A	1.6 (SB1)	1.4	0.5	*	51

4.2.1.4. Experiment

4.2.1.4.1. Four-point bending tests

Static four-point bending tests of both the cores and sandwich beams were performed in accordance with the ASTM D 6272-02 standard. Six coupons were prepared and tested to determine their flexural properties. Due to the different thicknesses of the cores and sandwiches, both the sample dimensions and test setups needed to be varied to achieve the same span-to-depth ratio. According to the standard, a support span-to-depth ratio of 32:1 was used and the load was applied at a point one-third of the length of the span from the edge. A table-top precision universal tester from Shimadzu Corporation was used. The length-to-depth ratio of the coupons was 40:1 and their width was 20 mm. The test was conducted using a rate of crosshead motion R for a load span of one third of the support span: $R = 0.185ZL2/d$ (mm/min), where L is the support span (mm), d is the depth of the beam (mm), and Z is the rate of straining of the outer fibers (mm/mm min) and was equal to 0.01 in our case. The radii of the loading noses and supports were 5 mm, while Teflon sheets (10-mm wide and 0.5-mm thick) were placed between the rollers and coupon to prevent local indentation failure. A dial indicator with 1 μm sensitivity (Kyowa Electronic

Instrument Co., Ltd.) was placed under the specimen to measure the deflection of the center of the beam. Figure 4-5 shows the test setup of the coupons under four-point loading.

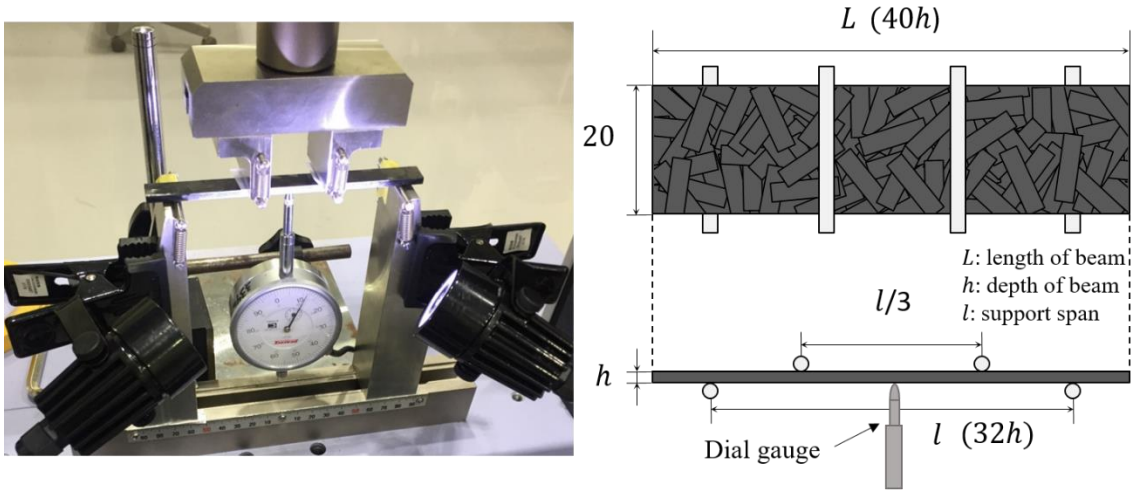

Figure 4-5 (Left) Photograph and (right) schematic diagram of the four-point bending test setup where the values are in mm.

4.2.1.4.2. Digital microscope observation

The fractured specimens were observed using a VHX-1000 digital microscope from Keyence Corporation, where the interface of facing-core and different types of failure modes were observed.

4.2.1.4.3. X-ray micro-CT scanning

The internal fiber orientations of the sandwiches were observed using a TDM1000-II 3D X-ray micro-CT scanning system (YAMATO Scientific Co., Ltd). A scan voltage of 50 kV and scan current of 48 mA were used. The 3D structural models and fiber orientation were acquired and analyzed using TRI/3D-FBR-DT software (RATOC Corporation). The out-of-plane fiber orientation (θ), as defined in Figure 4-6, was determined for panels with and without needle punching. To minimize variability introduced by the molding process, CT samples were cut from the same areas of both needle-punched and control panels; five samples were scanned and analyzed for each panel, as shown in Figure 4-7.

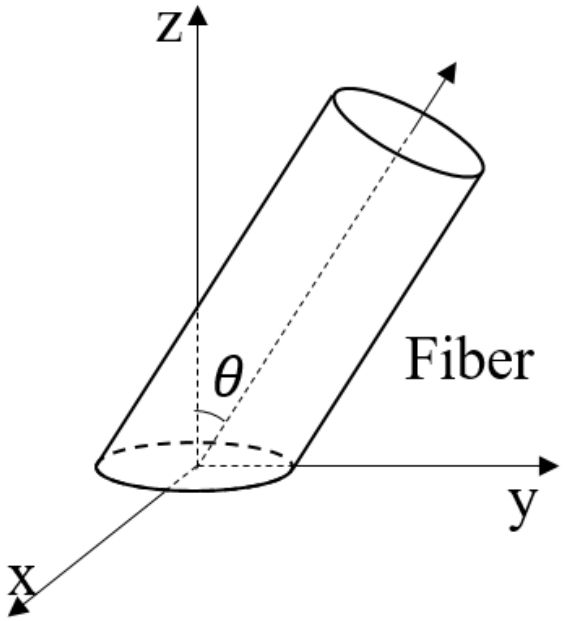

Figure 4-6 Schematic diagram representing out-of-plane fiber orientation θ

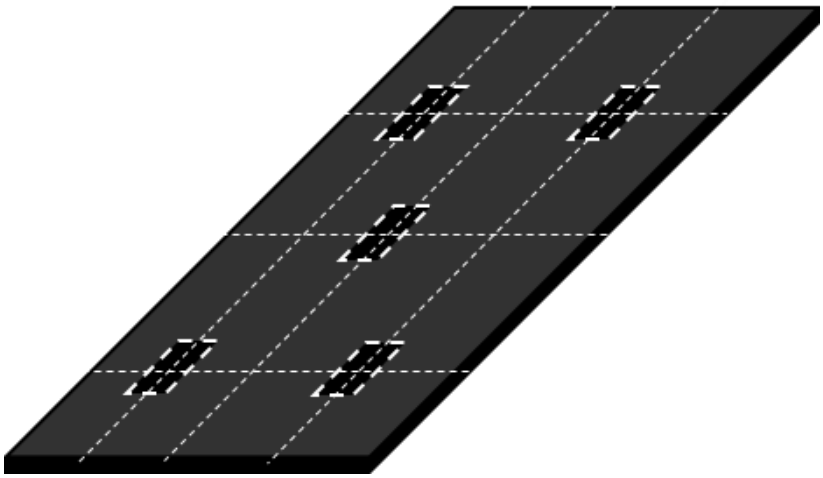

Figure 4-7 Schematic diagram showing the selection of positions for micro-CT scanning

4.2.2. Results and discussion

4.2.2.1. Flexural rigidity of sandwich panels

In this section, a spring-back core was used as the lightweight material in between two facings in the sandwich structure. This kind of structure can provide a high sectional moment of inertia and improve the flexural rigidity of the panel which is a very important parameter in structural design.

After being processed by the spring back process, thermoplastic matrix composites can show a significant change in their meso-structures as well as in their macro-performance [110]. In addition, the degree of thermal deconsolidation is related to many complex factors, including volume changes due to thermal expansion/contraction and chemical shrinkage, which can be characterized by the release of internal stresses and increase in porosity. Therefore, assuming ideality and linearity of all constituents, we used classical beam theory (ignoring shear deflection) and predicted its linear phase and rigidity to determine a threshold up to where a spring-back ratio can reach. This analysis was performed in order to further investigate the kinetics of deconsolidation on CF reinforced thermoplastic and the effect of the degree of deconsolidation on the macro-performance of this type of sandwich structure. A schematic diagram defining the cross-sectional area of the samples used in the calculations is shown as Figure 4-8. The nomenclature used in the following description of the calculations is given in Table 4-3.

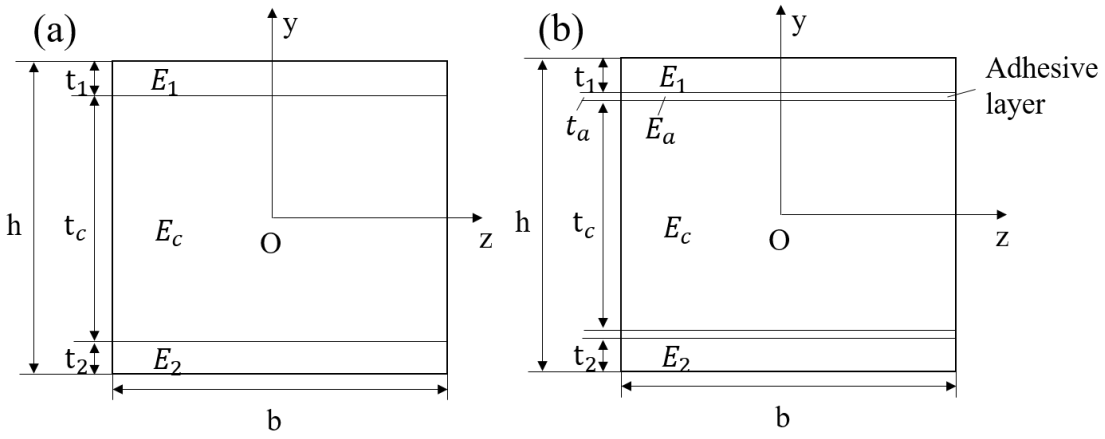

Figure 4-8 Schematic describing the calculation of the cross-sectional area of the sandwich structure (a) without adhesive layer I and (b) with adhesive layer II

Table 4-3 Nomenclature

Nomenclature			
t_1,	thickness of upper facing in sandwich	I_{eq}	equivalent sectional inertia moment of sandwich
t_2	thickness of bottom facing in sandwich	I_{eq_1}, I_{eq_2}	equivalent sectional inertia moment of facing
t_c	thickness of core in sandwich	I_{eq_c}	equivalent sectional inertia moment of core
t_a	thickness of adhesive layer	D_{I}	flexural rigidity of sandwich without adhesive layer
h	height of sandwich	D_{II}	flexural rigidity of sandwich with adhesive layer
A	area of cross section	ρ	curvature of natural surface
E_1, E_2	flexural modulus of facing	M	bending moment
E_f	flexural modulus of facing in sandwich	δ	deflection in center of beam
E_c	flexural modulus of core in sandwich	F	loading force
E_a	flexural modulus of adhesive layer	ρ_s	density of sandwich

Assuming that both facings were effective, according to the mechanical equilibrium conditions, the moment of inertia and rigidity are defined as shown in Equation 4-1 and Equation 4-2, respectively.

$$I_{eq} = \int_A y^2 \, dA \qquad \text{Equation 4-1}$$

$$\begin{aligned} D_{\mathrm{I}} &= E_1 I_{eq_1} + E_c I_{eq_c} + E_2 I_{eq_2} \\ &= E_1 \left[\frac{b t_1^3}{12} + \left(\frac{t_1 + t_c}{2} - y_c \right)^2 b t_1 \right] \\ &+ E_c \left[\frac{b t_c^3}{12} + (0 - y_c)^2 b t_c \right] \\ &+ E_2 \left[\frac{b t_2^3}{12} + \left(-\frac{t_2 + t_c}{2} - y_c \right)^2 b t_2 \right] \end{aligned} \qquad \text{Equation 4-2}$$

As the sandwich structure is symmetric with upper and bottom facings of equal thickness, point O (see Figure 4-8) is the centroid of the area. Therefore, we can obtain $y_c = 0; t_1 = t_2 = t_f;\ E_1 = E_2 = E_f$. Thus, Eq. (1) reduces to:

$$D_{\mathrm{I}} = \frac{E_f t_f^3 b}{6} + \frac{E_f \left(t_f + t_c \right)^2 t_f b}{2} + \frac{E_c t_c^3 b}{12} \qquad \text{Equation 4-3}$$

Similarly, the flexural rigidity of the sandwich structure with adhesive layers can be expressed as:

$$D_{II} = \frac{E_a t_a^3 b}{6} + \frac{E_a (t_a + t_c)^2 t_a b}{2} + \frac{E_c t_c^3 b}{12} + \frac{2E_f}{3}\left\{\left(\frac{t_c}{2} + t_f + t_a\right)^3 - \left(\frac{t_c}{2} + t_f\right)^3\right\} \quad \text{Equation 4-4}$$

where E_f and E_a are material property of the facing and adhesive material, respectively, which can be obtained easily from experiments. However, the parameters of the core material are quite sensitive to its spring-back ratio. The experimentally determined flexural modulus values of the cores with corresponding spring-back ratio were fitted using an exponential decay curve, as shown in Figure 4-9. The flexural modulus E_c for a specific thickness after applying the spring-back process can be determined from this fitted curve.

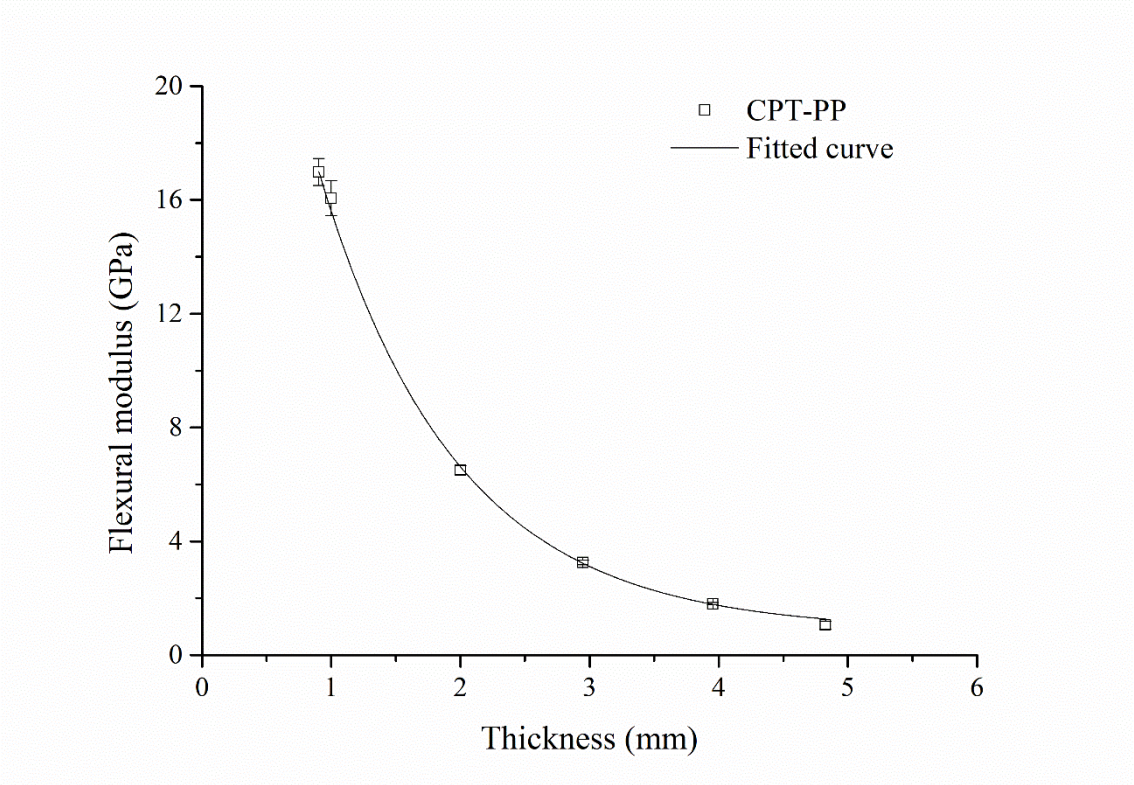

Figure 4-9 Elastic modulus as a function of thickness of CPT-PP

Because the span used in the experiments varied with the thickness of the sandwich panel (in accordance with the standard ASTM D 6272-02), the values of flexural rigidity determined from the slope of the experimental load-displacement curves are not directly comparable with the calculated results. Therefore, the experimental results were transformed into a form only related to the modulus and moment of inertia; this was undertaken according to the theory of mechanics of materials and considering the schematic diagram for four-point loading given in Figure 4-10.

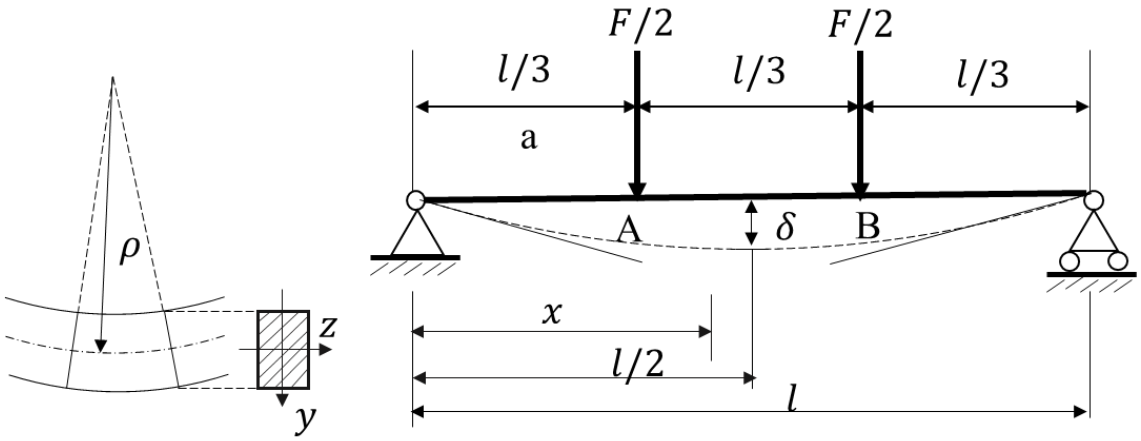

Figure 4-10 Schematic diagram of the four-point loading geometry

According to the mechanics of materials, the curvature of the neutral surface is expressed as

$$\frac{1}{\rho} = \frac{M}{EI} \qquad \text{Equation 4-5}$$

where the curvature of a plane curve at a point (x, δ) of the curve can be expressed as

$$\frac{1}{\rho} = \frac{\frac{d^2\delta}{dx^2}}{\left[1 + \left(\frac{d\delta}{dx}\right)^2\right]^{3/2}} \qquad \text{Equation 4-6}$$

In the case of the elastic curve of a beam, the slope dy/dx is very small, resulting in:

$$\frac{1}{\rho} = \frac{d^2\delta}{dx^2} \qquad \text{Equation 4-7}$$

Thus, Equation 4-5 can be expressed as

$$\frac{d^2\delta}{dx^2} = \frac{M(x)}{EI} \qquad \text{Equation 4-8}$$

Based on the loading condition used in the four-point bending test, the deflection of point (x, δ) under loading at point A can be expressed as

$$\delta_{Ax} = \frac{F/2 \cdot ax}{6lEI}(l^2 - x^2 - a^2) \qquad \text{Equation 4-9}$$

When $x = l/2$, the deflection of the center point of the beam under both loading points will be

$$\delta = \delta_{l/2} = 2\delta_{Ax} \quad \text{Equation 4-10}$$

$$\delta = \frac{23Fl^3}{1296EI} \quad \text{Equation 4-11}$$

Therefore, assuming $\mathrm{k} = \frac{F}{\delta}$

$$\mathrm{EI} = \mathrm{k}\frac{23l^3}{1296} \quad \text{Equation 4-12}$$

All sandwich structures were compared, as shown in Figure 4-11 and Table 4-4.

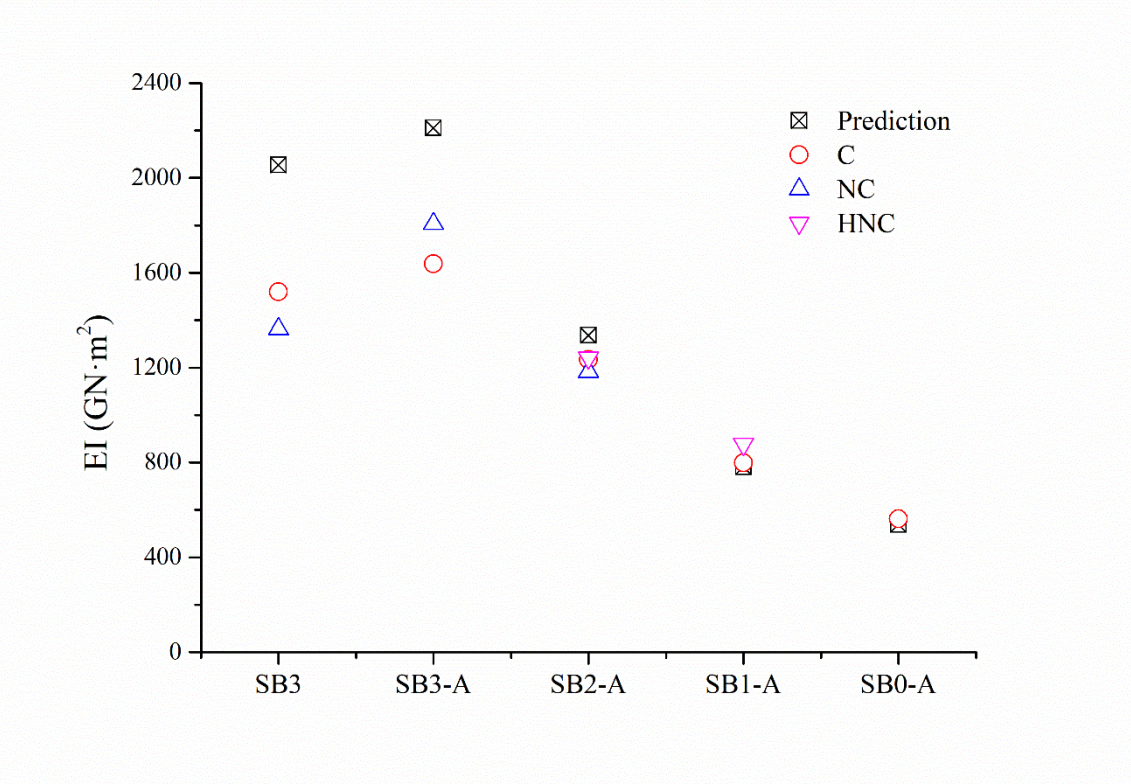

Figure 4-11 Rigidity of the various sandwich panels

Table 4-4 Summary of EI values for various sandwich panel samples

	EI (GN·m²)				Spring back ratio	CPT-PA6 adhesive
	Prediction	**C**	**NC**	**HNC**		
SB3	2054.1	1519.518	1363.297	-	2.9	-
SB3-A	2210.0	1638.074	1806.085	-	2.9	*
SB2-A	1336.4	1235.077	1182.850	1242.015	2.1	*
SB1-A	781.2	798.147	-	876.702	1.6	*
SB0-A	538.0	562.670	-	-	1	*

The sandwich structure with an adhesive layer showed a higher rigidity than equivalent samples without the adhesive due to the slight increase in thickness. Comparing the predicted and experiment results, some variations were observed in the case of SB3, which was attributed to the relatively high void content that reduced the rigidity of the core; however, the calculated values matched well with the experimental ones for lower spring back ratios. Considering the spring-back ratio, although the characteristics of the interior of the core varied, the rigidity increased with increase of thickness.

In general, needle punching can damage the preform structure, often leading to detrimental results. However, in this study, needle-punched sandwiches were stiffer than those without the adhesive layer, and neither needle-punching density affected the flexural properties of the sandwiches; this will be discussed in more detail in following sections.

4.2.2.2. Effect of needle-punching on failure modes

It is well known that the dominant failure mode of composite sandwich structures with most conventional core materials is core shear or skin-core interaction failures [124]. However, three different failure modes of the sandwiches with a spring-back ratio of 2 were observed during our tests, as shown in Figure 4-12, where (a) shows a delamination fracture in the sandwich not subjected to needle punching, which occurred between the CPT-PP layer and adhesive CPT-PA6 layer. However, in the case of the sandwich subjected to 12.7 punches/cm² needle punching density (Figure 4-12 (b)), the failure occurred in an intra-CPT-PP-layer location. The third failure mode can be seen in the sandwich subjected to a needle-punching density of 51 punches/cm² (Figure 4-12 (c)), in which the core was strong enough to resist delamination failure by sustaining transverse shear forces; hence, compression failure occurred primarily on the upper facing.

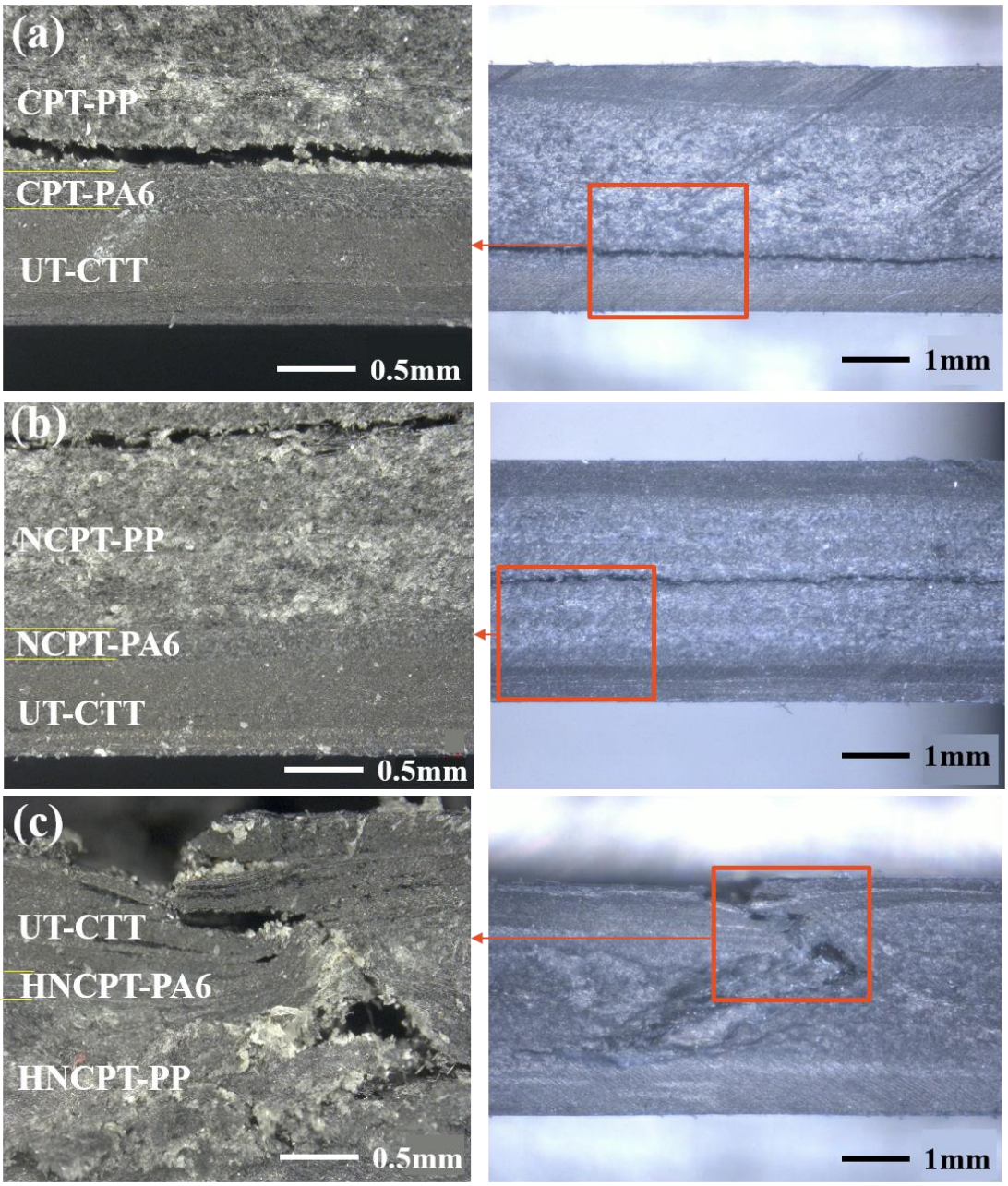

Figure 4-12 Optical observation of the fracture area of the sandwich with a spring back ratio of 2: (a) without needle punching, and needle punching density of (b) 12.7 pins/cm² and (c) 51 pins/cm².

In the absence of the needle-punching process, the adhesive between the facing and core could not resist primary shear forces due to the poor compatibility of PA6 and PP. During needle punching, when the needle passes through the CPT stacking, PA6 fibers were carried through the

sheet by the needle barbs and introduced into the CPT-PP layer, as shown in the microscopy image in Figure 4-13. Figure 4-14 shows a schematic diagram of the needle-punched CPT-PA6 and CPT-PP sheets, where the PA6 fibers that were punched into the CPT-PP sheets formed PA6 pillars and improved the adhesion between the facing and the core. For a needle-punching density of 12.7 punches/cm², the adhesion between the facing and core was enhanced, but the number of PA6 pillars was insufficient to improve the out-of-plane mechanical properties of the core; thus, delamination occurred within CPT-PP layers. When the needle punching density increased to 51 punches/cm², the core was strong enough to support the facing without significant out-of-plane deflection.

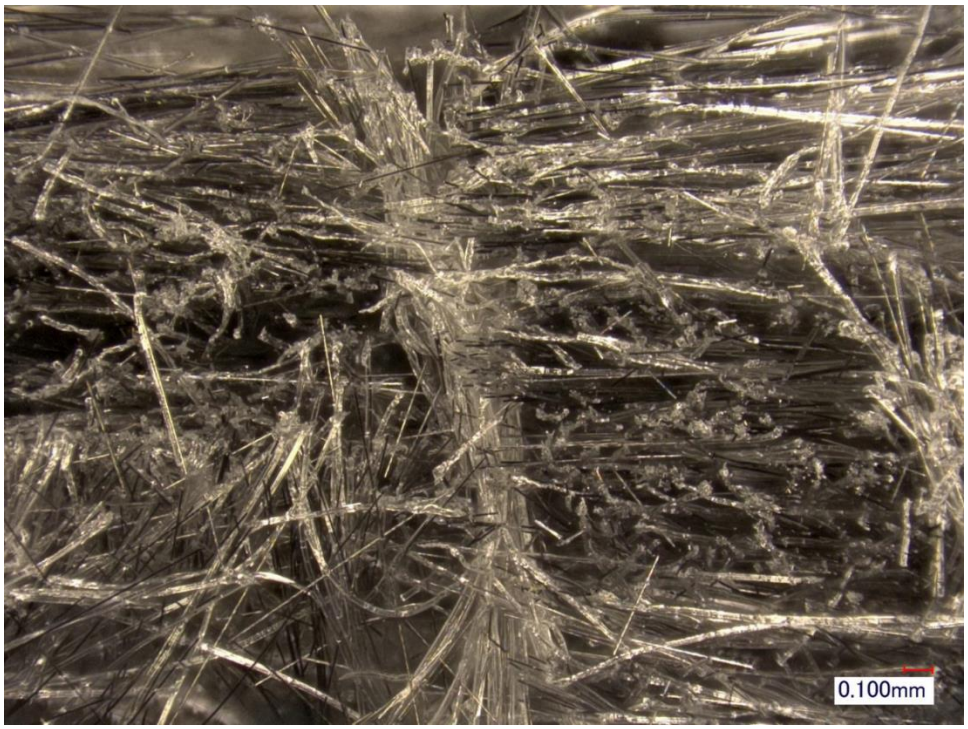

Figure 4-13 Optical microscopy image of the cross-section of a needle-punched CPT sheet

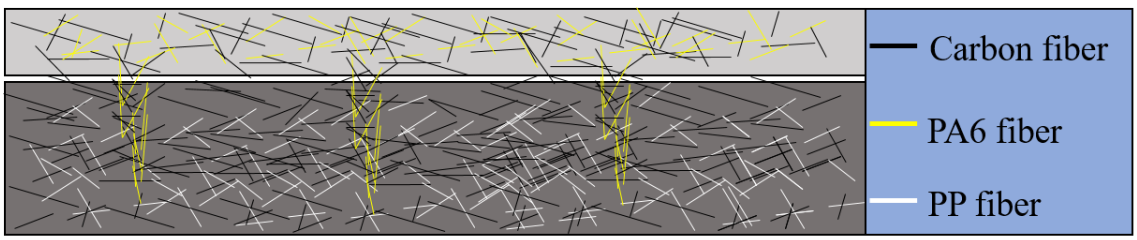

Figure 4-14 Schematic diagram of needle-punched CPT-PA6 and CPT-PP sheets

In the case of the sandwich with a spring-back ratio of 1.5, the deconsolidation level was lower than that of the sample with a spring-back ratio of 2. Hence, the out-of-plane stiffness of the core was higher for the sample with the lower spring-back ratio, but the upper facing failed due to delamination between the facing and core, as shown in Figure 4-15 (a). In the case of the sample with the same spring-back ratio, but subjected to a needle punching density of 51 punches/cm², the crack propagated through the cross-section without delamination, as shown in Figure 4-15 (b).

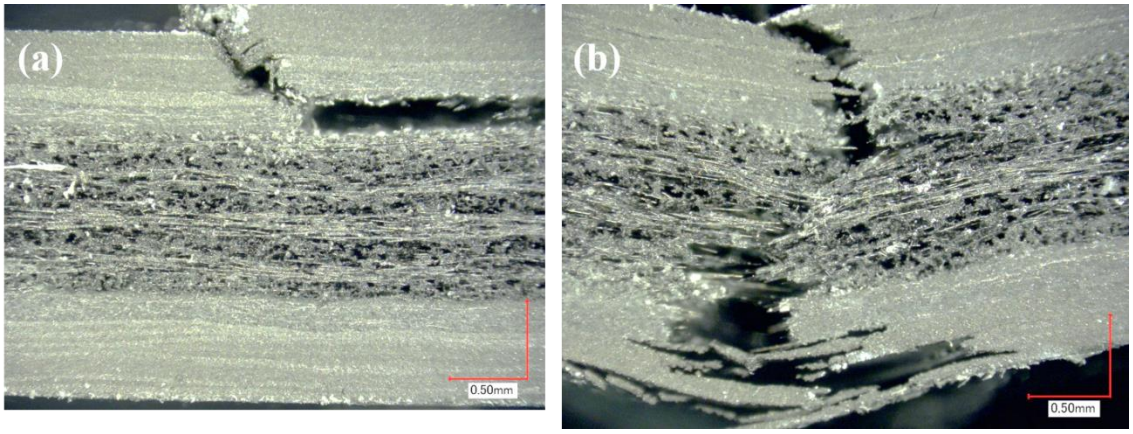

Figure 4-15 Optical observation of the fracture area of the sandwich with spring back ratio 1.5: (a) without needle punching and (b) needle punching density of 51 pins/cm²

4.2.2.3. X-ray micro-CT scanning

As resin fibers are flexible, they can easily form a loop inside the preform during needle punching, while the stiff short CF cannot form a loop, but rather reorient, slip or break in response to punching. In addition, compared with CF, resin fiber is more easily observed under optical microscopy due to its larger diameter and semitransparent characteristic, as shown in Figure 4-13. Therefore, we used X-ray micro-CT scanning analysis to determine the CF orientation and visualize the internal structure of the sandwich samples with spring-backed cores and the general structure of randomly orientated CF after the binary processing.

After X-ray micro-CT scanning, the internal structure of the sandwich was visualized, where the core was clearly distinguished from the facing by the void size and porosity. Therefore, before the binarization, we selected the core area based on the porosity differences, as shown in Figure 4-16. Then, the fiber orientation of the selected volume was analyzed.

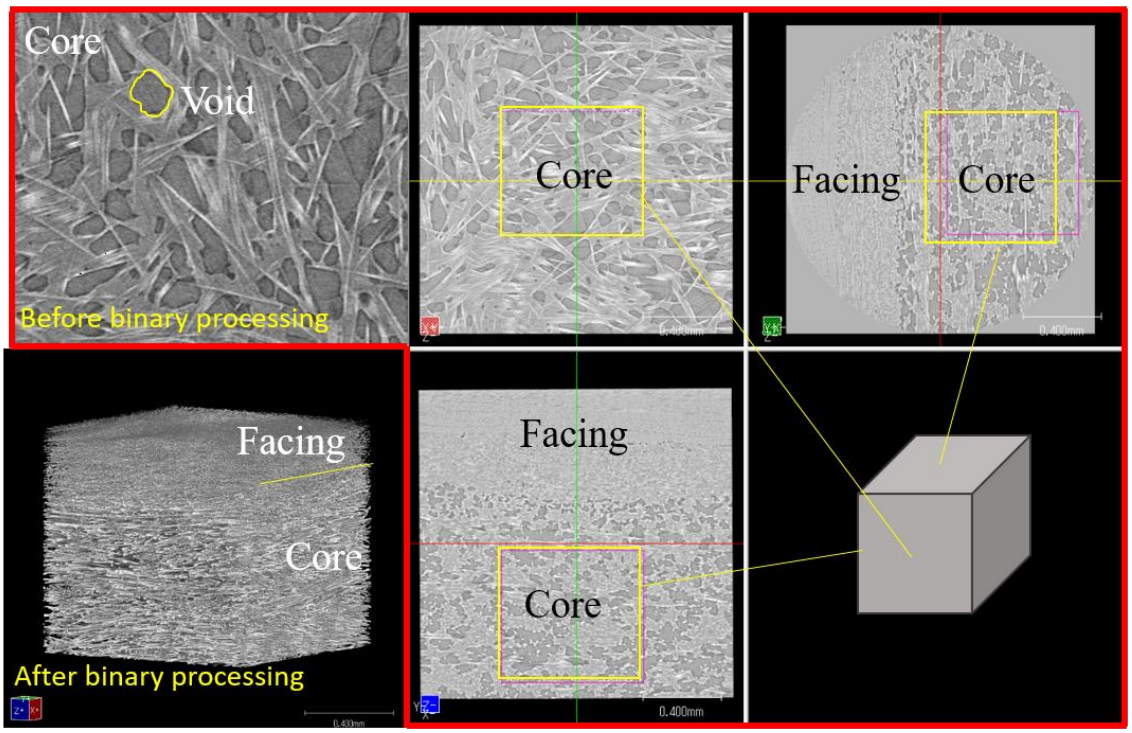

Figure 4-16 X-ray micro-CT scanning analysis

Using a statistical method, the fiber orientation information was collected and plotted as a scatter plot of relative frequency vs. θ, as shown in Figure 4-17 shows. Then, curve fitting was conducted using a Lorentz function, as shown in Equation 4-13 to qualitatively evaluate the out-of-plane fiber orientation of both needle-punched and control panels.

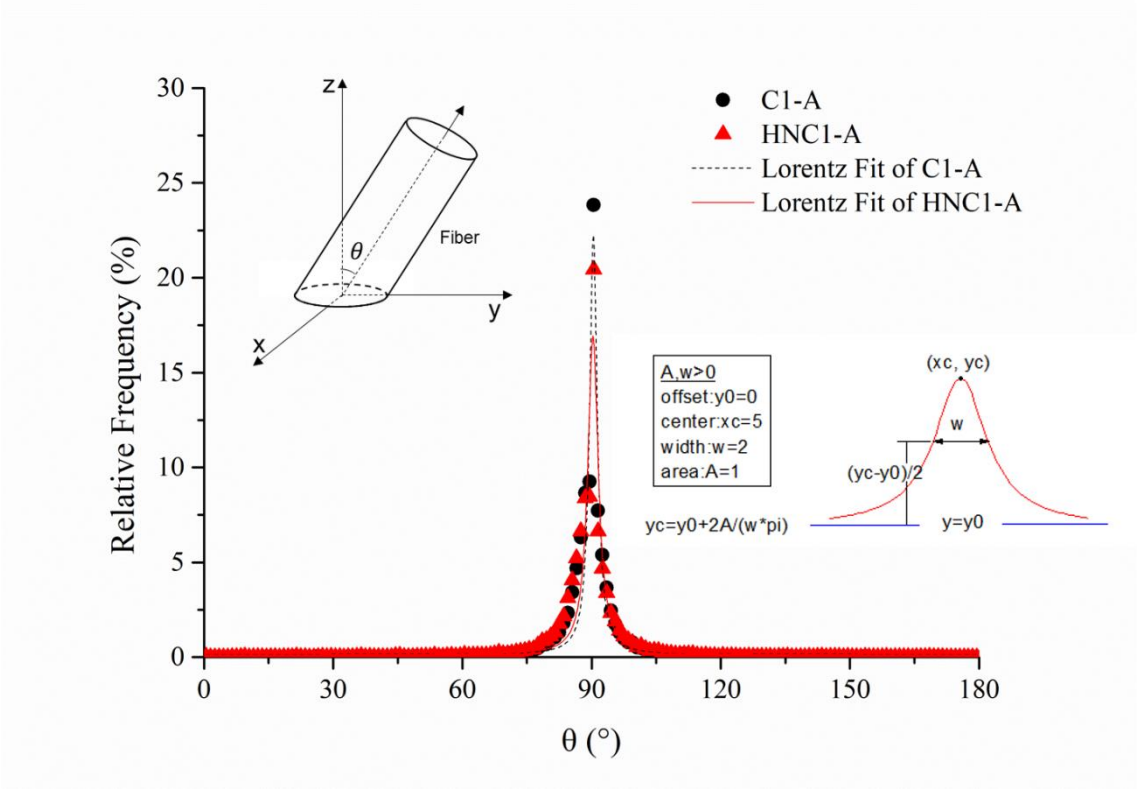

Figure 4-17 Angular distribution of the out-of-plane fiber orientation of spring back ratio 1.5 of control panels and those needle-punched with a density of 51 pins/cm²

$$y_c = y_0 + \frac{2A}{\pi}\frac{w}{4(x - x_c)^2 + w^2} \qquad \text{Equation 4-13}$$

Finally, the scale parameters y_c and w were obtained, as shown in Table 4-5. It was obvious that most fibers were oriented at 90° (in-plane direction), while the y_c and w values were 16.833 and 2.950 for panels needle-punched at 51 punches/cm² with a spring-back ratio of 1.5, implying that more fibers were oriented in the out-of-plane direction compared with the control panels with the same spring-back ratio (with y_c and w values of 22.153 and 2.125, respectively). This proves that the needle-punching process not only introduced PA6 resin fibers into the CPT-PP layer, but also changed the direction of some CF to an out-of-plane direction, thereby increasing the out-of-plane stiffness and reducing the risk of the delamination of the sandwich structure.

Table 4-5 Parameters obtained by Lorentz fitting

	C1-A		HNC1-A	
	Value	**Standard error**	**Value**	**Standard error**
y_c	22.153	0.657	16.833	0.640
w	2.125	0.090	2.950	0.162

4.2.3. Conclusion

In this study, CPT sheets were stacked and needle punched (with different needle-punching densities), then used as a core material between UT-CTT facings under different spring-back ratios to produce sandwich panels with different core thickness.

The sandwich structures prepared with adhesive layers showed enhanced rigidity, while needle-punching pulled PA6 fibers into the CPT-PP sheets, which resulted in enhanced adhesion between the CPT-PA6 and CPT-PP layers without sacrifying the flexural properties of the sandwich beams. A higher needle-punching density enhanced the interlaminar shear property of the core and reduced delamination failure. The calculated and experimental rigidity values matched well for samples with low spring-back ratios. X-ray micro-CT results indicated that the needle-punching process changed the direction of the CF to an out-of-plane direction, in addition to introducing PA6 resin fibers into the CPT-PP layer; this increased the out-of-plane stiffness and reduced the occurrence of delamination.

Therefore, we conclude that needle-punching has the potential to improve the mechanical properties of sandwich structures with carbon-paper cores. The work also demonstrates that comprehensive and insightful experimental and theoretical studies are needed to obtain better understanding of the complex effects of the spring-back ratio of cores subjected to needle punching under through-thickness loading.

4.3. Sandwich with spring-backed CPT-PA6 core

In previous section, sandwich was made by spring-backed CPT-PP core and CTT-PA6 facing where in order not to influence facing during spring back process, different resin materials were

utilized between the core and the facing. However, due to the weakness of spring-backed CPT-PP core, needle punching was applied to improve its shear property.

In this section, relatively strong core material, spring-backed CPT-PA6 was applied, meanwhile, to reduce the influence caused by the thickness variation of CTT facing, unidirectional carbon fiber prepreg (UD) was adopted as facing material. Several sandwich making methods were designed and compared through mechanical tests. Conventional sandwich with foam core was also made to compare with sandwich with spring-backed core.

4.3.1. Materials and methods

The core material is CPT-PA6 sheet which has been introduced in Chapter 3. As control groups, two types of foam material (Rohacell, Sunwa Trading Corporation) used in various engineering fields were applied as well.

The sandwich facings were made of unidirectional CF-PA6 prepreg (UD; CF, TR50S, Mitsubishi Rayon Co., Ltd.; PA6, Mitsubishi Plastics Co., Ltd.) that was 132 μm in thickness.

4.3.2. Separate forming and Two-step forming

4.3.2.1. Manufacturing

In the core preparation, CPT sheets fit for the mold size were cut from carbon paper roll and then stacked.

In the facing preparation, UD sheets were cut from 132 μm-thick unidirectional CF/PA6 prepreg in 0° direction. Both the upper facing and bottom facing were made with 3 pieces of UD sheets which can be molded into 0.5 mm-thick plate under the pressure enough for fully consolidated laminate.

Separate forming is the process where the facings and the core were molded separately; the facings were molded under 5 MPa pressure and 270 °C; the core was molded under 5 MPa

pressure, 265 ℃ and then reheated with spacers to spring back the core into expected thickness under 265 °C; and then the facings and the core were attached by epoxy adhesive and cured in 24 hours.

In two-step forming process, both core and facings were stacked and placed onto the mold to manufacture sandwich panels directly with 5 MPa pressure, 270 °C for 10 min; spring-back process was conducted by reheating the sandwich panel made in the previous step with spacers to produce different core thickness in sandwich structure. The sandwich panel was set onto molding die again and spring-back process was carried out with 5 MPa pressure, 265 °C.

The processing schematic diagrams are shown as Figure 4-18 and Figure 4-19.

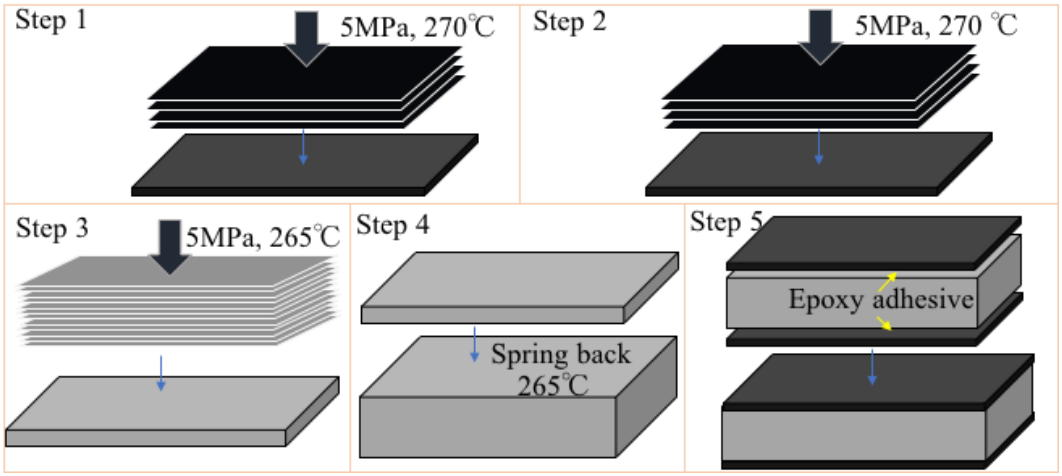

Figure 4-18 Separate forming

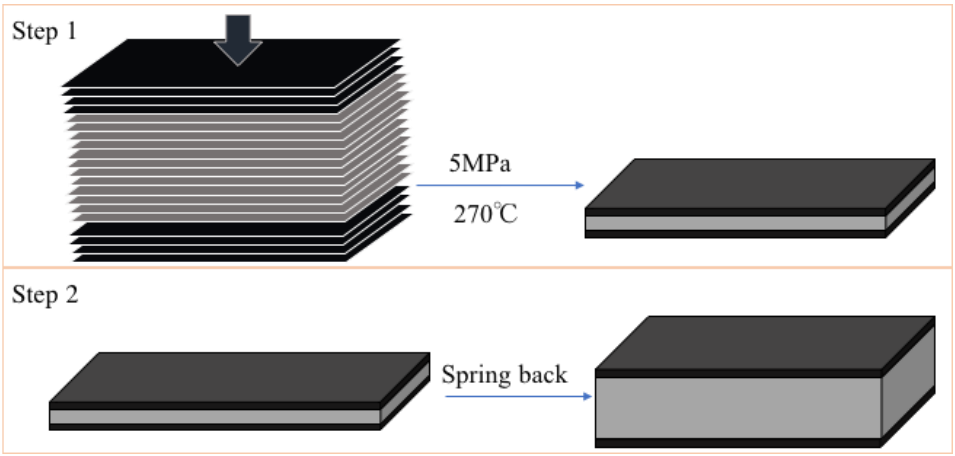

Figure 4-19 Two-step forming

A summary of the different samples prepared by these two forming methods is shown as Table 4-6, where: S refers to sandwiches made by separate forming method with epoxy adhesive which is marked as E; T indicates sandwiches made by two-step forming method. In addition, spring-back ratio (SB) is the concept mentioned in previous section. It is the ratio of the panel thickness in fully consolidated state to the panel thickness after spring-back processing. The higher the SB is, the more porous or void content or the weaker the core is and the lower consolidation level the sandwich is.

Table 4-6 Summary of the sample types made by separate forming and two-step forming methods

	Forming method	**Spring back ratio (SB)**	**Core thickness [mm]**	**Facing thickness [mm]**
EC280S	Separate forming	2.80	1.8	0.5
C266T	Two-step forming	2.66	1.66	
C289T		2.89	1.89	
C314T		3.14	2.14	

4.3.2.2. Four-point bending test

Static four-point bending test of the sandwich beams were performed in accordance with the ASTM D 6272-02 standard. The support span-to-depth ratio of 32:1 was chosen and the load was applied at the one third point of the span through a table-top precision universal tester from

Shimadzu Corporation, meanwhile, a dial indicator was set under the specimen to measure the deflection of the center of the beam as shown in Figure 4-20.

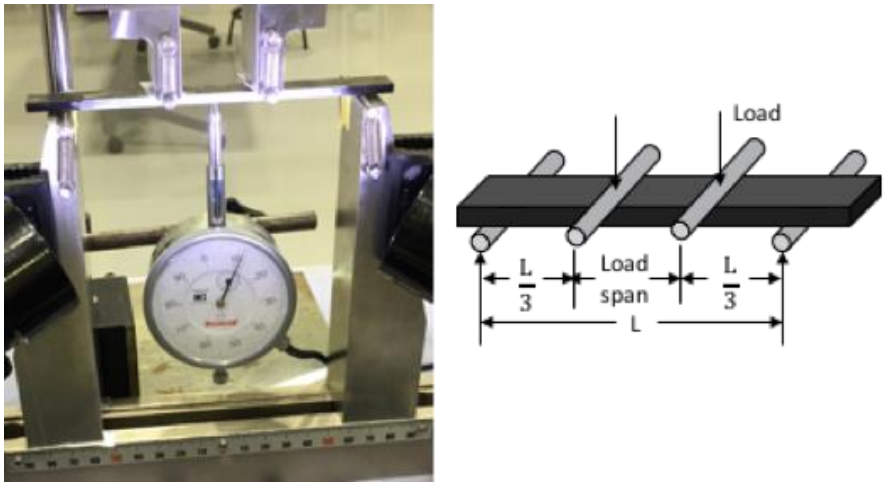

Figure 4-20 Four-point bending test setup

4.3.2.3. Results and discussion

4.3.2.3.1. The result of four-point bending test

Figure 4-21 shows the flexural modulus and flexural strength comparison among all types of sandwich panels. It is obvious that with the increase in spring-back ratio, both the flexural modulus and flexural strength decrease in the case of two-step forming. It was because the increase of spring back ratio resulted in the thickness change, which led to increase the void content and to deteriorate the performance of the core.

It is assumed that the flexural behavior of the sandwich panel by separate forming method would show better than the ones by two-step forming method because there are epoxy adhesive layer between the facing and the core, meanwhile, in two-step forming process, the facing suffered from the thermal heating twice with the high temperature which might probably cause thermal damage on the facing and affect the performance of the whole beam. But the flexural property of the sandwich with SB2.8 by separate forming method show close to the ones with SB2.66 and SB2.89 by two-step forming method, moreover, the value scatter of the sandwich with SB2.8 by separate forming method is relatively large because of some uncontrollable factors like the

ununiformity of the adhesive spread, therefore de-bonding of the facing and the core occurred during the test on several specimens.

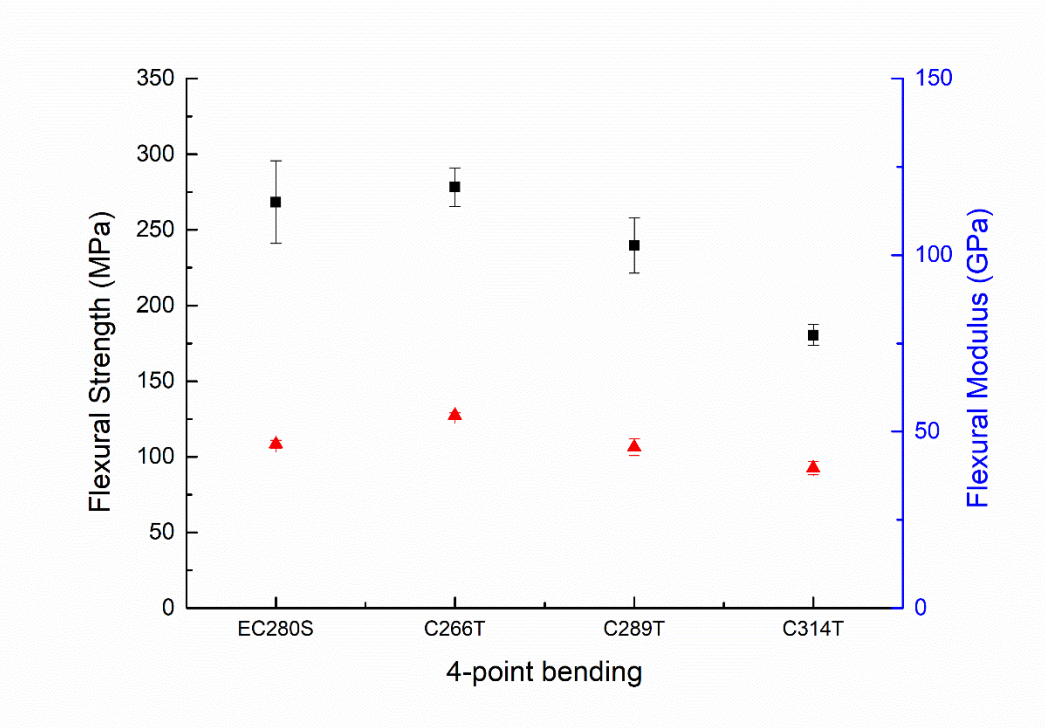

Figure 4-21 The flexural modulus and flexural strength of the sandwiches beams

4.3.2.3.2. Specific flexural property

As is known to us, sandwich composites are becoming more and more popular in structural design, mainly for their ability to substantially decrease weight, thus, the evaluation of weight lightening potential should be also discussed, which can be seen from Figure 4-22. The sandwiches by two-step forming method show superior to the one by separate forming when it comes to the specific flexural values. Compared with some steel and aluminum materials, the sandwiches have even more than four times higher specific flexural stiffness and strength. It is reasonable to get them into further investigation and some real application.

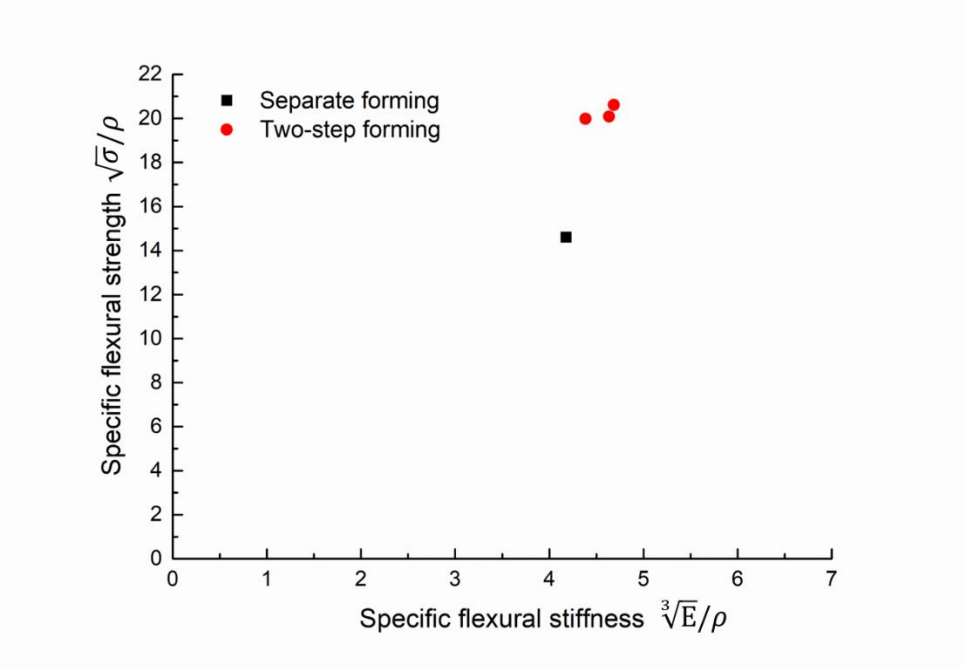

Figure 4-22 Comparison of weight lightening potential between sandwiches made by Separate forming and Two-step forming

4.3.2.3.3. Optical observation

Figure 4-23 shows the side-views of the upper facing and the interface area between facing and core in the sandwich beams. The resin-rich or void area of the facing in the case of separate formed sandwich evenly spread through the whole cross-section, however, those gather outwardly in the two-step forming sandwiches, which can also be seen in the cross-section of the sandwiches as Figure 4-24 and Figure 4-25 where the fibers around interface are more compact in two-step formed sandwich than separately formed sandwich. It is assumed that in the two-step forming method, due to the stress un-equilibrium on facing and core, the stress release pressure of the core led some resin of the facing flow into the core and compress the facing outwardly. The situation is the same in the bottom facing and interface, which can explain why the adhesive between facing and core is adequate and the facing thickness is thinner than expectation in two-step forming sandwiches.

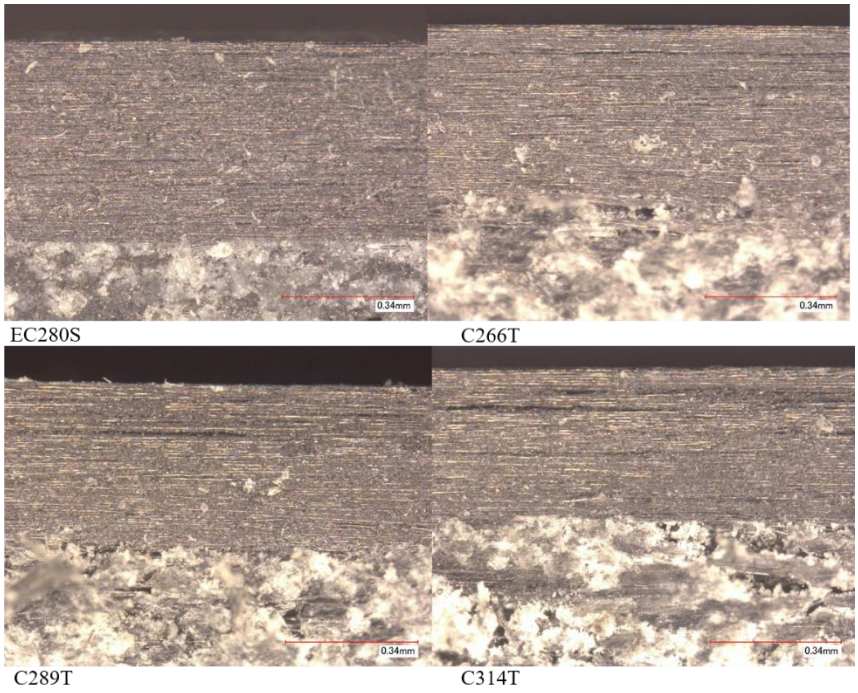

Figure 4-23 The side-view of the upper facing and the interface

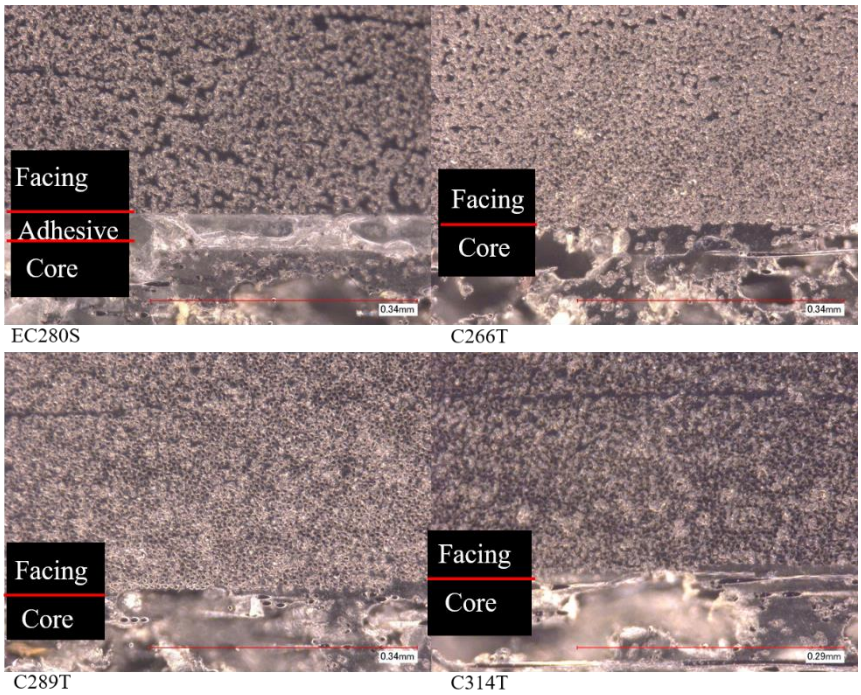

Figure 4-24 The cross-section of the upper facing and the interface area between facing and core

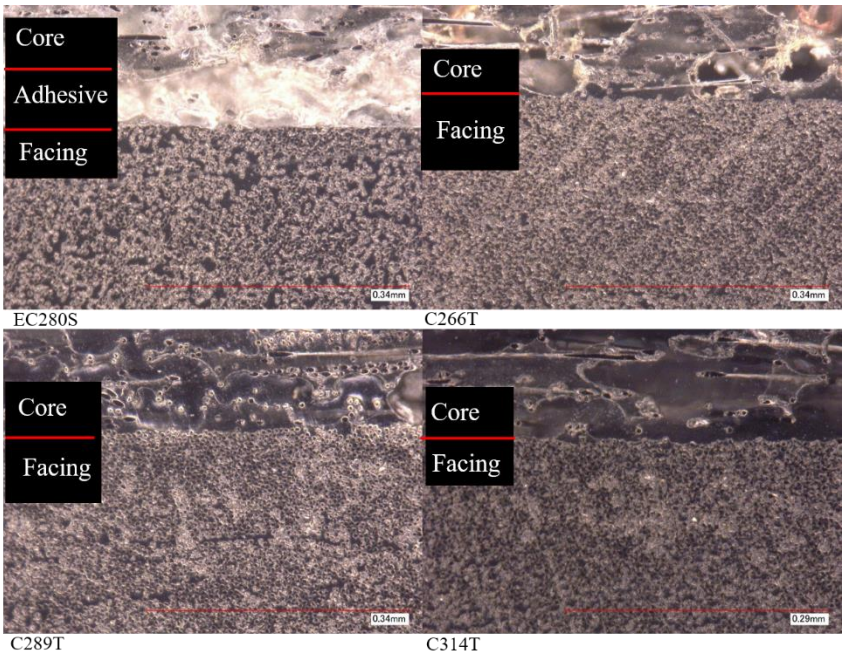

Figure 4-25 The cross-sections of the bottom facing and the interface area between facing and core

From the optical observation of the fracture cross section as Figure 4-26, it is obvious to see that the de-bonding occurs in the sandwich by separate forming method, even worse, almost the whole facing was peeled from the core in some specimens, as mentioned above, which might be caused by the ununiformity of the adhesive spread between facing and core. But the adhesive between the facing and the core shows better in sandwiches by two-step forming method where the upper facing failed first accompanied with the core deteriorated and it can be seen that the facings were always attached with core material beneath the facing body as shown in the two-step forming case.

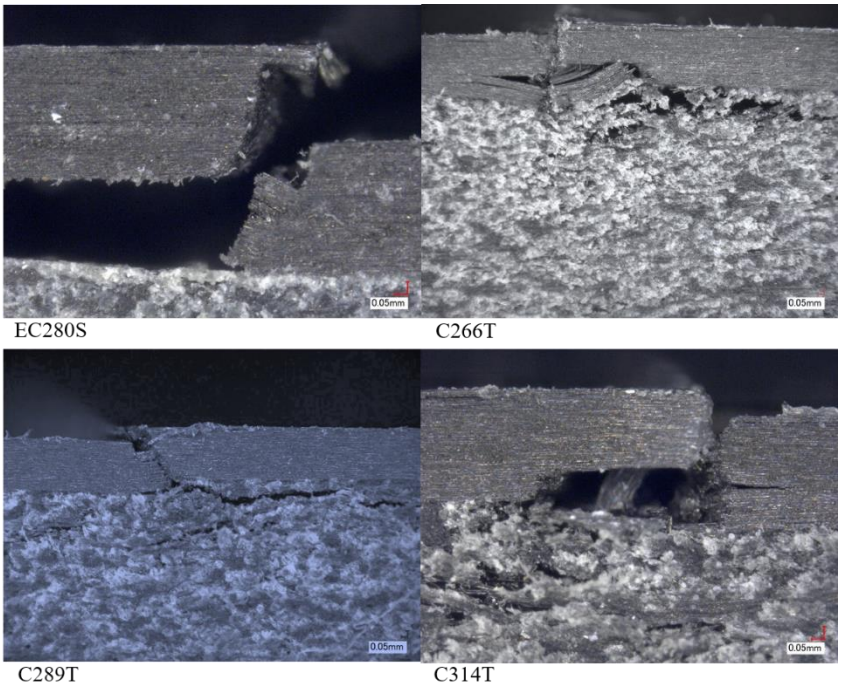

Figure 4-26 The fracture cross-section of specimens

4.3.2.4. Conclusion

CPT-PA6 was investigated as core material sandwiched with UD facing by two kinds of methods. And the comparison was made through different spring-back ratio and flexural behavior of the CPT-PA6 core sandwich beams. It is found two-step forming method is feasible to manufacture the UD/CPT sandwich because of its high production efficiency and better flexural behavior in sandwiches compared with the separate forming method.

4.3.3. Two-step forming and One-step forming

4.3.3.1. Manufacturing

From previous work, it is found two-step forming method is feasible to manufacture the UD/CPT sandwich because of its high production efficiency and better flexural behavior in sandwiches where in two-step forming, both core and facings were stacked and placed onto the mold to manufacture sandwich panels directly with designated temperature and pressure; and then the panel was set onto molding die again to be reheated under thickness controllers for getting

designated thick sandwich panels. In this study, a further improved forming method named one-step forming method was introduced to achieve higher production efficiency where both core and facings were stacked and placed onto the mold with thickness controllers directly under 5 MPa pressure at 270 °C. The processing schematic diagrams of two-step forming method and one-step forming method are shown in Figure 4-27 and Figure 4-28, respectively.

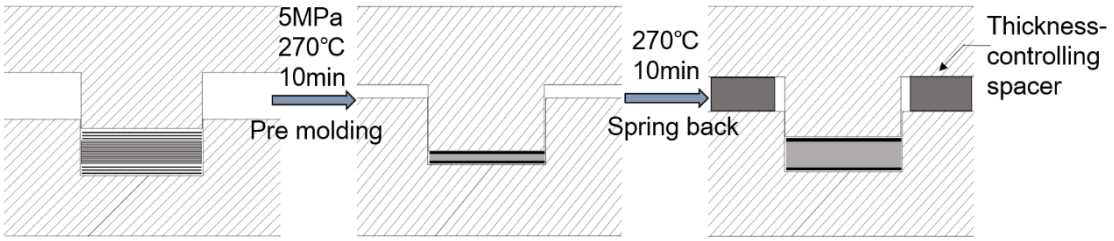

Figure 4-27 Two-step forming

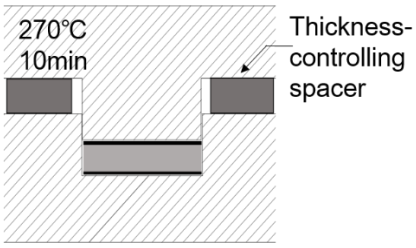

Figure 4-28 One-step forming

In this study, we fixed the whole thickness of sandwich panels by controlling spacers with different thicknesses, 4 mm and 5 mm. And then the spring-back ratio was adjusted by changing the number of CPT sheets. Different facing thickness in sandwich panels were also investigated. Therefore, we can make comparisons by picking specific groups to study the effect of the facing thickness to core thickness ratio. A summary of the different samples prepared by these two forming methods is shown in Table 4-7, where the front number 5 or 4 refers to sandwiches with 5 mm or 4 mm whole thickness; the front T represent the sandwiches with 1-mm thickness while the front S represent the sandwiches with 0.25-mm thickness; the last T or O means two-step forming and one-step forming, respectively; FCL indicates the foam-core sandwich with relatively low density and FCH indicates the foam-core sandwich with relatively high density.

Table 4-7 Summary of the sample types made by Two-step forming and One-step forming methods

	Forming method	**Spring back ratio (SB)**	**Facing thickness [mm]**	**Core thickness [mm]**	**Sandwich thickness [mm]**
5T-C300T	Two-step forming	3.00	1	3	5
5T-C300O		3.00	1	3	5
5T-C257O		2.57	1	3	5
5T-C225O		2.25	1	3	5
5-C300O	One-step forming	3.00	0.5	4	5
4-C300O		3.00	0.5	3	4
4-C257O		2.57	0.5	3	4
4S-C257O		2.57	0.25	3.5	4
4-FCL	Separate forming	-	0.5	3	4
4-FCH		-	0.5	3	4

4.3.3.2. Experiment

4.3.3.2.1. Three-point bending test

Static three-point bending test of the sandwich beams were performed in accordance with the ASTM D 790 standard through a table-top precision universal tester from Shimadzu Corporation.

4.3.3.2.2. Three point impact test

Three point impact test was performed by a high-speed puncture impact tester from Shimadzu Corporation HITS-P10. The impact speed was approximately 3.8 m/s.

4.3.3.3. Results and discussions

4.3.3.3.1. Comparison between two-step and one-step forming methods

It was assumed that the flexural behavior of the sandwich panels by two-step method would show better than the ones by one-step forming method because we supposed that the first step in the two-step method would make sure the resin infiltrated well through the whole sandwich body and reduce the void content, however, it is obvious that the sandwich under one-step forming method

share almost the same flexural property compared the one under two-step forming as Figure 4-29 shows. Therefore, it is considered that the facing suffered from the thermal heating twice with the high temperature which might probably cause thermal damage on the facing and affect the performance of the whole beam in the two-step forming, meanwhile, in the case of one-step forming, although the designated thickness might lead to lack of pressure to mold the facings, stress release during heating on CPT sheets provide certain pressure to compact facings.

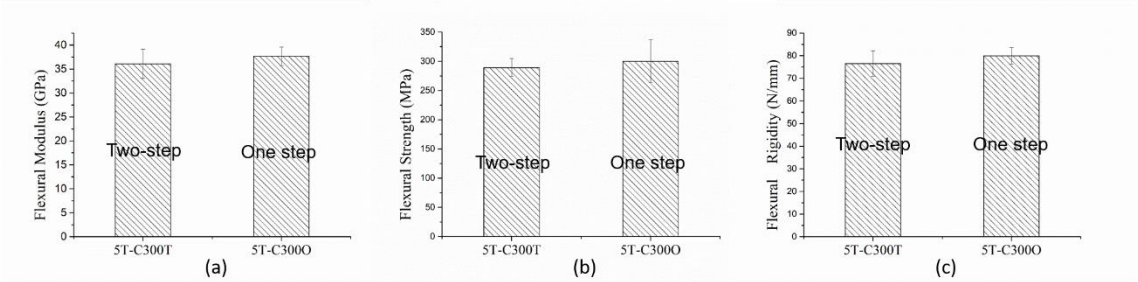

Figure 4-29 The flexural property comparison between Two-step and One-step forming: (a) Flexural modulus; (b) Flexural strength; (c) Flexural rigidity

Through optical observation (Figure 4-30), it can be found that there are voids groups in facing of the two-step forming one close to the interface of facing the core, however, one-step formed sandwich does not show many voids groups. Therefore, it is considered that the facing suffered from the thermal heating twice with the high temperature which might probably cause thermal damage on the facing and affect the performance of the whole beam in the two-step forming, meanwhile, in the case of one-step forming, stress release during heating on CPT sheets did provide certain pressure to compact facings.

Then, it can be concluded that one-step forming is a kind of efficient and promising method to manufacture this kind of sandwich. Therefore, the following discussion is all concerning the results of one-step forming method sandwiches.

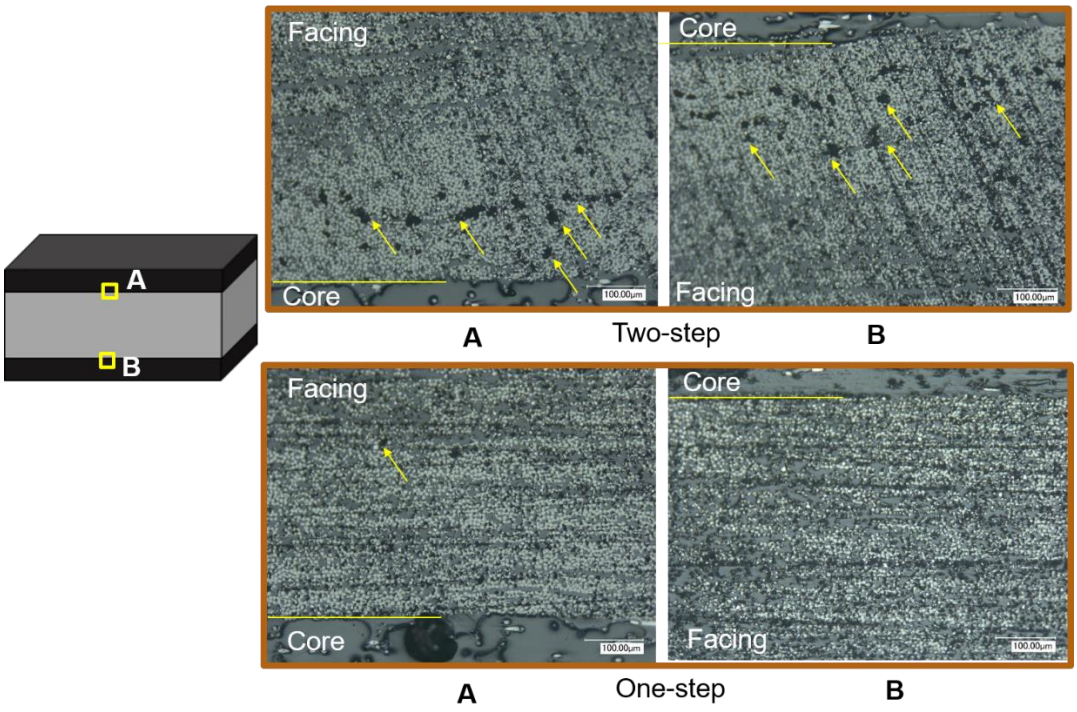

Figure 4-30 Side-view optical observation of the sandwiches with Two-step forming and One-step forming

4.3.3.3.2. The result of three-point bending test

Figure 4-31 and Figure 4-32 represent the typical stress-strain curves for 5mm-thick and 4-mm thick sandwich beams solicited in three point bending. The failure process of sandwich beams breaks up into three phases: the first phase shows initial linear elastic behavior which corresponds to the tension and compression of the facings and the first peak starts with the upper facing failure; the rest part of sandwich tends to suffer from core crushing and tension in the bottom facing where the second phase shows nonlinear behavior, which is followed by a phase of a reduction in the load applied where the bottom facing fails. Therefore, the sandwiches show ductile behavior under flexural failure.

It also can be seen that with higher core-to-facing thickness ratio, the curve can extend further, which indicates the core plays an important role in the energy absorption aspect.

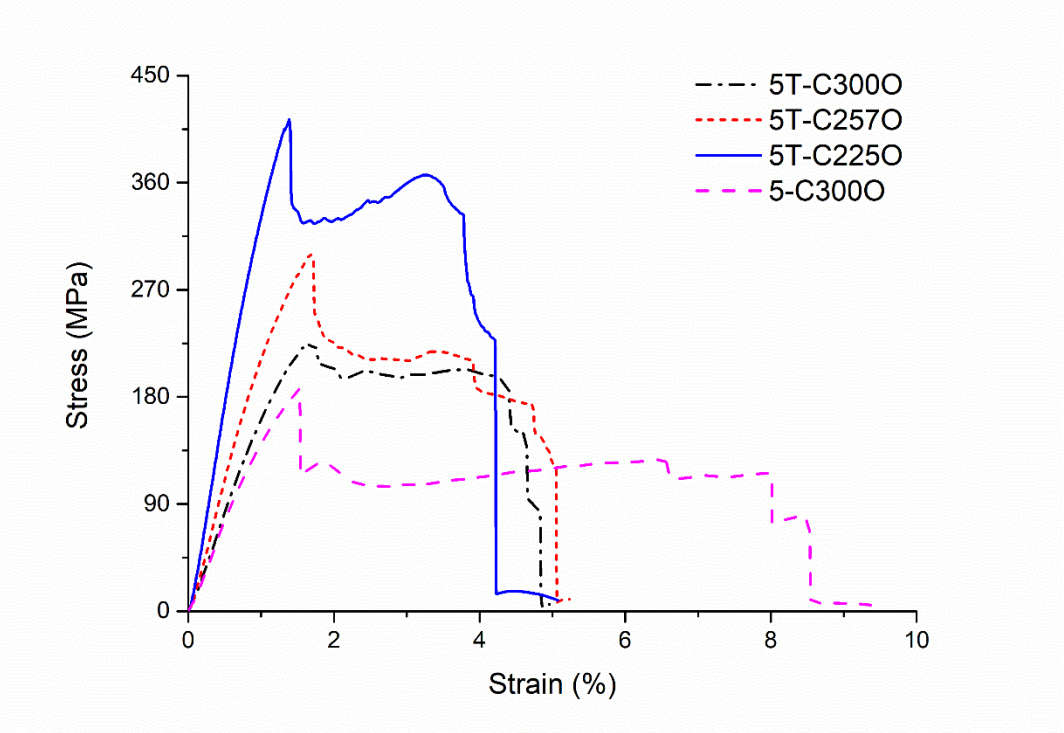

Figure 4-31 The flexural stress-strain curves of 5-mm thick sandwiches

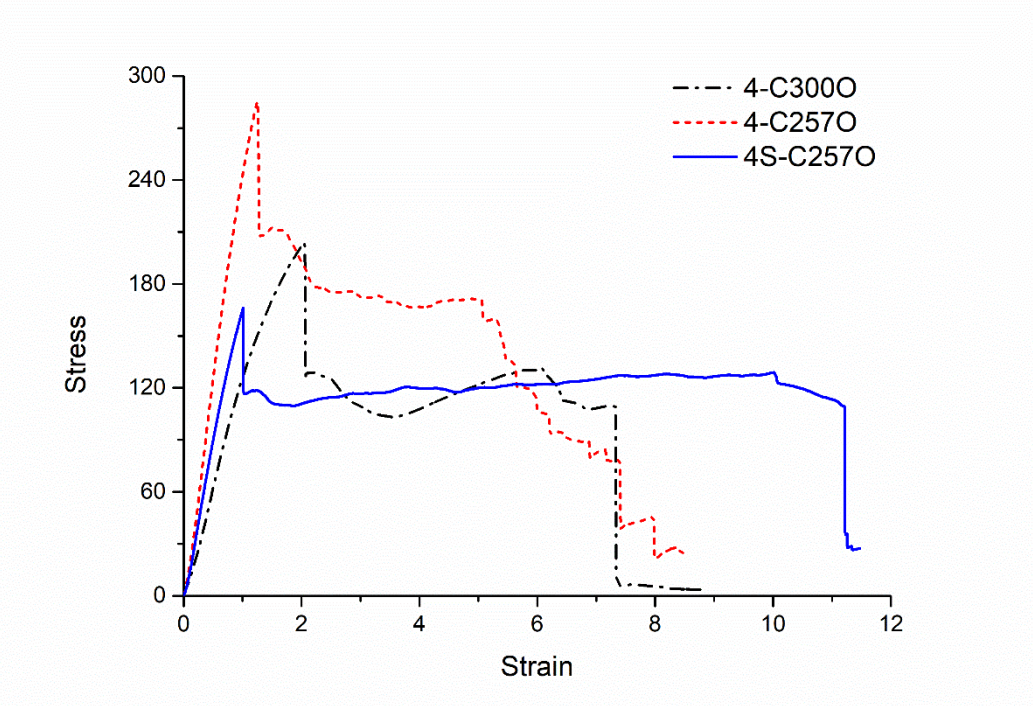

Figure 4-32 The flexural stress-strain curves of 4-mm thick sandwiches

There are two types of fracture modes in three-point bending test as shown in Figure 4-33. In general, top facing fails firstly, and then the end of fracture facing starts to thrust into the core part. But with SB3, core crushing and bottom facing fracture occur almost at the same time while with lower spring-back ratio, the end of fracture upper facing thrusts into core and causes inner delamination in core and finally the bottom facing fails.

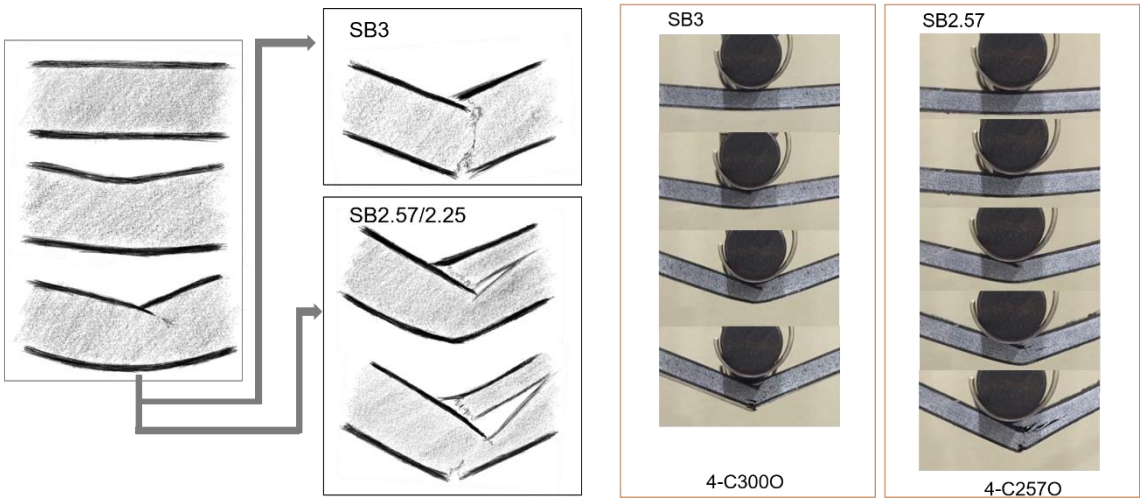

Figure 4-33 Failure mode of spring-backed core sandwich with different spring-back ratios

Figure 4-34 and Figure 4-35 show the flexural modulus and flexural rigidity of sandwiches. With the increase in the consolidation level where it means the decrease in spring-back ratio, both the flexural modulus and flexural rigidity increased.

Considering the sandwiches with the same thickness, in the case of SB3, by doubling the facing thickness, the rigidity did not improve a lot, while in the SB2.57 case, double the facing thickness, flexural rigidity show a large improvement. It is assumed the pressure provided by stress from the core is not enough for thicker facing compared with thin facing. So the property of core itself does not really affect the sandwich property. It is the spring-back ratio that determines the pressure it can offer to the facing and the facing property affect the sandwich.

It can be proved according to the standard ASTM C393 where the facing bending strength can be calculated as shown in Figure 4-36 and Figure 4-37, respectively. The sandwich 4S-C257O gets highest facing bending strength which is even higher than the sandwich 5T-C225O. That is

because the outer UD sheets of thicker facing was not able to get enough pressure by the released pressure from the core and it has more defects.

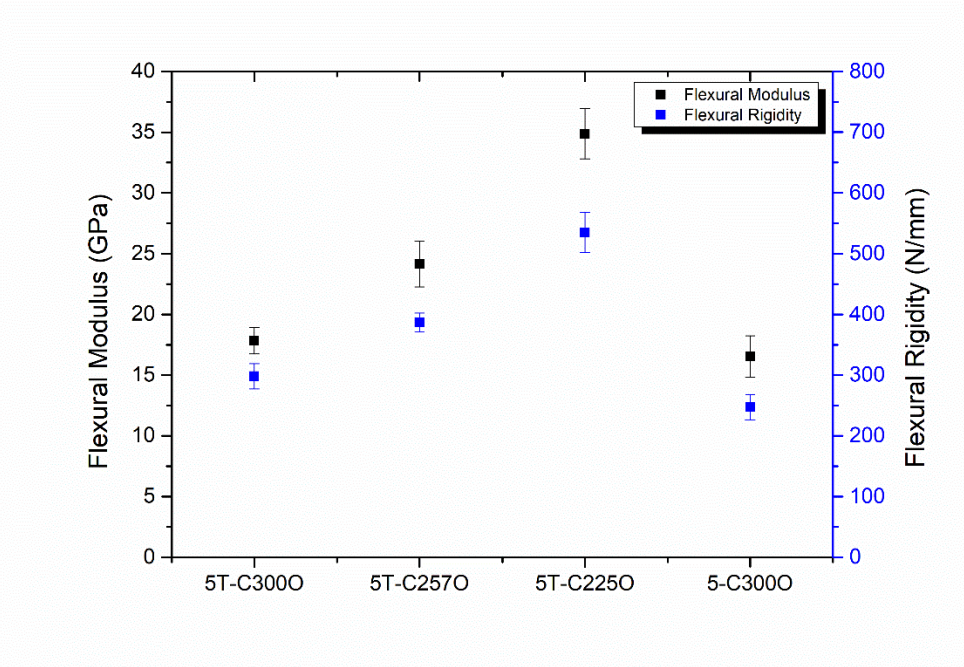

Figure 4-34 Flexural modulus and flexural rigidity of 5-mm thick sandwiches

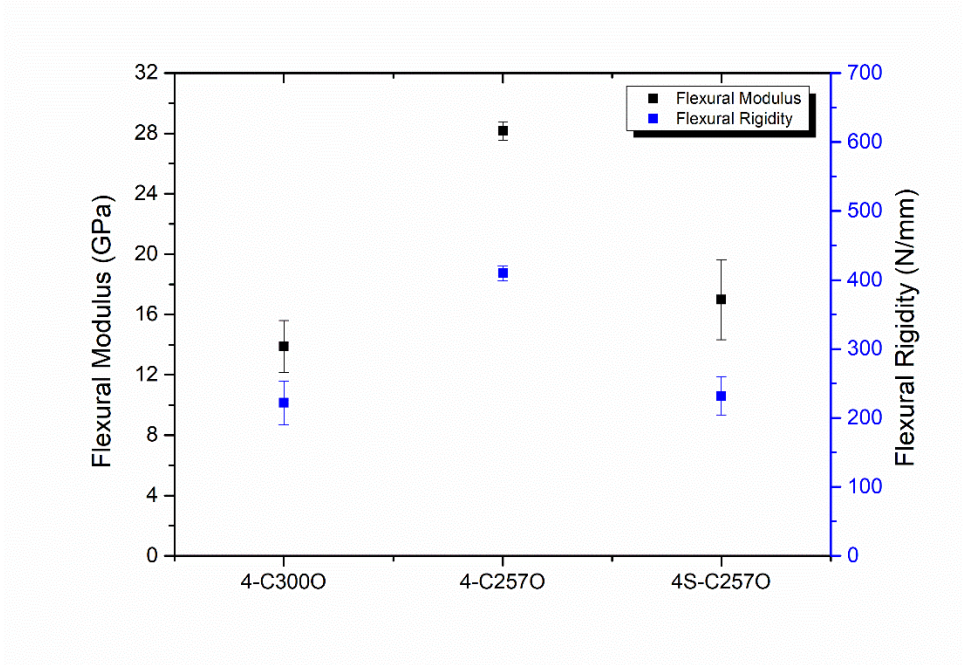

Figure 4-35 Flexural modulus and flexural rigidity of 4-mm thick sandwiches

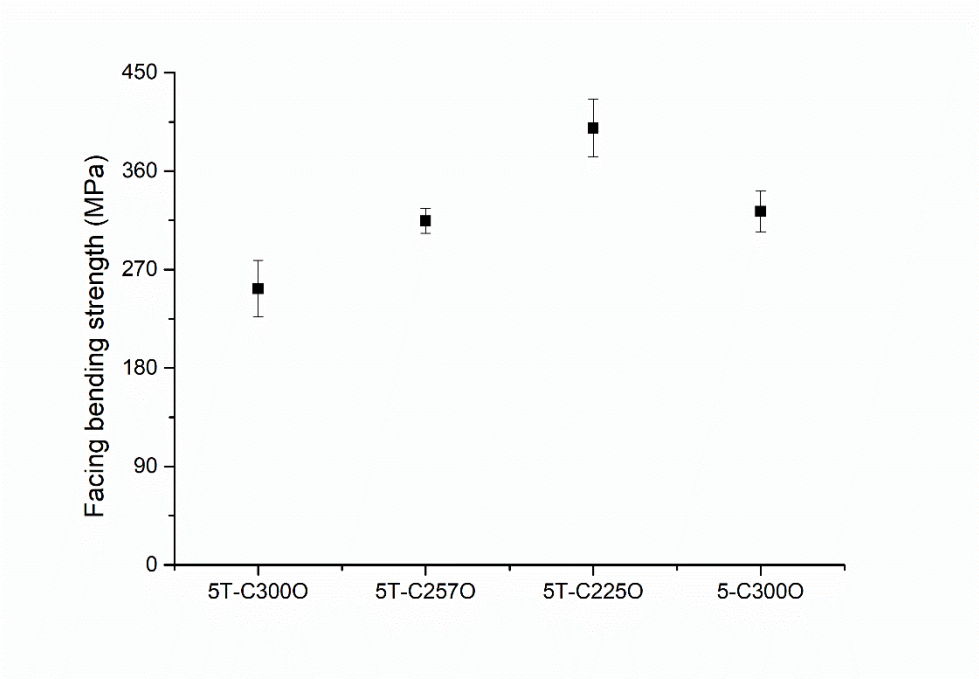

Figure 4-36 Facing bending strength of 5-mm thick sandwiches

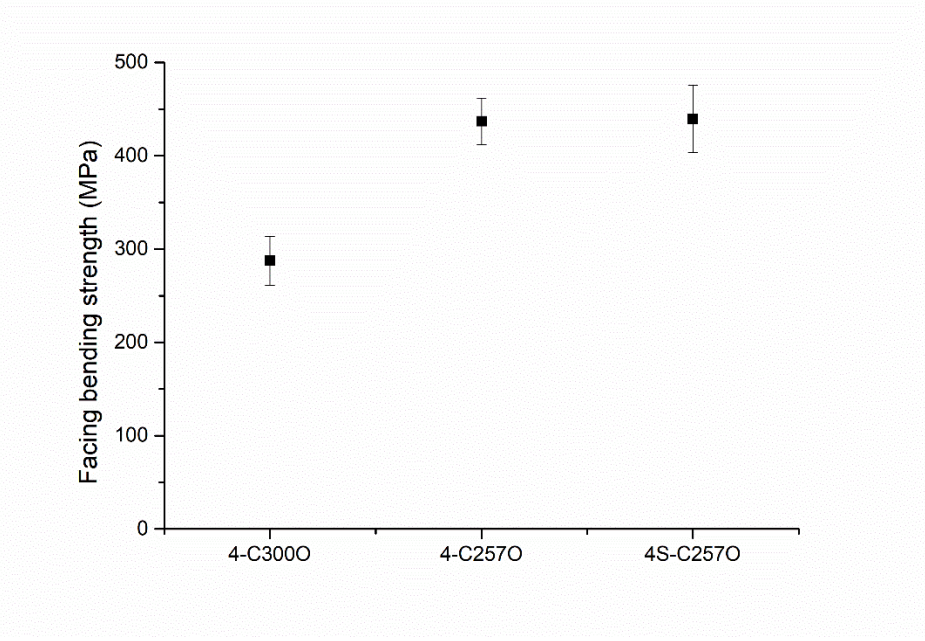

Figure 4-37 Facing bending strength of 4-mm thick sandwiches

Although the lower SB ratio is, the higher rigidity can be obtained, in the aspect of light weight or density, high SB ratio is not in an advantage, which can be seen from Table 4-8, density of sandwich is always lower than water when the SB is lower than 2.25.

Table 4-8 Density of the sandwiches

	Density [g/cm3]
5T-C300O	0.888
5T-C257O	0.927
5T-C225O	1.023
5-C300O	0.739
4-C300O	0.728
4-C257O	0.855
4S-C257O	0.742

4.3.3.3.3. The result of three-point impact test

From the impact load-displacement curves (Figure 4-38 and Figure 4-39), like the tendency in the static test, the extended phase can also be seen after the first peak. And for the sandwiches with higher core-to-facing thickness ratio, the curves can extend further.

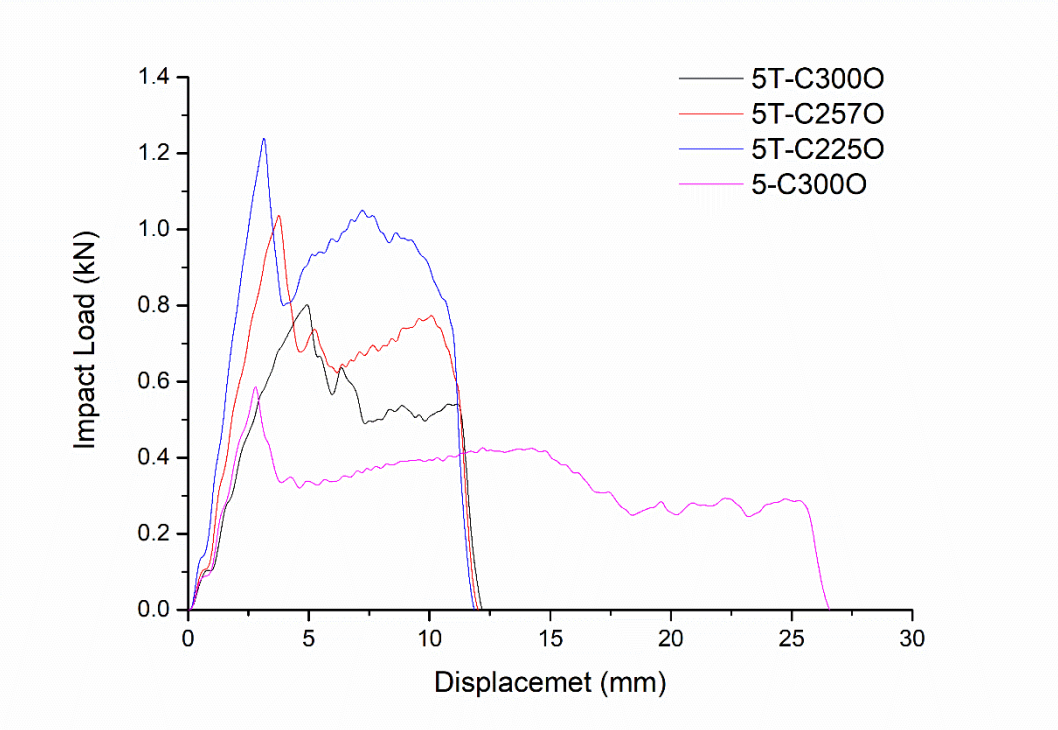

Figure 4-38 The impact load-displacement curves of 5-mm thick sandwiches

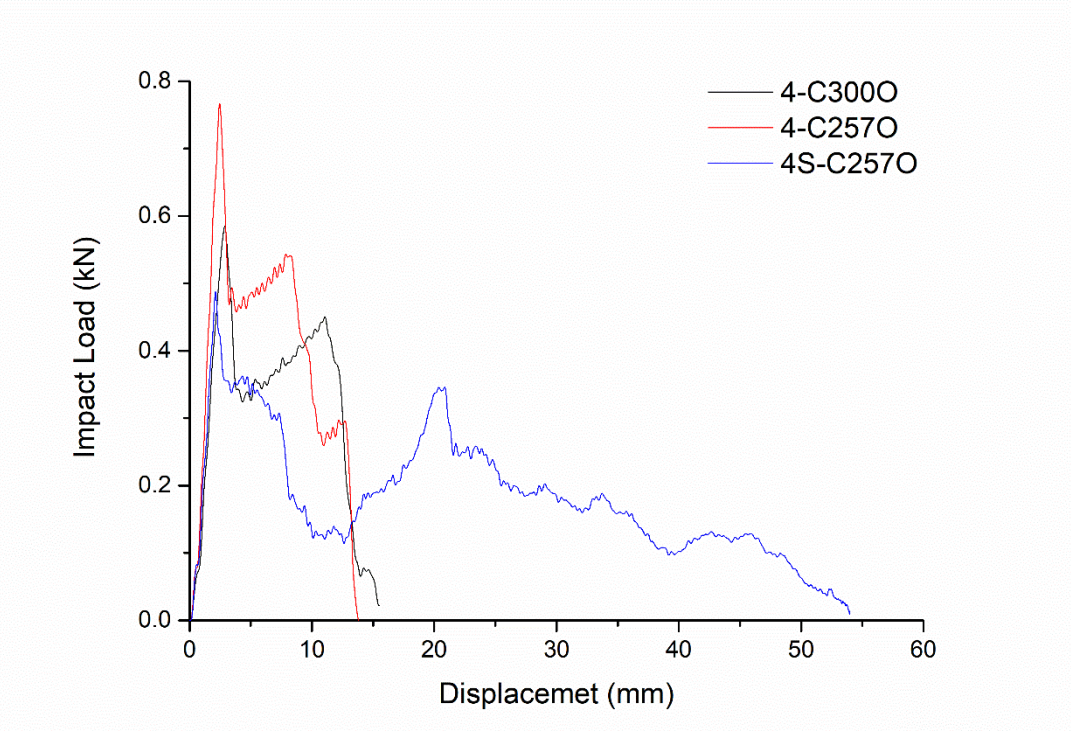

Figure 4-39 The impact load-displacement curves of 4-mm thick sandwiches

As for the fracture mode of three point impact test (Figure 4-40 and Figure 4-41), the two types of fracture modes were also observed by high speed camera records. The tendency is almost the same as static test where more porous or softer core does not contribute to inner delamination fracture. In addition, a higher core-to-facing thickness ratio can contribute to inner delamination of the core as well even at higher spring-back ratio, which can be seen in the sandwich, 5-C300O.

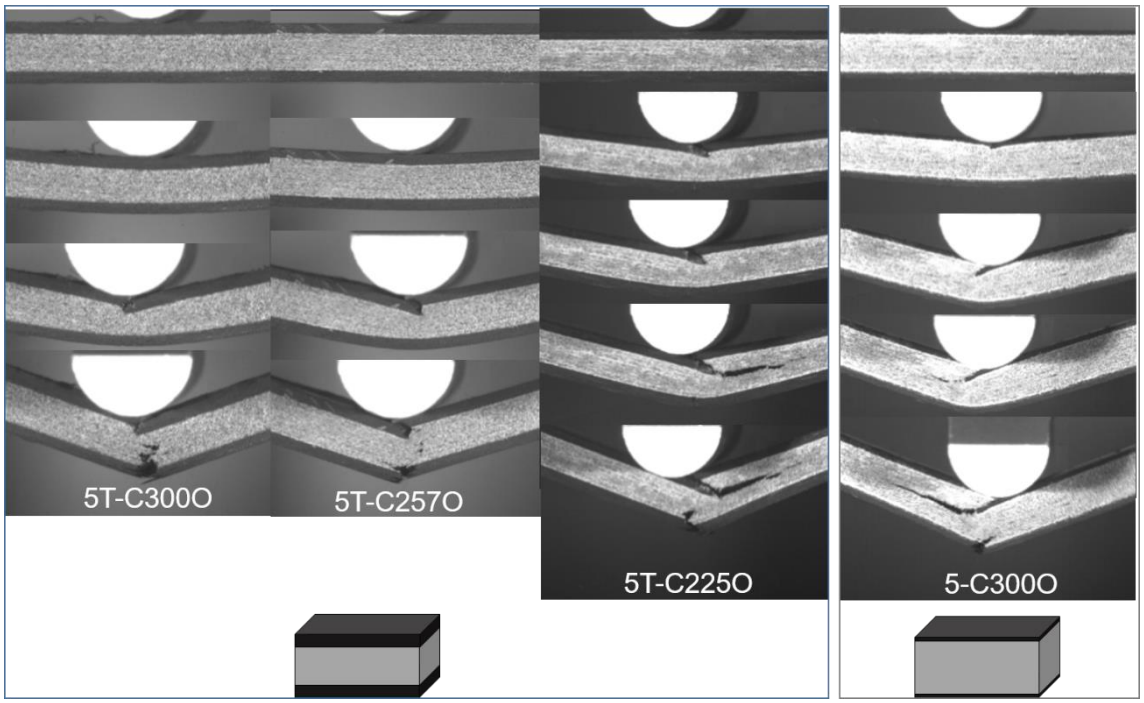

Figure 4-40 Failure mode in 3-point impact test of 5-mm thick sandwiches

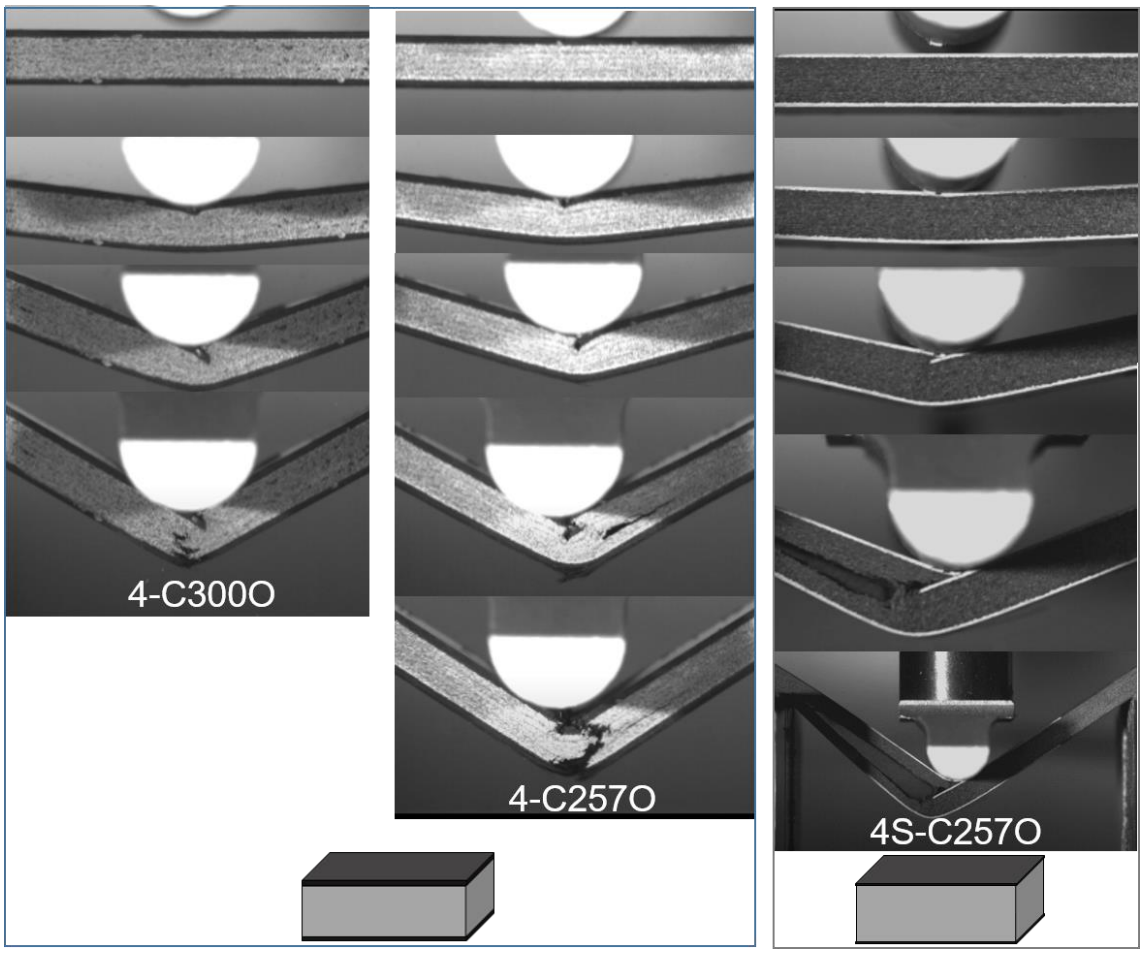

Figure 4-41 Failure mode in 3-point impact test of 4-mm thick sandwiches

In terms of the total energy absorption (Figure 4-42 and Figure 4-43), with the increase in SB, higher energy absorption capacity can be expected because of stronger facing which can contribute to elastic region of primary energy absorption. But the core-to-facing thickness ratio overweighs SB. In addition, more energy was absorbed in the fracture with delamination.

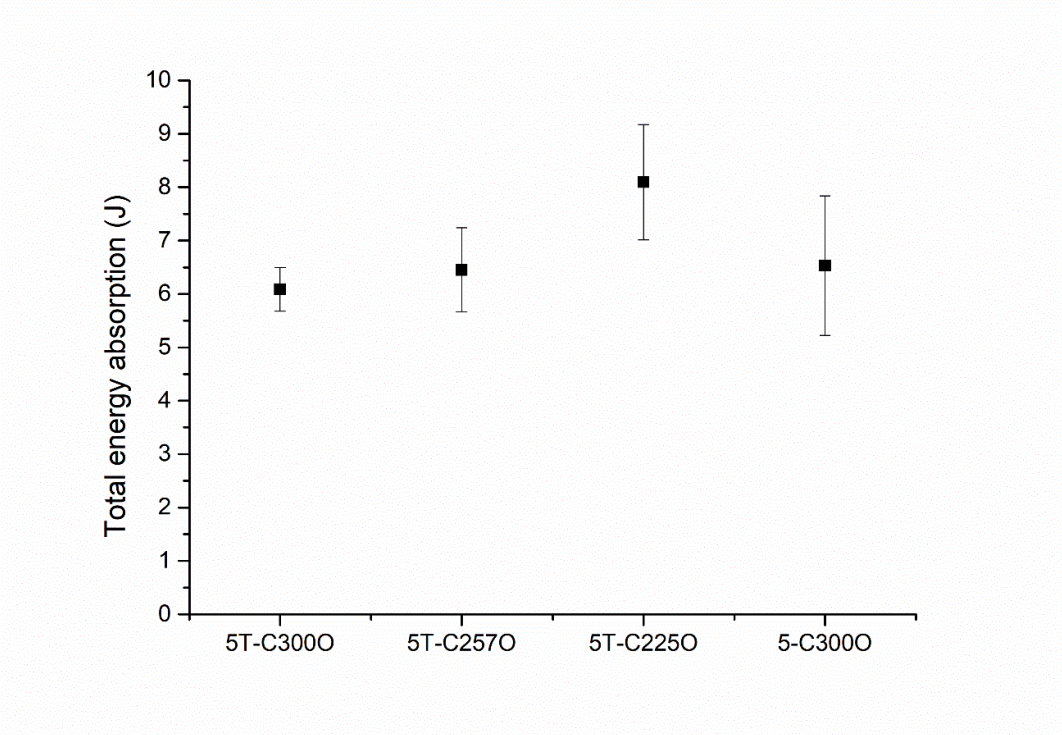

Figure 4-42 Total energy absorption of 5-mm thick sandwiches

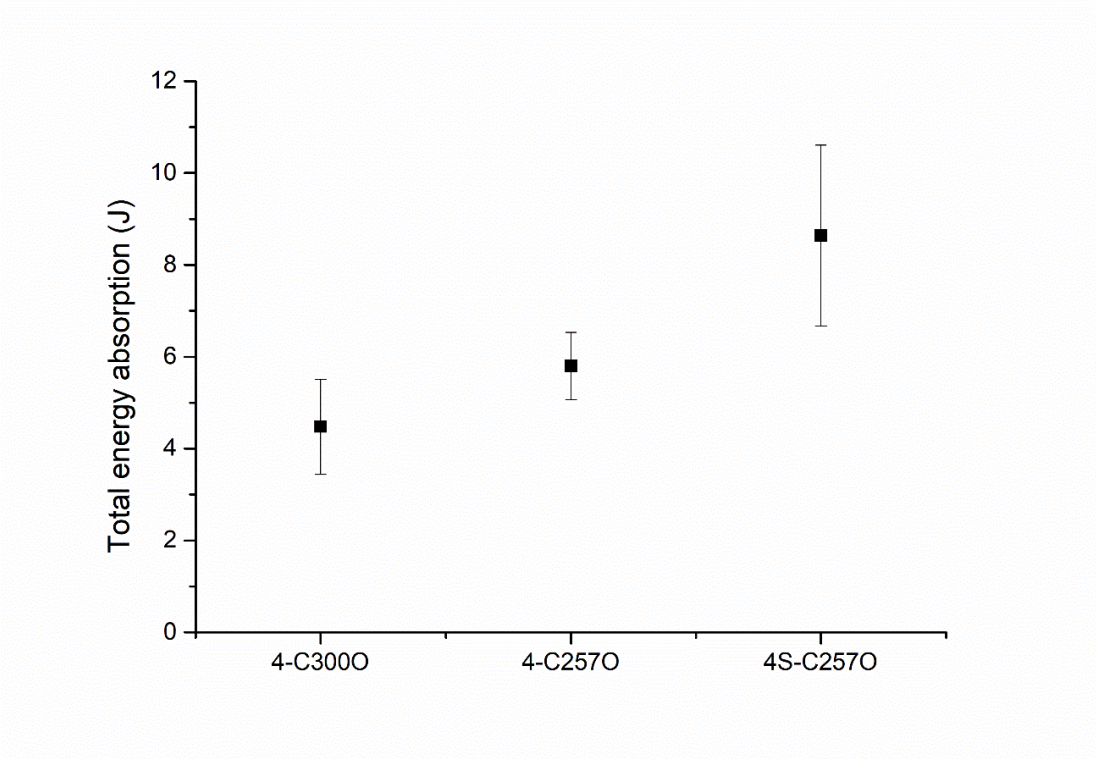

Figure 4-43 Total energy absorption of 4-mm thick sandwiches

Taking into account weight lighting aspect, the values of specific energy absorption (Figure 4-44 and Figure 4-45) were calculated using total energy absorption divided by density. It is obvious that the sandwiches with higher core-to-facing thickness ratio have higher specific energy absorption capacity.

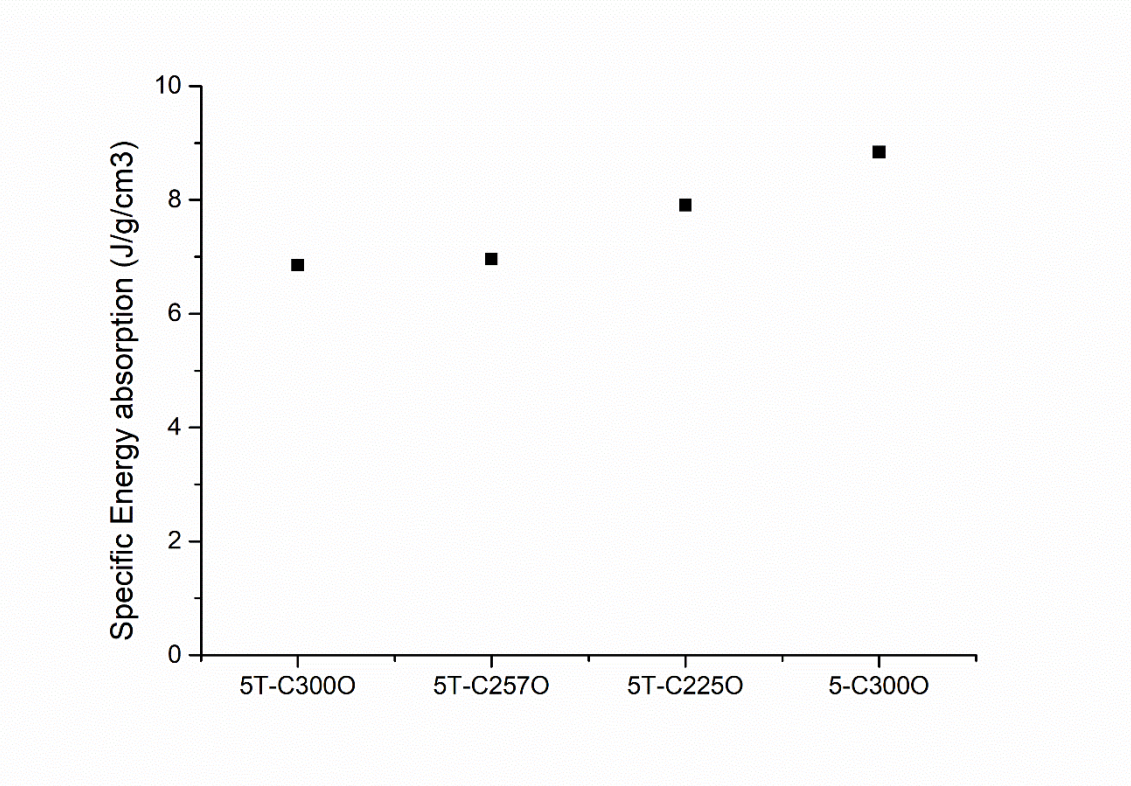

Figure 4-44 Specific energy absorption of 5-mm thick sandwiches

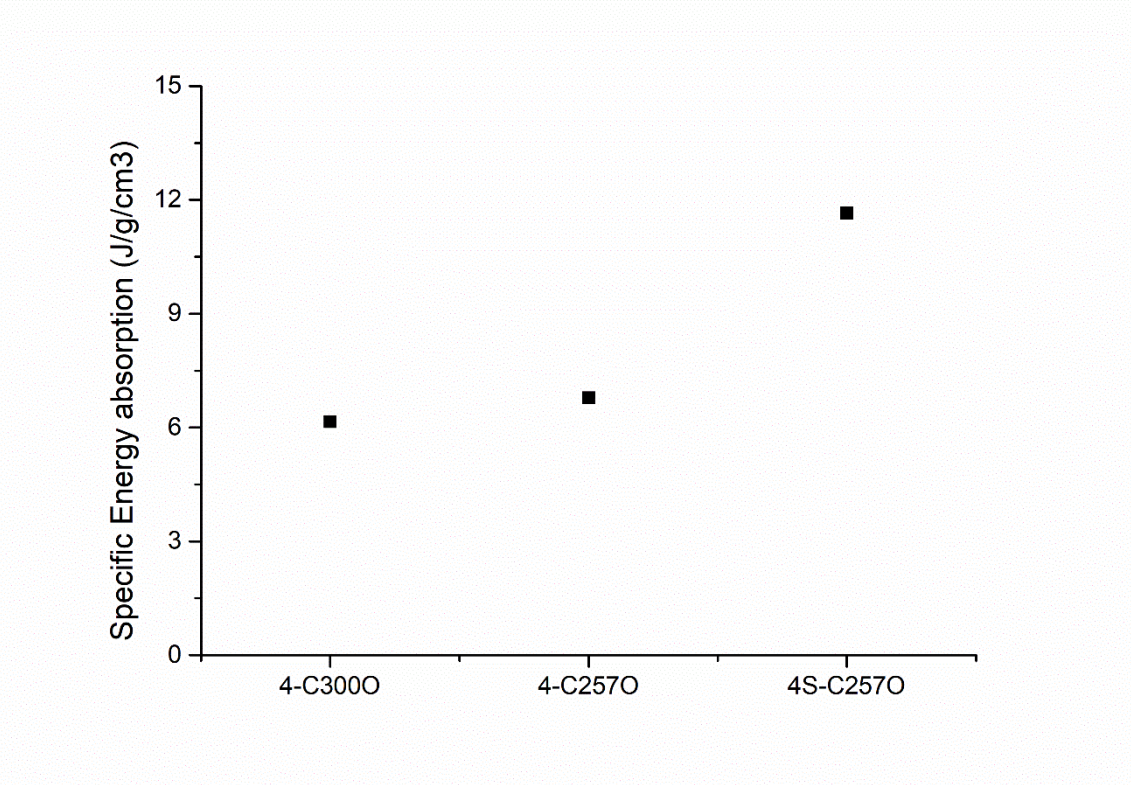

Figure 4-45 Specific energy absorption of 4-mm thick sandwiches

4.3.3.3.4. The comparison between spring-backed core sandwiches and foam-core sandwiches

Considering the practical engineering use aspect, the flexural property and energy absorption capacity of spring-backed sandwiches were compared with conventional foam-core sandwiches in which two types of commercial foam materials, type IG-51 and IG-71 (ROHACELL) were used.

From flexural test results as shown in Figure 4-46, Figure 4-47 and Figure 4-48, it is obvious that the flexural property of spring-backed sandwiches is superior to that of foam core sandwiches. But when it comes to light weight sector, material density has to be considered. Therefore, the aspect strength comparison among spring-backed sandwiches and foam core sandwiches is given in Figure 4-49. Even though foam material is usually considered to be in the ascendant for its lightweight, the aspect strength of spring-backed sandwich still shows close to and even higher than foam-core sandwiches.

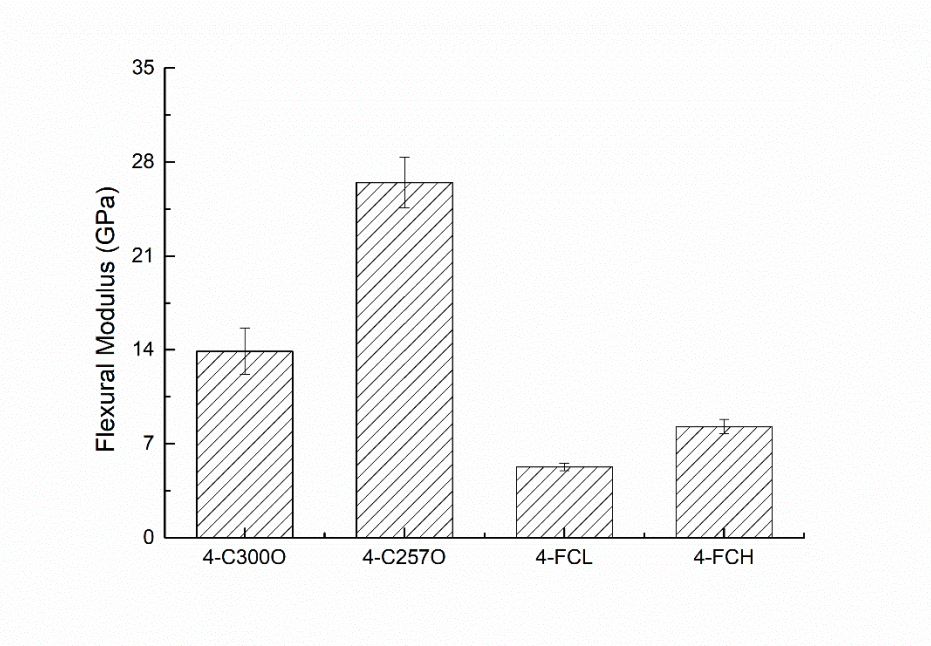

Figure 4-46 The flexural modulus comparison between spring-backed core sandwiches and foam-core sandwiches

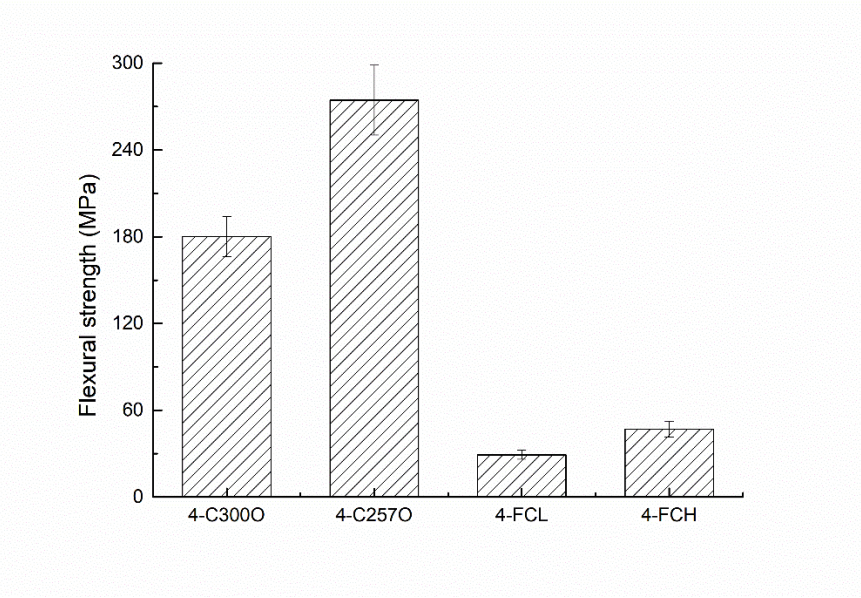

Figure 4-47 The flexural strength comparison between spring-backed core sandwiches and foam-core sandwiches

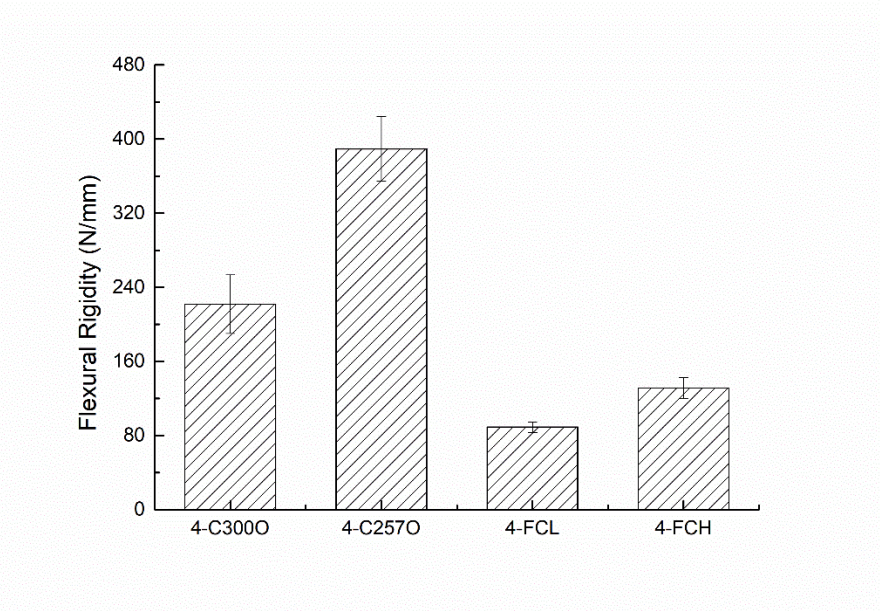

Figure 4-48 The flexural rigidity comparison between spring-backed core sandwiches and foam-core sandwiches

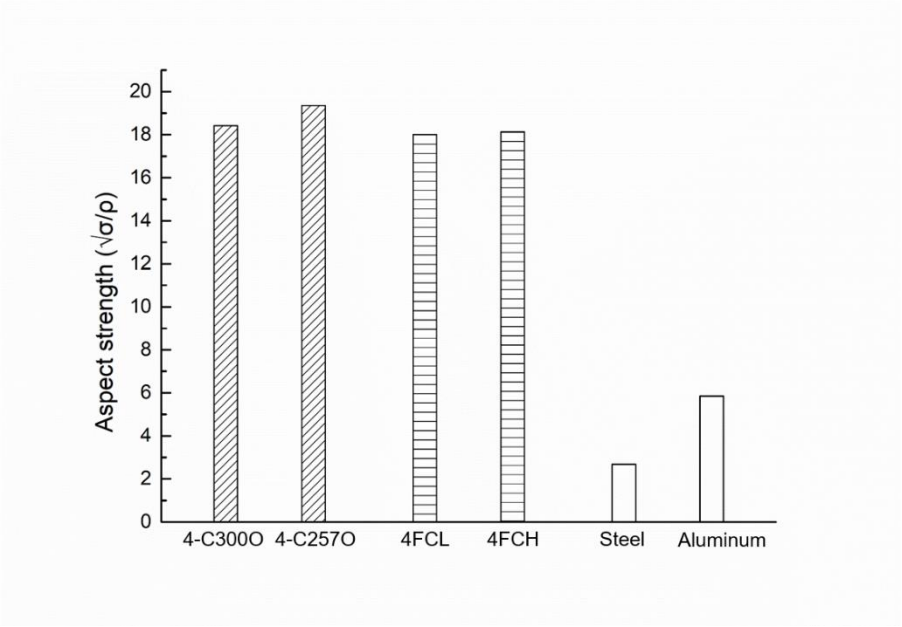

Figure 4-49 The aspect strength comparison between spring-backed core sandwiches and foam-core sandwiches

Figure 4-50 shows the normalized specific energy absorption comparison between spring-backed sandwiches and foam-core sandwiches. The value of spring-backed sandwich can be double or even higher than that of relatively high density foam-core sandwich. It can be seen from the failure

mode (Figure 4-51) that the foam core failed at the very early stage accompanied with facing/core detaching, on account of which, the facing made almost no contribution to the impact strength. Therefore, it can also be concluded that the spring-backed core sandwich has adequate facing/core adhesive property.

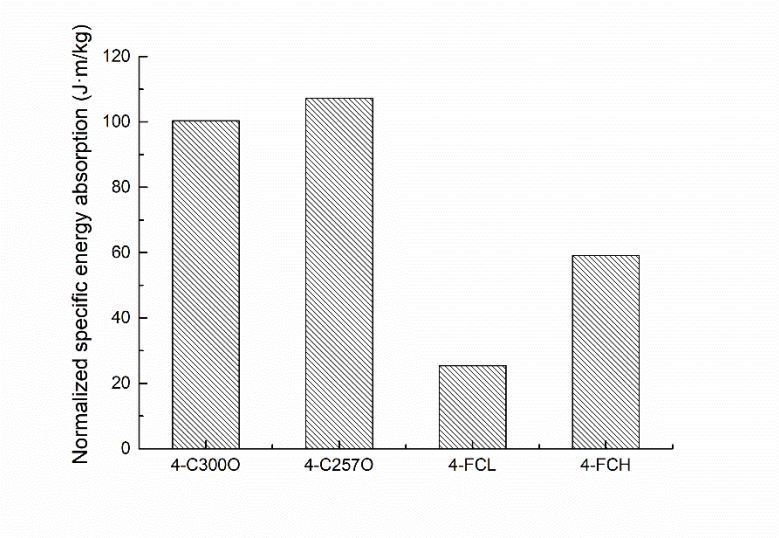

Figure 4-50 The normalize specific energy absorption comparison between spring-backed core sandwiches and foam-core sandwiches

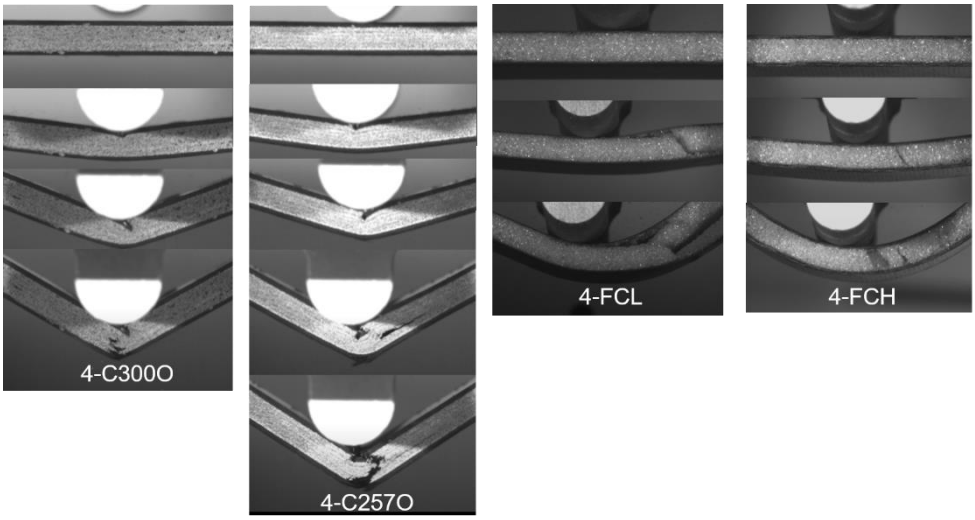

Figure 4-51 Comparison of failure mode in 3-point impact test between spring-backed core sandwiches and foam core sandwiches

4.3.3.4. Conclusion

From the experiments and results analysis, the release of the internal stress is regarded as the main mechanism of the spring-back effect and it contributes to the consolidation of the facing. And the spring-backed CPT-PA6 core sandwich is superior to foam core sandwich in terms of flexural property and energy absorption. Moreover, one-step forming process for CPT core sandwich can be considered as an efficient and reliable method when the core is designed to a suitable deconsolidation level.

4.4. Summary

In this chapter, spring-back CPT was adopted as core material in sandwich structure and was successfully made.

In the case of spring-back CPT-PP core/ CTT-PA6 facing sandwich, CPT-PA6 adhesive and needle punching were proved to improve the adhesion between facing/core and enhance both rigidity and interlaminar shear property of the sandwich.

Spring-back CPT-PA6 core/ UD facing sandwiches were manufactured with separate method, two-step method and one-step method successfully. From the experiments and results analysis, the release of the internal stress is regarded as the main mechanism of the spring-back effect and it contributes to the consolidation of the facing. And the spring-backed CPT-PA6 core sandwich shows superior to foam core sandwich in terms of flexural property and energy absorption. Moreover, one-step forming process for CPT core sandwich can be considered as an efficient and reliable method when the core is designed to a suitable deconsolidation level.

For developing this kind of sandwich, it is necessary to design optimal facing thickness and spring ratio of the core to achieve balance between high production efficiency and promising mechanical performance.

5. Conclusions

Thanks to CFRP's high mechanical performance and low weight, other than being used in aerospace and automotive industries, it starts to serve an array of other fields varying from wind turbines and satellites to drones and sports goods. A further positive development ranging from 10-13% is expected in the near future.

Undoubtedly, the increasing in CF or CFRP demand leads to a collateral increasing flow of waste. Basically, there are two main sources of waste containing CF. One is dry waste residues such as uncured and expired prepreg waste during production with manufacturers. The other source come from the product nearing the end of their life cycles. The wastage of CFRP keeps increasing along with its demand, for which an increasing number of researchers has been working on fiber recycling subject, thus there has been beneficial recycling techniques for CF available to maintain the mechanical properties of rCF.

However, the CFRP lifecycle loop needs to be closed since rCF should be repurposed for another round of composite application.

For those in-plant CF waste, most of them are uncontaminated and in relatively good condition. The composition is distinguishable as well. Therefore, recycling of in-plant CF waste could be subjected to less shredding of CF and the reclaimed CF can be of near virgin quality and less length sacrifice. But it is difficult to maintain fiber alignment status due to matrix detaching process before reusing, thus, to improve the fiber alignment of those relatively long (or what we called semi-long in this study) CF, a productive and achievable fiber aligning system was introduced to bring out the better performance in rCFRP.

As for the small portion of contaminated or unidentifiable mixed in-plant CF waste and most of market CF waste, the recycling involves a series of breaking-down processes, such as shredding, crushing, milling etc. Therefore the reusing of rCF from that could be limited by its drawbacks like extremely short fiber length and inferior quality, for which the re-manufacturing product with that rCF could have relative low mechanical performance and even some serious problems. With the aim at resolving the problems in short rCFRTP material, the concepts of whole CF sandwich and fiber hybridization were applied and investigated.

5.1. A carding and stretching system for semi-long rCF alignment

When relatively long rCF, around 50 mm in this thesis, can be obtained from recycling, exploiting its potential for high mechanical performance would be priority.

Through the development of a carding and stretching method to obtain a promising fiber alignment for rCF, the following conclusions can be drawn.

The carding process was used as the primary step to arrange thoroughly opened rCF and mix them with resin fibers uniformly. The stretching process was applied as a supplement to realign rCF. Using this method, CWT with a V_f of 43% without harmful void can be achieved. Satisfactory mechanical properties were obtained in some stretched types of CWT, and their tensile properties are close to those of unidirectional CF tape reinforced thermoplastics, and the flexural strength of some stretched CWT can be even higher than that of continuous woven CF fabric reinforced thermosetting plastic. An optimal CWT with a V_f of 30% and stretching ratio of 30% was proved. After X-ray micro-CT scanning, using an image processing and statistical analysis method, fiber alignment level was observed through FOD, and it was found that most rCF were aligned within ± 15°. At the end, two analytical models were applied to predict elastic moduli. Both laminate and netting theories show good correlation with experimental results, and netting theory was proven to be a simple tool for approximating CWT material.

5.2. Problems in re-manufacturing rCFRP with short rCF and the solutions

When the length of rCF tends to be short within 10 mm, usually they would be uniformly dispersed in the plane by nonwoven technology or paper-making technology. But due to short fiber length and random fiber orientation, high mechanical property cannot be expected compared with CWT. Therefore, to solve its weaknesses and find its potential in industry are necessary.

5.2.1. Brittle fracture of short rCF reinforced thermoplastic and its improvement

Brittle fracture is the worse type of failure because it occurs suddenly without warning and the material exhibits no visible signs of damage. In discontinuous fiber reinforced systems, it would lead to local stress concentrations for those irregular shaped particles or short fibers, which can affect the matrix microstructure, the properties and crack path. Therefore, due to large number of fiber ends and misalignment, inner defects and voids would increase stress concentration and creates more crack propagation paths, randomly oriented short carbon fiber reinforced plastics tend to be more brittle.

In this thesis, discontinuous aramid fiber papers were applied to hybridize with discontinuous carbon fiber papers and reinforce with thermoplastic. Flexural and energy absorption behavior were investigated among the hybrid panels with various interlayer stacking sequence, fiber dispersion state and different aramid fiber lengths.

In general, hybridized carbon fiber/aramid fiber paper reinforced thermoplastics have positive hybrid effect. “carbon outside” hybrids not only shows higher flexural property but also displays stage-like fracture. The effect of “fracture stopper” performed by aramid paper layers are more apparent in “Carbon outside” hybrids. In the case of interlaminated hybrid, hybrid reinforcement takes better effect when the segments setting numbers are lesser. Fiber length effect is not apparent in static loading, hybrid with longer aramid fiber obtain larger energy absorption capacity. Interlaminate structure of hybrid overwhelmed intermingled hybrid because it has a comprehensively better performance in terms of energy absorption capacity thanks to its stage-

like failure process. For developing this kind of hybrids, it is necessary to optimize the structure more precisely. Further analytical and numerical discussion is required in future work.

5.2.2. Deconsolidation of short rCF reinforced thermoplastic and its application

CPT under post-thermoforming would produce deconsolidation, which demonstrates the so-called spring-back effect. During processing, stress can be introduced into the material via various mechanisms, which can result in a low quality part. In some case, release of the internal stresses during post-processing thermal treatments can result in an excessive void content, which can render the part useless. However, this production of voids in CPT can be used to produce a porous and lightweight core material to reduce the density of the composite and absorb impact energy, vibrations, compressive stress, and acoustical shock. Therefore, it was considered to be a suitable core in sandwich structure.

In this thesis, spring-back CPT was adopted as core material in sandwich structure and was successfully made.

In the case of spring-back CPT-PP core/ CTT-PA6 facing sandwich, CPT-PA6 adhesive and needle punching were proved to improve the adhesion between facing/core and enhance both rigidity and interlaminar shear property of the sandwich.

Spring-back CPT-PA6 core/ UD facing sandwiches were manufactured with separate method, two-step method and one-step method successfully. From the experiments and results analysis, the release of the internal stress is regarded as the main mechanism of the spring-back effect and it contributes to the consolidation of the facing. And the spring-backed CPT-PA6 core sandwich is superior to foam core sandwich in terms of flexural property and energy absorption. Moreover, one-step forming process for CPT core sandwich can be considered as an efficient and reliable method when the core is designed to a suitable deconsolidation level.

For developing this kind of sandwich, it is necessary to design optimal facing thickness and spring-back ratio of the core to achieve balance between high production efficiency and promising mechanical performance.

5.3. Achievements

The achievements of this thesis are as followings:

- A carding and stretching process was developed to align semi-long rCF. And it was proved to be a promising method to scale up in industry for not only improving fiber alignment level but attaining satisfactory mechanical properties.
- Netting analysis was proved to be a simple method for approximating CWT material and can be used as a quick sizing tool for industries.
- Fatal brittleness problem of CPT was solved by hybridizing with aramid fibers. And an optimal stacking sequence was found without sacrificing mechanical property. The energy absorption ability of the hybrid has reached around 4 times higher than pure CPT.
- The study proved interlaminate structure of hybrid overwhelmed intermingled hybrid because it has a comprehensively better performance.
- A sandwich with whole CFRTP was investigated and optimized where spring-back CPT was used as core.
- Fast manufacturing method for spring-back CPT sandwich was discovered. The sandwich has excellent specific mechanical property where its density can be even lower than water. With the high specific property and floatable feature, it has potential to expand its application in industry.

5.4. Outlook

With the booming development of artificial intelligence, electrification and sharing economy, except the concepts of lightweight, durability and design, repairable, recyclable and reusable material is expected widespread to adapt to modern society and sustainable development.

Given that CF product shows its superior performance in modern society, rCFRP also has its appealing not only for its potential to be next-generation material but also for environmental friendly aspect, which is one of major concerns among the world.

Currently, to manage the in-plant rCF, a carding and stretching system was developed to improve fiber alignment of semi-long CF in rCFRP and a satisfactory mechanical property was achieved.

In addition, the netting analysis was proved to be a quick sizing tool for industry since it met well with empirical result. Further adjustment of fiber feeding, pin direction and rotation speed etc. is an essential future task to improve fiber alignment. Also, accurate analytical and numerical analysis are necessary to obtain deep understanding of CWT.

Concerning short rCF from market CF waste, spring-backed CPT core and fiber hybridization were introduced to solve the existing problems in random orientated short CFRTP. The new designed whole CF body sandwich can be an alternative material with satisfactory stiffness-to-weight ratio and the manufacturing method for this kind of sandwich shows extreme high production efficiency compared with conventional methods. For this research, an in-depth understanding of spring-back mechanism and the release stress investigation is necessary in the near future. When hybridized with ductile aramid fibers, CPT has large improvement in toughness related to energy absorption factor where aramid fiber layer served as crack arrester and slow down the crack propagation. In addition, it can be a win-win solution since aramid fiber recycling is also demanded. But the stacking sequence and fiber length effect on hybrids need more efforts in analyzing to build a map of hybrid effect on short CFRTP system to help manufacturers.

To sum up, this thesis offered valuable and efficient solutions for re-manufacturing carbon fiber sheet reinforced thermoplastics using rCF under semi-long and short status, which covers the general concerns of both in-plant and market CF waste. The work also demonstrates that comprehensive and insightful experimental and theoretical studies are needed to obtain better understanding of them and a complete recycling system or map available for a variety of rCF conditions should also be developed to close the recycling loop to the maximum extent possible.

Appendix. Digital filtering method

Digital filtering was used to suppress signal distortion induced by impactor ringing, which is a well-known and inevitable problem in impact tests. The equations of the digital low-pass filter which is applied to the data are as follows:

$$y(n) = a_0 x(n) + a_1 x(n-1) + a_2 x(n-2) - b_1 y(n-1) - b_2 y(n-2)$$

$$\begin{cases} a_0 = a_2 = \dfrac{(\omega_a T)^2}{4 + 2\sqrt{2}\omega_a T + (\omega_a T)^2} \\ a_1 = \dfrac{2(\omega_a T)^2}{4 + 2\sqrt{2}\omega_a T + (\omega_a T)^2} = 2a_0 \\ b_1 = \dfrac{-8 + 2(\omega_a T)^2}{4 + 2\sqrt{2}\omega_a T + (\omega_a T)^2} \\ b_2 = \dfrac{4 - 2\sqrt{2}\omega_a T + (\omega_a T)^2}{4 + 2\sqrt{2}\omega_a T + (\omega_a T)^2} \end{cases}$$

$$\omega_a = \frac{2}{T \tan(2\pi f_d T / 2)}$$

Here, x(n) is input force signal, y(n) is output force signal, T is sampling interval, f_d is cut-off digital frequency.

After digital filtering, the raw and filtered load-time and load-displacement curves of two samples from 3-point impact on the hybrid and the sandwich at the velocity of 3.8 m/s are as follows:

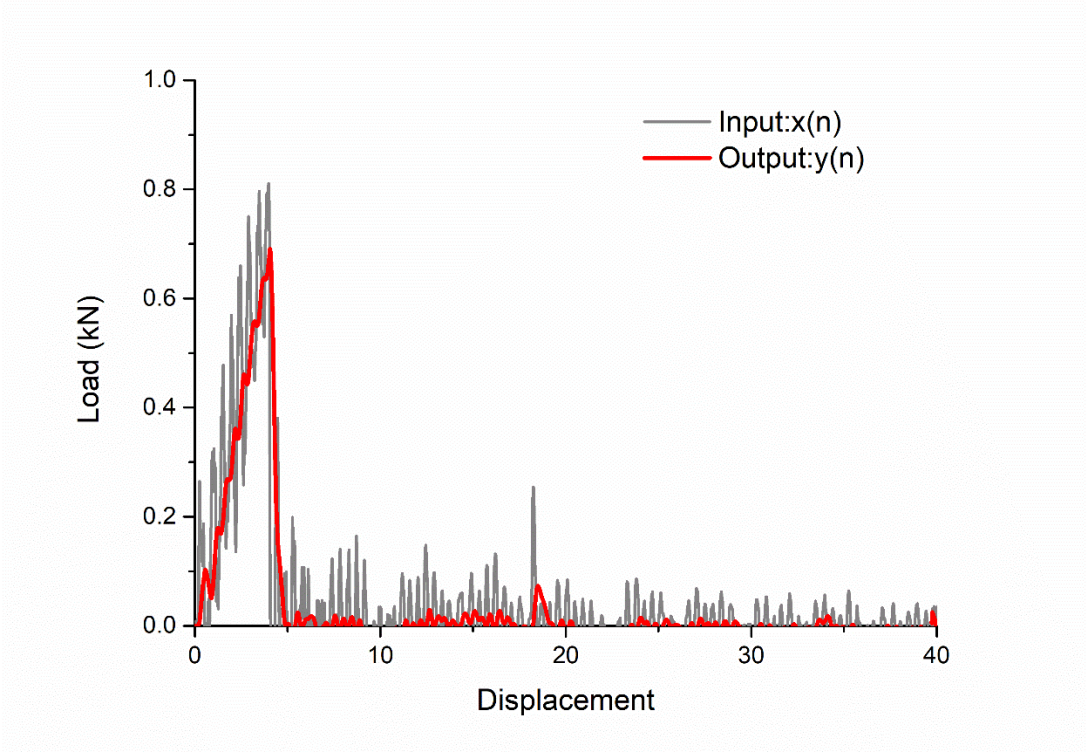
Input:x(n)
Output:y(n)
Load (kN)
Displacement
1.0
0.8
0.6
0.4
0.2
0.0
0
10
20
30
40

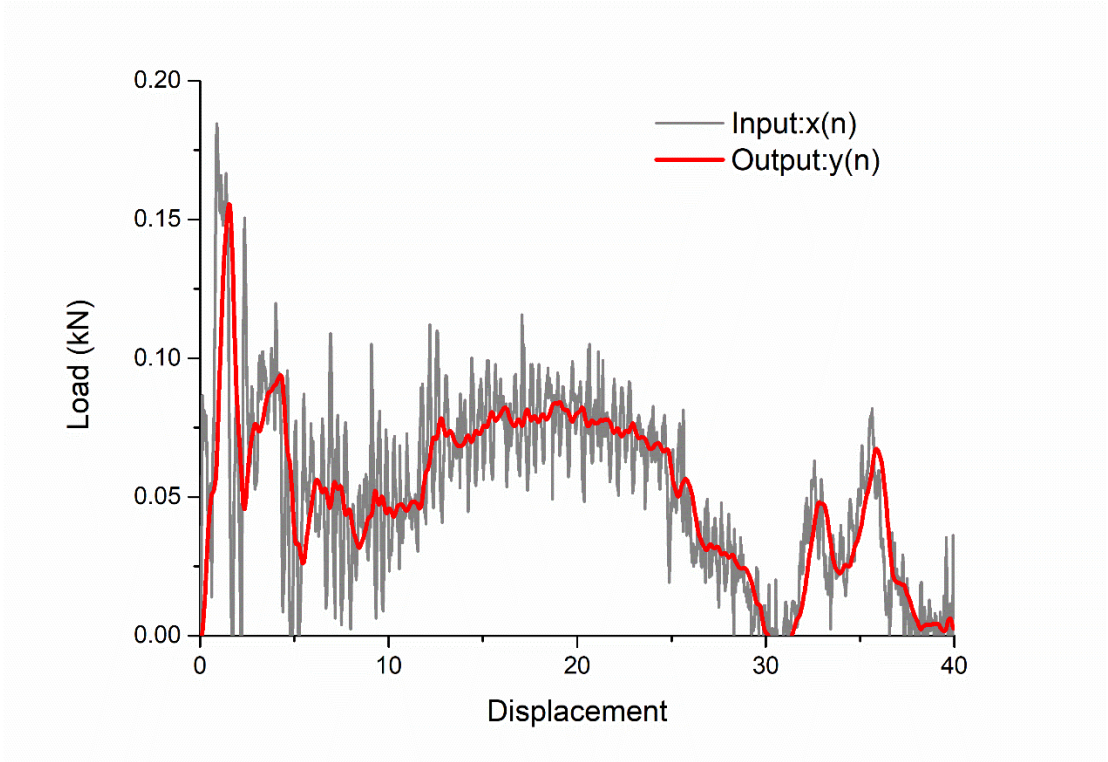
Input:x(n)
Output:y(n)
Load (kN)
Displacement
0.20
0.15
0.10
0.05
0.00
0
10
20
30
40

References

[1] Donnet, J.-B. and R.C. Bansal, *Carbon fibers*. 1998: Crc Press.

[2] Das, S., et al., *Global Carbon Fiber Composites Supply Chain Competitiveness Analysis*. 2016: United States.

[3] *Growth Opportunities in the Global Carbon Fiber Market*. 2018; Available from: https://www.lucintel.com/global-carbon-fiber-market-2018.aspx.

[4] Witten, E., V. Mathes, M. Sauer and M. Kühnel, *Composites Market Report 2018*. 2018, AVK-Industrievereinigung Verstärkte Kunststoffe e.V. [Federation of Reinforced Plastics].

[5] Meng, F., J. McKechnie, and S.J. Pickering, *An assessment of financial viability of recycled carbon fibre in automotive applications.* Composites Part A: Applied Science and Manufacturing, 2018. **109**: p. 207-220.

[6] McConnell, V.P., *Launching the carbon fibre recycling industry*. Reinforced Plastics, 2010. **54**(2): p. 33-37.

[7] Melendi-Espina, S., et al., *Recycling of carbon fibre composites*. 2016.

[8] Witik, R.A., et al., *Carbon fibre reinforced composite waste: An environmental assessment of recycling, energy recovery and landfilling.* Composites Part A: Applied Science and Manufacturing, 2013. **49**: p. 89-99.

[9] *Boom time for carbon fibre recycling*. 2016; Available from: http://terratechmedia.com/boomtime/.

[10] Pickering, S.J., *Recycling technologies for thermoset composite materials—current status.* Composites Part A: Applied Science and Manufacturing, 2006. **37**(8): p. 1206-1215.

[11] Pimenta, S. and S.T. Pinho, *Recycling carbon fibre reinforced polymers for structural applications: Technology review and market outlook.* Waste Management, 2011. **31**(2): p. 378-392.

[12] Jiang, G., et al., *Characterisation of carbon fibres recycled from carbon fibre/epoxy resin composites using supercritical n-propanol.* Composites Science and Technology, 2009. **69**(2): p. 192-198.

[13] Cai, G., et al., *Influence of treatment with superheated steam on tensile properties of carbon fiber*. Composites Part A: Applied Science and Manufacturing, 2018. **107**: p. 555-560.

[14] Wan, Y. and J. Takahashi, *Tensile and compressive properties of chopped carbon fiber tapes reinforced thermoplastics with different fiber lengths and molding pressures.* Composites Part A: Applied Science and Manufacturing, 2016. **87**: p. 271-281.

[15] Yamashita, S., et al., *Volume resistivity of ultra-thin chopped carbon fiber tape reinforced thermoplastics.* Composites Part A: Applied Science and Manufacturing, 2016. **90**: p. 598-605.

[16] Gillet, A., O. Mantaux, and G. Cazaurang, *Characterization of composite materials made from discontinuous carbon fibres within the framework of composite recycling.* Composites Part A: Applied Science and Manufacturing, 2015. **75**: p. 89-95.

[17] Adam, H., *Carbon fibre in automotive applications.* Materials & Design, 1997. **18**(4): p. 349-355.

[18] Such, M., C. Ward, and K. Potter, *Aligned discontinuous fibre composites: a short history.* Journal of Multifunctional Composites, 2014. **2**(3): p. 155-68.

[19] van de Werken, N., et al., *Investigating the effects of fiber surface treatment and alignment on mechanical properties of recycled carbon fiber composites.* Composites Part A: Applied Science and Manufacturing, 2019. **119**: p. 38-47.

[20] Yu, H., K.D. Potter, and M.R. Wisnom, *A novel manufacturing method for aligned discontinuous fibre composites (High Performance-Discontinuous Fibre method).* Composites Part A: Applied Science and Manufacturing, 2014. **65**: p. 175-185.

[21] Hasan, M.M.B., et al., *Carbon fibre reinforced thermoplastic composites developed from innovative hybrid yarn structures consisting of staple carbon fibres and polyamide 6 fibres.* Composites Science and Technology, 2018. **167**: p. 379-387.

[22] Akonda, M.H., C.A. Lawrence, and B.M. Weager, *Recycled carbon fibre-reinforced polypropylene thermoplastic composites.* Composites Part A: Applied Science and Manufacturing, 2012. **43**(1): p. 79-86.

[23] Miyake, T. and S. Imaeda, *A dry aligning method of discontinuous carbon fibers and improvement of mechanical properties of discontinuous fiber composites.* Advanced Manufacturing: Polymer & Composites Science, 2016. **2**(3-4): p. 117-123.

[24] Lawrence, C.A., *Fundamentals of spun yarn technology*. 2003: Crc Press.

[25] Lord, P.R., *Handbook of yarn production: Technology, science and economics*. 2003: Elsevier.

[26] Palmer, D., *Wrap spinning.* Carpet & Rug Industry, 1983. **11**(Oct): p. 15.

[27] Chin, W.-K. and S.-W. Yang, *Mechanical properties of short fiber reinforced thermoplastic composites —I. Elastic properties and predictions.* Journal of Polymer Research, 1995. **2**(1): p. 31-37.

[28] Fu, S.-Y. and B. Lauke, *The elastic modulus of misaligned short-fiber-reinforced polymers.* Composites Science and Technology, 1998. **58**(3): p. 389-400.

[29] Hashimoto, M., et al., *Prediction of tensile strength of discontinuous carbon fiber/polypropylene composite with fiber orientation distribution.* Composites Part A: Applied Science and Manufacturing, 2012. **43**(10): p. 1791-1799.

[30] Evans, J.T. and A.G. Gibson, *Composite angle ply laminates and netting analysis.* Proceedings of the Royal Society of London. Series A: Mathematical, Physical and Engineering Sciences, 2002. **458**(2028): p. 3079-3088.

[31] Verchery, G. *The Netting analysis as a limit case of the laminated structure theory*. in *Proceedings of the 19th International Conference on Composite Materials (Eds. SV Hoa, P. Hubert), Montreal, Canada, July 28-August 2*. 2013.

[32] Cox, H.L., *The elasticity and strength of paper and other fibrous materials.* British Journal of Applied Physics, 1952. **3**(3): p. 72-79.

[33] *18 - Fracture processes of aerospace materials*, in *Introduction to Aerospace Materials*, A.P. Mouritz, Editor. 2012, Woodhead Publishing. p. 428-453.

[34] Hicks, J., *8 - Brittle fracture*, in *Welded Joint Design (Third Edition)*, J. Hicks, Editor. 1999, Woodhead Publishing. p. 116-122.

[35] FranÇOis, D., *SECTION 7.5 - Brittle Fracture*, in *Handbook of Materials Behavior Models*, J. Lemaitre, Editor. 2001, Academic Press: Burlington. p. 566-576.

[36] Ardebili, H. and M.G. Pecht, *Chapter 5 - Encapsulation Defects and Failures*, in *Encapsulation Technologies for Electronic Applications*, H. Ardebili and M.G. Pecht, Editors. 2009, William Andrew Publishing: Oxford. p. 225-285.

[37] Benac, D.J., N. Cherolis, and D. Wood, *Managing Cold Temperature and Brittle Fracture Hazards in Pressure Vessels.* Journal of Failure Analysis and Prevention, 2016. **16**(1): p. 55-66.

[38] Benac, D.J., *Failure Analysis and Life Assessment of Structural Components and Equipment*, in *Failure Analysis and Prevention*, W.T. Becker and R.J. Shipley, Editors. 2002, ASM International. p. 0.

[39] Wulpi, D.J., *Understanding how components fail*. 2013: ASM international.

[40] Lonsdale, H., *Ammonia tank failure-South Africa.* Ammonia plant safety, 1975. **17**: p. 126-131.

[41] Kinloch, A.J., et al., *Deformation and fracture behaviour of a rubber-toughened epoxy: 1. Microstructure and fracture studies.* Polymer, 1983. **24**(10): p. 1341-1354.

[42] Chikhi, N., S. Fellahi, and M. Bakar, *Modification of epoxy resin using reactive liquid (ATBN) rubber.* European Polymer Journal, 2002. **38**(2): p. 251-264.

[43] Thomas, R., et al., *Miscibility, morphology, thermal, and mechanical properties of a DGEBA based epoxy resin toughened with a liquid rubber.* Polymer, 2008. **49**(1): p. 278-294.

[44] Shi, H.-Q., et al., *A high ductility RTM epoxy resin with relatively high modulus and Tg.* Journal of Polymer Research, 2015. **22**(7): p. 134.

[45] Jang, J. and D. Seo, *Performance improvement of rubber‐modified polybenzoxazine.* Journal of applied polymer science, 1998. **67**(1): p. 1-10.

[46] Jang, J. and H. Yang, *Toughness improvement of carbon-fibre/polybenzoxazine composites by rubber modification.* Composites science and technology, 2000. **60**(3): p. 457-463.

[47] Wong, D.W., et al., *Interlaminar toughening of woven fabric carbon/epoxy composite laminates using hybrid aramid/phenoxy interleaves.* Composites Part A: Applied Science and Manufacturing, 2017. **101**: p. 151-159.

[48] Selezneva, M., et al., *The brittle-to-ductile transition in tensile and impact behavior of hybrid carbon fibre/self-reinforced polypropylene composites.* Composites Part A: Applied Science and Manufacturing, 2018. **109**: p. 20-30.

[49] Swolfs, Y., et al., *Introducing ductility in hybrid carbon fibre/self-reinforced composites through control of the damage mechanisms.* Composite Structures, 2015. **131**: p. 259-265.

[50] Scott, J.M. and D.C. Phillips, *Carbon fibre composites with rubber toughened matrices.* Journal of Materials Science, 1975. **10**(4): p. 551-562.

[51] Marston, T.U., A.G. Atkins, and D.K. Felbeck, *Interfacial fracture energy and the toughness of composites.* Journal of Materials Science, 1974. **9**(3): p. 447-455.

[52] Atkins, A.G., *Intermittent bonding for high toughness/ high strength composites.* Journal of Materials Science, 1975. **10**(5): p. 819-832.

[53] Williams Jr, J.H. and P.N. Kousiounelos, *Thermoplastic fibre coatings enhance composite strength and toughness.* Fibre Science and Technology, 1978. **11**(2): p. 83-88.

[54] Hancox, N. and H. Wells, *The effects of fibre surface coatings on the mechanical properties of CFRP.* Fibre Science and Technology, 1977. **10**(1): p. 9-22.

[55] Liu, W., et al., *Improvement in interfacial shear strength and fracture toughness for carbon fiber reinforced epoxy composite by fiber sizing.* Polymer Composites, 2014. **35**(3): p. 482-488.

[56] Kinloch, A., et al., *The effect of silica nano particles and rubber particles on the toughness of multiphase thermosetting epoxy polymers.* Journal of Materials Science, 2005. **40**(18): p. 5083-5086.

[57] Hsieh, T., et al., *The toughness of epoxy polymers and fibre composites modified with rubber microparticles and silica nanoparticles.* Journal of materials science, 2010. **45**(5): p. 1193-1210.

[58] Zhang, H., et al., *Improved fracture toughness and integrated damage sensing capability by spray coated CNTs on carbon fibre prepreg.* Composites Part A: Applied Science and Manufacturing, 2015. **70**: p. 102-110.

[59] Meng, Q., et al., *Nanosilica-toughened polymer adhesives.* Materials & Design, 2014. **61**: p. 75-86.

[60] Sprenger, S., M.H. Kothmann, and V. Altstaedt, *Carbon fiber-reinforced composites using an epoxy resin matrix modified with reactive liquid rubber and silica nanoparticles.* Composites Science and Technology, 2014. **105**: p. 86-95.

[61] Yokozeki, T., et al., *Fracture toughness improvement of CFRP laminates by dispersion of cup-stacked carbon nanotubes.* Composites Science and Technology, 2009. **69**(14): p. 2268-2273.

[62] Ozdemir, N., et al., *Toughening of carbon fibre reinforced polymer composites with rubber nanoparticles for advanced industrial applications.* Express Polymer Letters, 2016. **10**(5): p. 394-407.

[63] Manders, P.W. and M. Bader, *The strength of hybrid glass/carbon fibre composites.* Journal of materials science, 1981. **16**(8): p. 2246-2256.

[64] Miwa, M. and N. Horiba, *Effects of fibre length on tensile strength of carbon/glass fibre hybrid composites.* Journal of materials science, 1994. **29**(4): p. 973-977.

[65] Jones, K.D. and A.T. DiBenedetto, *Fiber fracture in hybrid composite systems.* Composites Science and Technology, 1994. **51**(1): p. 53-62.

[66] Chiang, M.Y., et al., *Prediction and three-dimensional Monte-Carlo simulation for tensile properties of unidirectional hybrid composites.* Composites science and technology, 2005. **65**(11-12): p. 1719-1727.

[67] Yu, H., et al., *Pseudo-ductility in intermingled carbon/glass hybrid composites with highly aligned discontinuous fibres.* Composites Part A: Applied Science and Manufacturing, 2015. **73**: p. 35-44.

[68] Jalalvand, M., G. Czél, and M.R. Wisnom, *Numerical modelling of the damage modes in UD thin carbon/glass hybrid laminates.* Composites Science and Technology, 2014. **94**: p. 39-47.

[69] Jalalvand, M., G. Czél, and M.R. Wisnom, *Damage analysis of pseudo-ductile thin-ply UD hybrid composites – A new analytical method.* Composites Part A: Applied Science and Manufacturing, 2015. **69**: p. 83-93.

[70] Bunsell, A.R. and B. Harris, *Hybrid carbon and glass fibre composites.* Composites, 1974. **5**(4): p. 157-164.

[71] Swolfs, Y., L. Gorbatikh, and I. Verpoest, *Stress concentrations in hybrid unidirectional fibre-reinforced composites with random fibre packings.* Composites Science and Technology, 2013. **85**: p. 10-16.

[72] Mishnaevsky, L. and G. Dai, *Hybrid carbon/glass fiber composites: Micromechanical analysis of structure–damage resistance relationships.* Computational Materials Science, 2014. **81**: p. 630-640.

[73] Marom, G., et al., *Hybrid effects in composites: conditions for positive or negative effects versus rule-of-mixtures behaviour.* Journal of Materials Science, 1978. **13**(7): p. 1419-1426.

[74] Fukuda, H., *An advanced theory of the strength of hybrid composites.* Journal of Materials Science, 1984. **19**(3): p. 974-982.

[75] Marom, G., et al., *Impact behaviour of carbon/Kevlar hybrid composites.* Composites, 1986. **17**(2): p. 150-153.

[76] Jang, B.Z., et al., *Impact resistance and energy absorption mechanisms in hybrid composites.* Composites Science and Technology, 1989. **34**(4): p. 305-335.

[77] Park, R. and J. Jang, *Impact behavior of aramid fiber/glass fiber hybrid composite: Evaluation of four-layer hybrid composites.* Journal of Materials Science, 2001. **36**(9): p. 2359-2367.

[78] Sayer, M., N.B. Bektaş, and O. Sayman, *An experimental investigation on the impact behavior of hybrid composite plates.* Composite Structures, 2010. **92**(5): p. 1256-1262.

[79] Kalantari, M., C. Dong, and I.J. Davies, *Numerical investigation of the hybridisation mechanism in fibre reinforced hybrid composites subjected to flexural load.* Composites Part B: Engineering, 2016. **102**: p. 100-111.

[80] Ary Subagia, I.D.G., et al., *Effect of stacking sequence on the flexural properties of hybrid composites reinforced with carbon and basalt fibers.* Composites Part B: Engineering, 2014. **58**: p. 251-258.

[81] Dong, C., J. Duong, and I.J. Davies, *Flexural properties of S-2 glass and TR30S carbon fiber-reinforced epoxy hybrid composites.* Polymer Composites, 2012. **33**(5): p. 773-781.

[82] Dong, C. and I.J. Davies, *Optimal design for the flexural behaviour of glass and carbon fibre reinforced polymer hybrid composites.* Materials & Design, 2012. **37**: p. 450-457.

[83] Bucknall, C., *Polymer Glasses, Fracture of: Factors Controlling Toughness.* 2016.

[84] King, J., *Failure in composite materials.* Met. Mater., 1989. **40**(3): p. 720-726.

[85] Zhang, H., et al., *Localized toughening of carbon/epoxy laminates using dissolvable thermoplastic interleaves and electrospun fibres.* Composites Part A: Applied Science and Manufacturing, 2015. **79**: p. 116-126.

[86] Yun, N.G., Y.G. Won, and S.C. Kim, *Toughening of carbon fiber/epoxy composite by inserting polysulfone film to form morphology spectrum.* Polymer, 2004. **45**(20): p. 6953-6958.

[87] Sohn, M.-S. and X.-Z. Hu, *Mode II delamination toughness of carbon-fibre/epoxy composites with chopped Kevlar fibre reinforcement.* Composites Science and Technology, 1994. **52**(3): p. 439-448.

[88] Yasaee, M., et al., *Mode I interfacial toughening through discontinuous interleaves for damage suppression and control.* Composites Part A: Applied Science and Manufacturing, 2012. **43**(1): p. 198-207.

[89] Yasaee, M., et al., *Mode II interfacial toughening through discontinuous interleaves for damage suppression and control.* Composites Part A: Applied Science and Manufacturing, 2012. **43**(1): p. 121-128.

[90] Duarte, A., I. Herszberg, and R. Paton, *Impact resistance and tolerance of interleaved tape laminates.* Composite Structures, 1999. **47**(1): p. 753-758.

[91] Kretsis, G., *A review of the tensile, compressive, flexural and shear properties of hybrid fibre-reinforced plastics.* Composites, 1987. **18**(1): p. 13-23.

[92] Manders, P.W. and M.G. Bader, *The strength of hybrid glass/carbon fibre composites.* Journal of Materials Science, 1981. **16**(8): p. 2233-2245.

[93] Summerscales, J. and D. Short, *Carbon fibre and glass fibre hybrid reinforced plastics.* Composites, 1978. **9**(3): p. 157-166.

[94] Manders, P.W. and M.G. Bader, *The strength of hybrid glass/carbon fibre composites.* Journal of Materials Science, 1981. **16**(8): p. 2246-2256.

[95] Zweben, C., *Tensile strength of hybrid composites.* Journal of Materials Science, 1977. **12**(7): p. 1325-1337.

[96] Fukunaga, H., T.-W. Chou, and H. Fukuda, *Strength of Intermingled Hybrid Composites.* Journal of Reinforced Plastics and Composites, 1984. **3**(2): p. 145-160.

[97] Ren, P., et al., *Hybrid effect on mechanical properties of M40-T300 carbon fiber reinforced Bisphenol A Dicyanate ester composites.* Polymer Composites, 2010. **31**(12): p. 2129-2137.

[98] Peijs, A.A.J.M. and J.M.M. de Kok, *Hybrid composites based on polyethylene and carbon fibres. Part 6: Tensile and fatigue behaviour.* Composites, 1993. **24**(1): p. 19-32.

[99] Liang, Y., C. Sun, and F. Ansari, *Acoustic Emission Characterization of Damage in Hybrid Fiber-Reinforced Polymer Rods.* Journal of Composites for Construction, 2004. **8**(1): p. 70-78.

[100] Pitkethly, M.J. and M.G. Bader, *Failure modes of hybrid composites consisting of carbon fibre bundles dispersed in a glass fibre epoxy resin matrix.* Journal of Physics D: Applied Physics, 1987. **20**(3): p. 315-322.

[101] Zhang, Y., et al., *Tensile and interfacial properties of unidirectional flax/glass fiber reinforced hybrid composites.* Composites Science and Technology, 2013. **88**: p. 172-177.

[102] De Rosa, I.M., et al., *Post-impact mechanical characterisation of E-glass/basalt woven fabric interply hybrid laminates.* Express Polymer Letters, 2011. **5**(5): p. 449-459.

[103] Sarasini, F., et al., *Hybrid composites based on aramid and basalt woven fabrics: Impact damage modes and residual flexural properties.* Materials & Design, 2013. **49**: p. 290-302.

[104] Peijs, A.A.J.M. and R.W. Venderbosch, *Hybrid composites based on polyethylene and carbon fibres Part IV Influence of hybrid design on impact strength.* Journal of Materials Science Letters, 1991. **10**(19): p. 1122-1124.

[105] Sevkat, E., et al., *Effect of repeated impacts on the response of plain-woven hybrid composites.* Composites Part B: Engineering, 2010. **41**(5): p. 403-413.

[106] Enfedaque, A., et al., *Effect of Glass Fiber Hybridization on the Behavior Under Impact of Woven Carbon Fiber/Epoxy Laminates.* Journal of Composite Materials, 2010. **44**(25): p. 3051-3068.

[107] Sevkat, E., et al., *Drop-weight impact of plain-woven hybrid glass–graphite/toughened epoxy composites.* Composites Part A: Applied Science and Manufacturing, 2009. **40**(8): p. 1090-1110.

[108] Onal, L. and S. Adanur, *Effect of Stacking Sequence on the Mechanical Properties of Glass–Carbon Hybrid Composites before and after Impact.* Journal of Industrial Textiles, 2002. **31**(4): p. 255-271.

[109] Swolfs, Y., L. Gorbatikh, and I. Verpoest, *Fibre hybridisation in polymer composites: A review.* Composites Part A: Applied Science and Manufacturing, 2014. **67**: p. 181-200.

[110] Wolfrath, J., V. Michaud, and J.A.E. Månson, *Deconsolidation in glass mat thermoplastic composites: Analysis of the mechanisms.* Composites Part A: Applied Science and Manufacturing, 2005. **36**(12): p. 1608-1616.

[111] Wan, Y. and J. Takahashi, *Deconsolidation behavior of carbon fiber reinforced thermoplastics.* Journal of Reinforced Plastics and Composites, 2014. **33**(17): p. 1613-1624.

[112] Petras, A. and M.P.F. Sutcliffe, *Failure mode maps for honeycomb sandwich panels.* Composite Structures, 1999. **44**(4): p. 237-252.

[113] Allen, H.G., *Analysis and design of structural sandwich panels.* 1969.

[114] Zenkert, D., *An Introduction to Sandwich Construction*. 1995: Engineering Materials Advisory Services.

[115] Triantafillou, T.C. and L.J. Gibson, *Failure mode maps for foam core sandwich beams.* Materials Science and Engineering, 1987. **95**: p. 37-53.

[116] Vitale, J.P., et al., *Failure mode maps of natural and synthetic fiber reinforced composite sandwich panels.* Composites Part A: Applied Science and Manufacturing, 2017. **94**: p. 217-225.

[117] Mostafa, A., K. Shankar, and E.V. Morozov, *Behaviour of PU-foam/glass-fibre composite sandwich panels under flexural static load.* Materials and Structures, 2015. **48**(5): p. 1545-1559.

[118] Gdoutos, E. and I. Daniel, *Failure modes of composite sandwich beams.* Theoretical and Applied Mechanics, 2008. **35**(1-3): p. 105-118.

[119] Bau-Madsen, N., K.-H. Svendsen, and A. Kildegaard, *Large deflections of sandwich plates—an experimental investigation.* Composite Structures, 1993. **23**(1): p. 47-52.

[120] Daniel, I.M. and J.L. Abot, *Fabrication, testing and analysis of composite sandwich beams.* Composites Science and Technology, 2000. **60**(12-13): p. 2455-2463.

[121] Grenestedt, J.L., *Development of a new peel-stopper for sandwich structures.* Composites science and technology, 2001. **61**(11): p. 1555-1559.

[122] Burton, W.S. and A. Noor, *Structural analysis of the adhesive bond in a honeycomb core sandwich panel.* Finite Elements in analysis and design, 1997. **26**(3): p. 213-227.

[123] Mostafa, A., K. Shankar, and E.V. Morozov, *Effect of shear keys diameter on the shear performance of composite sandwich panel with PVC and PU foam core: FE study.* Composite Structures, 2013. **102**: p. 90-100.

[124] Mostafa, A., K. Shankar, and E.V. Morozov, *Independent analytical technique for analysis of the flexural behaviour of the composite sandwich panels incorporated with shear keys concept.* Materials and Structures, 2015. **48**(8): p. 2455-2474.

[125] Åkermo, M. and B. Tomas Åström, *Modelling face-core bonding in sandwich manufacturing: Thermoplastic faces and rigid closed-cell foam core.* Composites Part A: Applied Science and Manufacturing, 1998. **29**(5): p. 485-494.

[126] Rion, J., Y. Leterrier, and J.-A.E. Månson, *Prediction of the adhesive fillet size for skin to honeycomb core bonding in ultra-light sandwich structures.* Composites Part A: Applied Science and Manufacturing, 2008. **39**(9): p. 1547-1555.

[127] Grove, S.M., E. Popham, and M.E. Miles, *An investigation of the skin/core bond in honeycomb sandwich structures using statistical experimentation techniques.* Composites Part A: Applied Science and Manufacturing, 2006. **37**(5): p. 804-812.

[128] Mouritz, A.P., *Review of z-pinned composite laminates.* Composites Part A: Applied Science and Manufacturing, 2007. **38**(12): p. 2383-2397.

[129] Grogan, J., et al., *Ballistic Resistance of 2D and 3D Woven Sandwich Composites.* Journal of Sandwich Structures & Materials, 2007. **9**(3): p. 283-302.

[130] Tekalur, S.A., A.E. Bogdanovich, and A. Shukla, *Shock loading response of sandwich panels with 3-D woven E-glass composite skins and stitched foam core.* Composites Science and Technology, 2009. **69**(6): p. 736-753.

[131] Judawisastra, H., J. Ivens, and I. Verpoest, *The fatigue behaviour and damage development of 3D woven sandwich composites.* Composite Structures, 1998. **43**(1): p. 35-45.

[132] Sharma, S.C., M. Krishna, and H.N.N. Murthy, *Buckling Response of Stitched Polyurethane Foam Composite Sandwich Structures.* Journal of Reinforced Plastics and Composites, 2004. **23**(12): p. 1267-1277.

[133] Raju, K.S. and J.S. Tomblin, *Energy Absorption Characteristics of Stitched Composite Sandwich Panels.* Journal of Composite Materials, 1999. **33**(8): p. 712-728.

[134] Potluri, P., E. Kusak, and T.Y. Reddy, *Novel stitch-bonded sandwich composite structures.* Composite Structures, 2003. **59**(2): p. 251-259.

[135] Mouritz, A.P., *Delamination properties of z-pinned composites in hot–wet environment.* Composites Part A: Applied Science and Manufacturing, 2013. **52**: p. 134-142.

[136] Nanayakkara, A., S. Feih, and A.P. Mouritz, *Experimental analysis of the through-thickness compression properties of z-pinned sandwich composites.* Composites Part A: Applied Science and Manufacturing, 2011. **42**(11): p. 1673-1680.

[137] Hoffmann, J., J. Sabban, and G. Scharr, *Pullout performance of circumferentially notched z-pins in carbon fiber reinforced laminates.* Composites Part A: Applied Science and Manufacturing, 2018. **110**: p. 197-202.

[138] Henao, A., et al., *Mechanical performance of through-thickness tufted sandwich structures.* Composite Structures, 2010. **92**(9): p. 2052-2059.

[139] Xia, F. and X.-q. Wu, *Study on impact properties of through-thickness stitched foam sandwich composites.* Composite Structures, 2010. **92**(2): p. 412-421.

[140] Evans, J. and A. Gibson, *Composite angle ply laminates and netting analysis.* Proceedings of the Royal Society of London. Series A: Mathematical, Physical and Engineering Sciences, 2002. **458**(2028): p. 3079-3088.

[141] Ma, Y., et al., *Influence of Defects on Bending Properties of 2D-T700/E44 Composites Prepared by Improved Compression Molding Process.* Materials (Basel, Switzerland), 2018. **11**(11): p. 2132.

[142] Whitehouse, W., *The quantitative morphology of anisotropic trabecular bone.* Journal of microscopy, 1974. **101**(2): p. 153-168.

[143] Gibson, R.F., *Principles of composite material mechanics*. 2011: CRC press.

[144] Wei, H., et al., *Influence of small amount of glass fibers on mechanical properties of discontinuous recycled carbon fiber-reinforced thermoplastics.* Advanced Composite Materials, 2019. **28**(3): p. 321-334.

References

List of Publications

(1) Journal Papers

〔Peer-reviewed〕

(1-1) **B. Xiao**, R. Nishida, Z. Zhang, H. Hamada and Y. Yang, "Effects of needle punching on mechanical properties of glass mat composites with open hole", Fiber composites, No. 4, (2013-12), pp. 18-22.

(1-2) Z. Xu, **B. Xiao**, T. Hojo, H. Hamada and Y. Yang, "Mechanical Properties of Kenaf Mat Reinforced Composites", Journal of Biobased Materials and Bioenergy, Vol.9, No.2, (2015-4), pp.188-195.

(1-3) **B. Xiao**, Y. Yang, X. Wu, M. Liao, R. Nishida and H. Hamada, "Hybrid laminated composites molded by spray lay-up process", Fibers and Polymers, Vol.16, No.8, (2015-8) 1759-1765.

(1-4) Y. Wang, Y. Gao, J. Takahashi, Y. wan, Y. Li, M. Li, C. Zhang, **B. Xiao**, X. He, J. Li, "Effect of plating time on surface evolution of chromium modified graphite powder by multi-arc ion plating", Surface Topography: Metrology and Properties, (accepted online at 2019/1/16, https://doi.org/10.1088/2051-672X/aafef3).

(1-5) **B. Xiao**, Y. Wan, I. Ohsawa and J. Takahashi, "Effect of needle punching on flexural behavior of carbon fiber-reinforced thermoplastic sandwich panel with spring-backed core", Composites Part A, Vol.118, (2019-3), pp.57-66.

〔Peer-reviewed　Under review *Italic under preparation*〕

(1-6) **B. Xiao**, T. Zaima, K. Shindo, T. Kohira, J. Morisawa, Y. Wan, G. Yin, I. Ohsawa, and J. Takahashi. "A carding and stretching method for recycled carbon fibers on thermoplastics", Composites Part A. (Under review)

(1-7) ***B. Xiao**, H. Matsuda, Y. Wan, I. Ohsawa and J. Takahashi, "Hybrid effect on mechanical properties of carbon/aramid fiber hybrid composites", Composites Part A.*

(2) International Conference Proceeding

〔peer-reviewed　○: Presenter〕

(2-1) ○**B. Xiao**, Z. Xu and Y. Yang, "Durability of Kenaf Fiber reinforced thermosetting plastics", Proceedings of JSPP25- 25th Japan Society of Polymer Processing Conference, Tokyo, Japan, 25, 19-20, (2014-6).

(2-2) ○**B. Xiao**, T. Hojo, H. Hamada, and Y. Yang, "Fatigue properties of cellulosic-fiber mat reinforced thermosetting plastic composites", Proceedings of ASME 2014 International

Mechanical Engineering Congress & Exposition, Montreal, Canada, Vol. 9, No. IMECE2014-37802, pp. V009T12A049, (2014-11).

(2-3) ○**B. Xiao**, Y. Mochizuki, Y. Mizutani, M. Okoshi, Y. Yang and H. Hamada, "Mechanical properties of cardboard sandwiched glass fiber reinforced plastics", Proceedings of JSCM40- 40th Japanese symposium on composite material, Kanazawa, Japan, No. C2-10, (2015-9).

(2-4) ○**B. Xiao**, Y. Mochizuki, Y. Mizutani, R. Satsuta, I. Sawada, M. Kawamoto and Y. Yang, "Mechanical and acoustic properties of cardboard sandwiched composites", Proceedings of JISSE14- 14th Japan International SAMPE Symposium & Exhibition (JISSE14), Kanazawa, Japan, No. 50, (2015-12).

(2-5) ○**B. Xiao**, Y. Wan, I. Ohsawa and J. Takahashi, "Needle punching effect on carbon fiber reinforced thermoplastic sandwich panels", Proceedings of ICCM21- 21st International Conference on Composite Materials, Xi'an, China, No. 4062, (2017-8).

(2-6) ○**B. Xiao**, I. Ohsawa and J. Takahashi, "Manufacturing and flexural behavior of carbon fiber reinforced thermoplastic sandwich panels with springback cores", Proceedings of JCCM9- 9th Japanese Conference on Composite Materials, Kyoto, Japan, No. 3B-09, (2018-3).

(2-7) ○Y. Zhang, **B. Xiao**, I. Ohsawa and J. Takahashi, "Evaluation of soft-skin effect performance of carbon fiber reinforced thermoplastics", Proceedings of ECCM18- 18th European Conference on Composite Materials, Athens, Greece, No. 69, (2018-6).

(2-8) ○Y. Zhang, G. Yin, **B. Xiao**, Y. Wan, I. Ohsawa and J. Takahashi, "Comparison between springbacked carbon fiber card web reinforced thermoplastics and carbon fiber paper reinforced thermoplastics sandwich structures on bending and impact property", Proceedings of ECCM18- 18th European Conference on Composite Materials, Athens, Greece, No. 82, (2018-6).

(2-9) ○**B. Xiao**, I. Ohsawa and J. Takahashi, "The manufacturing of carbon-fiber paper reinforced thermoplastic core sandwiched panels under several degrees of consolidation", Proceedings of ECCM18- 18th European Conference on Composite Materials, Athens, Greece, No. 155, (2018-6).

(2-10) ○**B. Xiao**, I. Ohsawa, S. Naruse and J. Takahashi, "Hybrid reinforcement effect of discontinuous carbon/aramid fiber paper reinforced thermoplastics", Proceedings of JSCM43- 43rd Japanese Symposium on Composite Material, Toyama, Japan, No. B1-1-1, (2018-9).

(2-11) ○Y. Zhang, **B. Xiao**, I. Ohsawa and J. Takahashi, "The advantage of carbon fiber reinforced thermoplastics in body-contacting structure design", Proceedings of JSCM43-43rd Japanese Symposium on Composite Material, Toyama, Japan, No. C1-2-1, (2018-9).

(2-12) ○**B. Xiao**, H. Matsuda, I. Ohsawa and J. Takahashi, "Hybrid effect on carbon paper reinforced thermoplastics with aramid papers", Proceedings of JCCM10- 10th Japanese Conference on Composite Materials, Tokyo, Japan, No. 1D-16, (2019-3).

(3) Patent

〔acquired〕

(3-1) Y. Yang, Y. Ma, Q. Zhang, J. Yang, L. Yu, X. Liu, Z. Xu, X. Kong, **B. Xiao**. Carbon/aramid hybrid fiber reinforced composite pipe for energy absorption in vehicle. Invention Patent. Publication Patent Number: CN103661183B.

(4) Awards

(4-1) Merit Student, Donghua Univ., (2011, 2012&2013).
(4-2) School Scholarship, Donghua Univ., (2011).
(4-3) Premium School Scholarship (awarded to top 5% students in the department), Donghua Univ., (2012&2013).
(4-4) 'Light of Textile' Scholarship, China National Textile and Apparel Council, (2012)
(4-5) Santoni Scholarship, Santoni (Shanghai) Knitting Machinery Co., Ltd., (2013).
(4-6) Memorial Award Prize in the 5th Super Lightweight CFRP Bridge Student contest (SAMPE-China), (2013).
(4-7) Outstanding Graduates, Shanghai, China, (2014).
(4-8) Recommended as a master degree candidate exempted from the entrance examination, Donghua Univ., (2014).
(4-9) National Scholarship (Top Scholarship in China), China, (2015).
(4-10) Outstanding Graduates , Shanghai, China, (2016)
(4-11) Outstanding Master Dissertation Award, Donghua Univ., (2016).
(4-12) Scholarship under the State Scholarship Fund for PhD. Degree by China Scholarship Council, (2016).
(4-13) Second prize in the Fiscal 2016 SAMPE-Japan Student Bridge Contest (SAMPE-Japan), (2017).
(4-14) First prize in dispatch to SAMPE CAMX 2018, SAMPE-Japan, (Sep., 2018).

Acknowledgements

First and foremost I would like to express my sincere gratitude to my supervisor, Professor Jun Takahashi. I appreciate all his continuous contributions of time, ideas, and funding, for his patience, motivation and immense knowledge. It has been an honor to be one of his Ph. D. students. Undertaking this Ph. D. has been a truly life-changing experience for me and it would not have been possible to do without the support and guidance that I received from him.

I would also like to express my special appreciation and thanks to Doctor Isamu Ohsawa for all the considerable support and encouragement he gave me during the past three years. This Ph. D. would not have been achievable without his guidance and constant feedback.

Many thanks also to all my fellow members at the University of Tokyo, Dr. Yi Wan, Mr. Shaoping Qian, Mr. Yiran Wang, Mr. Linshu Meng, Mr. Xiangdong He, Mr. Ye Zhang, Ms. Yunqian Zhang, Mr. Tiansheng Ha, Mr. Yasuyuki Furuta, Ms. Siyi Shao, Mr. Jun Li, Mr. Hisaki Matsuda, Mr. Gutao Shen, Mr. Hao Wu, and previous lab mates, Mr. Takahiro Hyashi, Mr. Wataru Nagatsuka, Mr. Michinobu Fujita, Mr. Shinichiro Yamashita, Mr. Hanchul Lee, Ms, Haowen Wei, Mr. Peng Qu, Mr. Qitao Guo, Mr. Hao Piao, Mr. Guangbin Cai, Mr. Taro Nakamura, Ms. Zaoyang Li, Ms. Lubai Chen, Mr. Daiki Kobayashi, Mr. Yuto Nakashima, Mr. Wataru Sato, Mr. Guanghu Yin, Mr. Bohan Xiao, Ms. Natsumi Okano, Mr. Hideki Toyoda, for immensely contribution to my personal and professional time at Tokyo. The group has been a source of friendships as well as valuable discussion and collaboration.

Part of this study was conducted as Japanese METI project "the Future Pioneering Projects/ Innovative Structural Materials Project" since 2013fy. Authors would like to express sincere appreciation to the project members who have provided valuable information and useful discussions.

My sincere thanks also go to some of my friends either in Japan or in my homeland. Thank them for being so supportive, warm-hearted and encouraging, for supporting me spiritually throughout this period.

Lastly, I would like to thank my family especially my mom for letting me through all difficulties, without whose support and love, I would not have had the courage to embark on this journey at the first place. Thank them for always believing in me, helping in whatever way they could and supporting me in all my pursuits, which made it possible for me to complete all of what I started.

Bing Xiao
The University of Tokyo
May 2019